

August 2017

# A Study of Development of a Micro Hydro Turbine System with a Rim Drive and Air Injection Treatment for Cavitation.

Tomoki Sakamoto

*University of Wisconsin-Milwaukee*

Follow this and additional works at: <https://dc.uwm.edu/etd>



Part of the [Mechanical Engineering Commons](#)

---

## Recommended Citation

Sakamoto, Tomoki, "A Study of Development of a Micro Hydro Turbine System with a Rim Drive and Air Injection Treatment for Cavitation." (2017). *Theses and Dissertations*. 1689.

<https://dc.uwm.edu/etd/1689>

This Thesis is brought to you for free and open access by UWM Digital Commons. It has been accepted for inclusion in Theses and Dissertations by an authorized administrator of UWM Digital Commons. For more information, please contact [open-access@uwm.edu](mailto:open-access@uwm.edu).

A STUDY OF DEVELOPMENT OF A MICRO HYDRO TURBINE  
SYSTEM WITH A RIM DRIVE AND AIR INJECTION TREATMENT  
FOR CAVITATION.

by

Tomoki Sakamoto

A Thesis Submitted in  
Partial Fulfillment of the  
Requirements for the Degree of

Master of Science  
in Engineering

at

The University of Wisconsin–Milwaukee

August 2017

## ABSTRACT

### A STUDY OF DEVELOPMENT OF A MICRO HYDRO TURBINE SYSTEM WITH A RIM DRIVE AND AIR INJECTION TREATMENT FOR CAVITATION.

by  
Tomoki Sakamoto

The University of Wisconsin–Milwaukee, 2017  
Under the Supervision of Professor Ryoichi Amano

This thesis presents the study of Kaplan hydro turbines system at a very low head and air injection treatment to reduce cavitation happening around a turbine. Regarding the study of Kaplan hydro turbine system, optimization of hydro turbine system with a rim generator to gain a better performance was conducted by CFD and experiment. E-Motors, the partner of this research, is developing an integrated design to simplify manufacturing and installation. The integrated design includes a rim in the outside of the turbine runner to house the electrical generator rotor, namely rim drive. This approach enables a compact and simple assembly without having shafts and outside generators, thus improving efficiency and facilitating assembly. Output power is limited due to experimental conditions, but CFD calculations showed good efficiency potential of this design. About the air injection treatment, the effect of air injected into a hydraulic system was investigated regarding power and reduction of cavitation. It was found that the air injection treatment can decrease cavitation over the blade and hub at most by 96.1% and 98.7%, respectively.

# TABLE OF CONTENTS

	page
<b>LIST OF FIGURES</b> .....	<b>v</b>
<b>LIST OF TABLES</b> .....	<b>viii</b>
<b>LIST OF GREEK LETTERS</b> .....	<b>xii</b>
<b>ACKNOWLEDGMENTS</b> .....	<b>1</b>
<b>1. Introduction</b> .....	<b>1</b>
<b>2. Approach</b> .....	<b>5</b>
2.1. CFD.....	5
2.2. Large Eddy Simulation.....	5
2.3. Governing Equations of LES [11].....	7
2.4. WALE subgrid scale model [12] .....	9
2.5. Volume of Fluid (VOF).....	9
2.6. Experiment setup.....	10
2.7. Turbine design.....	12
<b>3. CFD development for Rim-Drive</b> .....	<b>14</b>
3.1. Mesh size .....	14
3.2. Time step .....	16
3.3. Draft tube design.....	18
3.4. Investigation of guide vanes at the 90-degree elbow .....	20
<b>4. Result and discussion on Rim-Drive</b> .....	<b>27</b>
4.1. Initial data .....	27
4.2. Presence of air .....	29
4.3. Effect of friction.....	30
4.4. Error analysis.....	32
4.5. Summary of experimental study .....	36
<b>5. Cavitation treatment by air injection</b> .....	<b>37</b>
5.1. Phenomenon Description .....	37
5.1.1. Cavitation number .....	37
5.1.2. Type of cavitation.....	38
5.2. Computational Fluid Dynamics (CFD) model setting up .....	40
5.2.1. Modeling.....	40
5.2.2. Configuration and mesh .....	41
5.2.3. Design of air injection holes.....	43
5.2.4. Boundary conditions.....	45
5.3. Result and Discussion .....	45
5.3.1. No air injected case.....	45
5.3.2. Fluctuation of pressure on the air injection hole .....	48

5.3.4. Design B.....	63
5.3.5. Constant Head Case .....	70
<b>6. Conclusions .....</b>	<b>78</b>

# LIST OF FIGURES

Figure 1: Sketch of the water phase diagram [8].....	3
Figure 2: Cavitation damage on the blades at the discharge from a Francis turbine [9]..	4
Figure 3: The decomposition into the GS eddies and SGS eddies.....	6
Figure 4 : 3D CAD of the experimental system .....	11
Figure 5 : The experiment system.....	11
Figure 6 : Geometrical layout of the turbine .....	12
Figure 7 : Turbine and stator made by 3D printer .....	13
Figure 8 : Mesh resolution ; (a) coarse 0.8 M (b) fine 1.5M (c) very fine 4.4M .....	15
Figure 9: Power output versus mesh size.....	15
Figure 10 : Y + around the stator and runner when the rotational speed is 3000 rpm ..	16
Figure 11 : The image of flow with different Courant number.....	17
Figure 12 : Convective Courant Number when the rotational speed is 3000 rpm .....	18
Figure 13 : Computational condition for the rim-drive .....	19
Figure 14 : Power output with for different draft tube angles.....	19
Figure 15 : Velocity profiles with 12 deg. tube (top) and 36 deg. tube (bottom).....	20
Figure 16 : Cross sectional view of the guide vanes in the elbow. Case (a): Without guide vane. Case (b): Two flat guide vanes. Case (c): One flat guide vane. Case (d): One curved guide vane.....	21
Figure 17 : Pressure distribution (a) without guide vanes (b) with two flat guide vanes..	22
Figure 18 : 2D sketch for the elbow with one flat guide vane.....	23
Figure 19: Mass flow rate (left) and pressure drop (right), flat guide vane.....	23
Figure 20: 2D sketch for the elbow with a curved guide vane .....	24
Figure 21: Mass flow rate (left) and pressure drop (right), curved guide vane .....	25
Figure 22 : Standard derivation of pressure drop; one flat guide vane(left), curved guide vane (right).....	26
Figure 23 : Configuration of the system.....	27
Figure 24: Mass flow rate of the CFD and experiment.....	28
Figure 25 : Power output of the CFD and experiment.....	28
Figure 26: Comparison CFD corrected for presence of air with the experiment .....	30
Figure 27 : The part causing friction.....	31
Figure 28 : Comparison CFD corrected for presence of air and friction with the experiment.....	32
Figure 29 : Corrected power output $W_f$ and experimental results with the error bar ...	36
Figure 30: Tip vortex cavitation on a propeller [b].....	39
Figure 31: Cavitation cloud on the suction surface of a hydrofoil [3].....	39
Figure 32: Sheet cavitation on the suction surface of a hydrofoil [34] .....	40

Figure 33 : Convective Courant Number on the stator when it runs at 3000rpm without any air injection.....	41
Figure 34 : Computational domain and the mesh around the system.....	42
Figure 35 : VVF in different mesh conditions; 1.9M, 3.6M, 5.2M.....	42
Figure 36 : Wall Y+ on the turbine when it runs at 1000rpm.....	43
Figure 37: Configuration of the air injection hole of Design A .....	44
Figure 38: Configuration of the air injection hole of Design B .....	45
Figure 39: Contour plots of VVF without air injection when the rotational speed is 1000rpm – 4000rpm, real time is 0.3 (s) .....	46
Figure 40 : Time history for the surface averaged VVF over the suction side of the blade .....	47
Figure 41: Profile of pressure on the air injection hole .....	50
Figure 42 : Contour plots of time averaged absolute pressure over the turbine.....	50
Figure 43 : Profile of mass flow rate of air from the air injection hole when the applied pressure on the holes is 51.7kPa and the turbine runs at 2000rpm.....	51
Figure 44 : Profile of mass flow rate of air from the air injection hole when the applied pressure on the holes is 51.7kPa and the turbine runs at 2000rpm.....	51
Figure 45: Traveling air injected into the system.....	52
Figure 46: 17 cross sections over the runner and draft tube.....	54
Figure 47 : profile of surface and time averaged VVF when the rotational speed is 3000rpm.....	55
Figure 48 : Profile of surface and time averaged absolute pressure at each cross section when the rotational speed is 3000rpm, No-air case .....	55
Figure 49 : Profile of surface and time averaged AVF when the rotational speed is 3000rpm.....	56
Figure 50: Contour plots of $f_c$ at cross section of the turbine (the rotational speed is 3000rpm and pressure on the air injection holes is 137.9kPa) .....	56
Figure 51 : Comparison of 68.9kPa and 137.9kPa air injection in terms of depth of air penetration and reduction of cavitation when the rotational speed is 1000rpm.....	60
Figure 52 : Comparison of 68.9kPa and 137.9kPa air injection in terms of depth of air penetration and reduction of cavitation when the rotational speed is 3000rpm.....	61
Figure 53: Profile of surface and time averaged VVF over the suction side of blade.....	62
Figure 54: Profile of surface and time averaged VVF over the hub.....	62
Figure 55: Contour plots of time averaged AVF over the turbine and cross sections a, b, c and d when the rotational speed is 1000rpm and pressure on the air holes is 137.9kPa.....	63
Figure 56: Contour plots of time averaged AVF and VVF over the turbine when the rotational speed is 1000rpm; air injected by 103.4kPa from the Design B(top), air injected 137.9kPa from the Design A (bottom) .....	67
Figure 57 : Profile of surface and time averaged VVF over the hub, Design B.....	68

Figure 58 : Profile of surface and time averaged VVF over the suction side of blade, Design B.....	68
Figure 59: Efficiency drop of the turbine when air is injected from the Design B.....	69
Figure 60: Profile of VVF over the blade.....	70
Figure 61 : Configuration of the computational domain and the inlet Boundary Condition .....	72
Figure 62 : Power output with different inlet condition.....	74
Figure 63 : Surface and time averaged pressure at the inlet.....	75
Figure 64 : Surface and time averaged VVF over the suction side of the blade with constant mass flow rate inlet condition .....	76
Figure 65 : Surface and time averaged VVF over the blade with constant mass flow rate inlet condition .....	76
Figure 66 : Surface and time averaged WVF over the blade with constant mass flow rate inlet condition at the each cross section; 1000rpm and 137.9kPa air injection	77

# LIST OF TABLES

Table 1 : Mesh conditions for cases (a), (b) and (c).....	14
Table 2: Range and accuracy of tools used for the experiment.....	32
Table 3: Data from the experiment, uncertainty and fractional uncertainty of torque ...	33
Table 4: Data from the experiment, uncertainty and fractional uncertainty of rotational speed.....	34
Table 5: Data from the experiment, uncertainty and fractional uncertainty of rotational mass flow rate .....	34
Table 6: Data from the experiment, fractional uncertainty, and uncertainty of power output.....	35
Table 7 : Cavitation number in different rotational speed.....	46
Table 8: VVF, power, and mass flow rate for No air injected case.....	48
Table 9: VVF, power, and mass flow rate; Design A, 51.7(kPa) on air injection holes.....	49
Table 10: Air injection Design A compared to No-air case when the rotational speed is 1000rpm.....	58
Table 11: Air injection Design A compared to No-air case when the rotational speed is 2000rpm.....	59
Table 12: Air injection Design A compared to No-air case when the rotational speed is 3000rpm.....	59
Table 13: Air injection Design A compared to No-air case when the rotational speed is 4000rpm.....	59
Table 14: Air injection Design B compared to No-air case when the rotational speed is 1000rpm.....	65
Table 15 : Air injection Design B compared to No-air case when the rotational speed is 2000rpm.....	65
Table 16 : Air injection Design B compared to No-air case when the rotational speed is 3000rpm.....	66
Table 17: Air injection Design B compared to No-air case when the rotational speed is 4000rpm.....	66
Table 18: VVF over the blade and hub, Mass flow rate and Power when the turbine rotates at 300rpm.....	70
Table 19 : Air injection Design B compared to No-air case when the rotational speed is 1000rpm and the inlet mass flow rate is 35.23kg/s .....	73
Table 20 : Air injection Design B compared to No-air case when the rotational speed is 2000rpm and the inlet mass flow rate is 39.14kg/s .....	73
Table 21 : Air injection Design B compared to No-air case when the rotational speed is 3000rpm and the inlet mass flow rate is 42.99kg/s .....	73
Table 22 : Air injection Design B compared to No-air case when the rotational speed is 4000rpm and the inlet mass flow rate is 46.55kg/s .....	74
Table 23: Efficiency drop (%) of the turbine in different rotational speed cases .....	75

# LIST OF SYMBOLS

$C$	Convective Courant Number
$C_r$	$= f_{\text{EXP}}/f_{\text{CFD}}$ , Ration of mass flow rate of CFD and experiment
$C_w$	Model coefficient
$C_{ij}$	Cross term
$D$	$= l/r_1$ , Dimensionless number
$D_a$	Distance between the center of the turbine and the air injection hole
$E_{\text{loss}}$	Energy loss due to friction
$F$	Friction force on the shaft (N)
$f_c$	$= f_w + 2f_v$
$f_{\text{CFD}}$	Mass flow rate from CFD (kg/s)
$f_{\text{EXP}}$	Mass flow rate from the experiment
$f_v$	Vaper volume fraction
$f_w$	Water volume fraction
$g$	Gravitational acceleration ( $\text{m/s}^2$ )
$g_{ij}$	$= \frac{\partial \langle u_i \rangle}{\partial x_j}$ , Velocity gradient tensor
$H$	Water head (m)
$k$	Turbulent kinetic energy
$k_{\text{SGS}}$	SGS turbulent kinetic energy
$l$	Distance between the center of the curved guide vane and the center of pipe
$L$	Moment on the turbine ( $\text{m}\cdot\text{N}$ )
$L$	$= r/r_0$ , Dimensionless number
$L_a$	$= D_a/R_t$ , Dimensionless number
$L_{ij}$	Leonard term

N	Rotational Speed (rpm)
p	pressure
P	$= p/\rho$
$P_V$	Vapor pressure
$P_\infty$	Reference pressure
Q	Mass flow rate of water (kg/s)
r	Distance between the guide vane and the center of the pipe (m)
$r_0$	Radius of the pipe (3 inches)
$r_1$	Radius of the curved guide vane
R	$= r_0/r_1$ , Dimensionless number
$R_t$	Radius of the turbine
$R_{ij}$	Reynolds stress term
$R_{shaft}$	Radius of the shaft
$S_{ij}$	Strain rate tensor
$S_{\alpha_i}$	source or sink of the $i$ th phase.
u	Velocity
$u_\tau$	Friction velocity
$U_\infty$	Reference velocity
$U(\emptyset)$	Uncertainty of $\emptyset$
$x_i$	Physical coordinate system
W	Power output (W)
$W_b$	Power output corrected for air bubble
$W_{CFD}$	Power output from CFD
y	Wall distance
$Y^+$	$= \frac{u_\tau y}{\nu}$ , normalized wall distance

- $z$  The distance from the water head to the center of the turbine
- $\forall_c$  Control volume
- $\forall_i$  Volume of the  $i$ th phase in a control volume
- $\langle \rangle$  Filtering operator
- $\sim$  SGS components

## LIST OF GREEK LETTERS

$\alpha$	Fraction function
$\alpha_i$	$i$ th phase volume fraction
$\delta_{ij}$	Kronecker delta
$\Delta$	Filter width
$\Delta t$	Time step size
$\theta$	Angle (degree)
$\eta$	Efficiency of the turbine
$\eta_{Air}$	Efficiency of the turbine when air is injected
$\eta_{No-air}$	Efficiency of the turbine of No-air injected case
$\nu, \nu_t, \nu_{SGS}$	Kinematic viscosity, eddy viscosity, SGS eddy viscosity
$\rho$	Density
$\rho_i$	Density of the $i$ th phase
$\rho_L$	Liquid density
$\phi$	any equivalent property
$\sigma$	Cavitation number

## LIST OF ABBREVIATIONS

AVF	Air volume fraction
CFD	Computational Fluid Dynamics
GS	Grid Scale
LES	Large Eddy Simulation
Re	Reynolds number
rpm	Revolutions per minute
SGS	Sub Grid Scale
VOF	Volume Of Fluid
VVF	Vapor Volume Fraction

# ACKNOWLEDGMENTS

I would first like to thank my thesis advisor Prof. Ryoichi Amano. Without his kind help, I would not be able to study here, at the University of Wisconsin–Milwaukee. The door to Prof. Amano's office was always open whenever I had questions about my research, and he was so generous and patient particularly in the beginning of my research.

This work would not have been possible without the financial support from DOE and UWM fund. I am grateful to all of those with whom I have had the pleasure to work during this project. I would especially like to thank Tarek Elgammal. As my friend and coworker of this project, he has taught me more than I could give him credit for here. He has shown me, by his example, what a good scientist and person should be.

I also like to show my appreciation to Prof. Suga from Osaka Prefecture University. He has been supportive of my career goals and always give me personal and professional guidance and taught me a great deal about both scientific research and life in general.

I would also like to thank the members of the committee, Prof. Istvan Lauko, and Prof. John Reisel, for their valuable comments and fair thesis assessment.

I also want to say thank to my friends I met here. They made my stay here in America precious. Thank you Ming, Sravan, Sai, Yash, Sophia, Teresa, John, Cynthia, Johnny, Alex, Neah, Luke, Prayag, Paulo, Vera, Violeta, Sam, Ines, Mandana, Ahmad, Muhannad, Hanseul, Seougbum,

Sanghee, Hiroto, Keita, Yuya, Hinako, Satoshi, Arisa and so many more I cannot possibly list them all.

Nobody has been more important to me in the pursuit of this project than the members of my family. I would like to thank my parents, whose love and guidance are with me in whatever I pursue. I would like to give the greatest of thanks to my family for the all they have done for me.

# 1. Introduction

Hydro-electric power, using the energy of rivers has become one of the highly reliable renewable energy sources especially in countries with many water sources. Hydropower supplies 16% of worldwide electricity production presently [1]. In addition to that, 86% of the renewable energy is generated from hydropower [2]. Since most large rivers have already been equipped with power stations, more and more attention is turning to small hydropower. Even though the power from each station is low, they can generate a tremendous amount of power aggregately. For this reason, making an efficient hydroelectric power system for small river or low heads is necessary.

Hydro-turbines are set to take advantage of head differences between water levels and to derive the power from the energy of falling water. In this study, since the aim is to make an efficient hydroelectric power system for low heads, a Kaplan turbine, which is capable of working efficiently with low heads and high flow rates has been selected as the turbine of the system.

Easy assembly and durability of the scheme have to be considered in terms of minimum maintenance of hydroelectric power system. To make installation easy and straightforward, the integrated design developed under the DOE STTR/SBIR grant [3], which includes a rim in the

outside of the turbine runner to house the electrical generator rotor, was used in this study. Regarding durability, air injection treatment for cavitation was also investigated in this study.

Cavitation is a transforming phenomenon from liquid to vapor when it is subjected to reduced pressures at constant ambient temperature. Cavitation is the process of boiling a liquid as a result of pressure reduction rather than heat addition. Figure 1 visually shows the difference between boiling and cavitation. When cavitation bubble collapse in liquid, the vapor is compressed rapidly by liquid phase, which has larger inertia and causes very high temperature and high pressure locally and instantaneously. In addition to that, cavitation bubbles can easily change their shape to non-spherical with affected ambient force and flow fields. In the process of transforming the shape of bubbles, it induces a liquid jet, whose velocity can be the order of the sound velocity of the liquid. When the liquid jet penetrates the bubble interface, and the bubbles become toroidal, it causes a high-pressure shock wave. These liquid jets and destructive shock wave due to the collapse of cavitation bubbles are the cause of performance degradation of fluid machinery and material damages. Figure 2 shows a picture of cavitation damage on turbine blades. Various studies on cavitation have been conducted for a long time to prevent deteriorating performance and erosion due to cavitation [4].

Cavitation is problematic not only because it causes erosion but also because it is a restriction for designing fluid machinery such as pumps and turbines to prevent erosion happening [4]. As a method to mitigate cavitation around hydro turbines, Arndt et al. proposed

air injection treatment [5]. Zhi-yong et. al. investigated experimentally and theoretically the cavitation control by aeration. The experimental results show that aeration remarkably increases the pressure in cavitation region [6]. Revetti et al. did research on the means of air injection to mitigate tip vortex cavitation of a Kaplan turbine and found that air injection can decrease the level of vibration of the system and damages due to tip vortex cavitation [7]. However, the effect of air injection when hydro turbines are cavitating with cloud or sheet cavitation have not studied enough. Hence, in this study, the effect of air injection when hydro turbines have strong cavitation such as cloud and sheet cavitation are investigated by CFD.

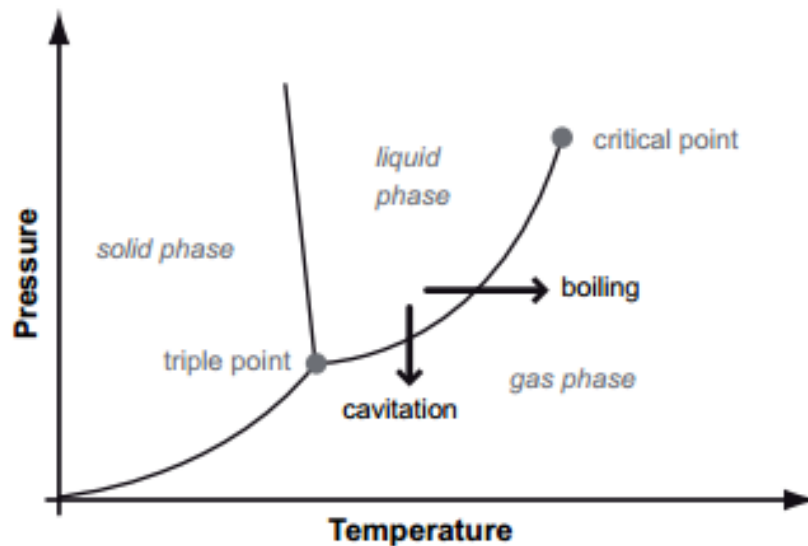


Figure 1: Sketch of the water phase diagram [8]



Figure 2: Cavitation damage on the blades at the discharge from a Francis turbine [9]

## 2. Approach

### 2.1. CFD

Turbulent flow is such familiar phenomena which one can see in one's daily life that many industrial products are designed by considering the effects of turbulent flow. For example, to make an aircraft of which wings can enhance the fuel efficiency and to produce a car with reduced aerodynamic drag, it is necessary to consider the effects of turbulent flow. Since the turbulent flow is a complicated phenomenon, it is often difficult to predict the fluid flow experimentally, especially when the geometry where the fluid is flowing complexly. Hence, it is required to run simulations to predict the turbulent fluid flow and to get the optimized design of industrial products, utilizing a Computational Fluid Dynamics (CFD) [10]. In this study, CFD was conducted by using the commercial codes of the multidisciplinary STAR CCM+. The Volume of Fluid (VOF) and Large Eddy Simulation (LES) models were chosen to solve the unsteady multi phase turbulent flow. As an eddy viscosity model, the WALE (Wall-Adapting Local-Eddy Viscosity) subgrid scale model was chosen in this study.

### 2.2. Large Eddy Simulation

There are various eddies in the range of large scales to small scales in a turbulence field. To simulate the significantly small eddies directly, it is necessary to use an extremely fine mesh which can resolve the small-scale eddies. However, resolving all kinds of scales of eddies is unrealistic in industry due to the high computational cost because it is required to

use at least more than  $Re^{9/4}$  grids to capture the smallest eddies, namely Kolmogorov scale. Moreover, a time step must be smaller as the mesh size becomes smaller in order to make the simulation stable and meet the Courant–Friedrichs–Lewy requirement, which results in the extremely high computational cost. Hence, using the fine mesh which can resolve all kinds of eddies is not suitable for industrial applications.

To solve this problem, LES decomposes the turbulent flow into Grid Scale (GS) eddies which are larger than the grid size and Sub-Grid Scale (SGS) eddies which are smaller than the grid size. Modeling the SGS eddies, which are independent of the geometry, and calculating the GS eddies directly can make it possible to simulate turbulence precisely with a relatively coarse mesh. This method is called the Large Eddy Simulation (LES).

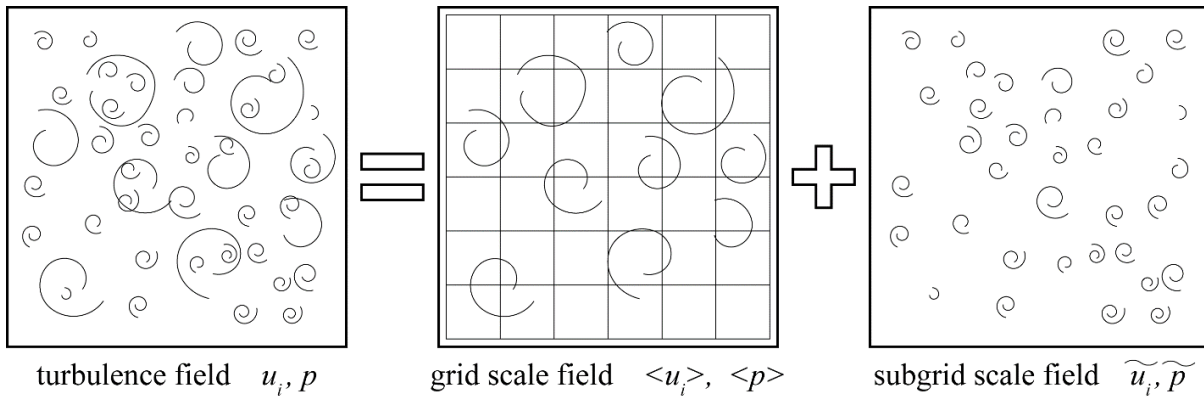


Figure 3: The decomposition into the GS eddies and SGS eddies

## 2.3. Governing Equations of LES [11]

The LES needs to classify eddies into GS eddies and SGS eddies as shown in Figure 3.

This operation is called a filtering operation. The velocity  $u$  is separated in this way by employing the filtering operator  $\langle \rangle$ .

$$u(x) = \underbrace{\langle u(x) \rangle}_{GS \text{ velocity}} + \underbrace{\widetilde{u(x)}}_{SGS \text{ velocity}} \quad (1)$$

The governing equations for LES can be derived by applying box filtering operation to the continuity equation and Navier–Stokes equations.

$$\frac{\partial \langle u_i \rangle}{\partial x_i} = 0 \quad (2)$$

$$\frac{\partial \langle u_i \rangle}{\partial t} + \langle u_j \rangle \frac{\partial \langle u_i \rangle}{\partial x_j} = -\frac{1}{\rho} \frac{\partial \langle p \rangle}{\partial x_i} + \frac{\partial}{\partial x_j} \left( \nu \frac{\partial \langle u_i \rangle}{\partial x_j} \right) - \frac{\partial \tau_{ij}}{\partial x_j} \quad (3)$$

These equations include filtering averaged value  $\langle \rangle$  and the unknown third term on the right-hand side of Eq. (3), which is the first derivative of SGS stress  $\tau_{ij} = \langle u_i u_j \rangle - \langle u_i \rangle \langle u_j \rangle$ . Hence, this equation is not closed. The physical model for SGS stress, namely SGS model, is needed to be introduced in order to close these governing equations. SGS stress is separated in the following way.

$$\begin{aligned} \tau_{ij} &= \langle u_i u_j \rangle - \langle u_i \rangle \langle u_j \rangle \\ &= \langle (\langle u_i \rangle + \widetilde{u}_i) (\langle u_j \rangle + \widetilde{u}_j) \rangle - \langle u_i \rangle \langle u_j \rangle \\ &= \underbrace{\langle \langle u_i \rangle \langle u_j \rangle \rangle}_{L_{ij}} - \langle u_i \rangle \langle u_j \rangle + \underbrace{\langle \langle u_i \rangle \widetilde{u}_j + \langle u_j \rangle \widetilde{u}_i \rangle}_{C_{ij}} + \underbrace{\langle \widetilde{u}_i \widetilde{u}_j \rangle}_{R_{ij}} \end{aligned} \quad (4)$$

where,

- $L_{ij}$ : Leonard term

This term expresses a part of stress given to GS eddies because of the interaction with SGS eddies. The Leonard term controls a part of energy dissipation of GS eddies.

- $C_{ij}$ : Cross term

$C_{ij}$  also controls a large part of energy dissipation of GS eddies with  $L_{ij}$ . In the case where box filter is applied,  $\langle u_i u_j \rangle - \langle u_i \rangle \langle u_j \rangle$  is directly modeled because  $C_{ij}$  becomes zero.  $C_{ij}$  and  $L_{ij}$  both have almost the same values and the effect of these two terms are normally neglected because they cancel out each other.

- $R_{ij}$ : Reynolds stress term

SGS modeling refers to the modeling for SGS Reynolds stress term  $R_{ij}$ . This term controls a large part of the effect on GS eddies by SGS eddies and have to include the effect of the energy dissipation. The eddy viscosity model, which defines the stress caused by turbulence eddies from the analogy of molecular viscous stress, is widely used for RANS and Reynolds stress is defined as the following:

$$\overline{u'_i u'_j} = \frac{2}{3} \delta_{ij} k - 2\nu_t \left( \frac{\partial \bar{u}_i}{\partial x_j} + \frac{\partial \bar{u}_j}{\partial x_i} \right) \quad (5)$$

The model which applies the same idea as that of eddy viscosity model for RANS is called SGS eddy viscosity model. Since the parameter which has to be modeled is SGS Reynolds stress, this is modeled by SGS turbulence kinetic energy  $k_{SGS}$  and SGS eddy kinematic viscosity  $\nu_{SGS}$  as shown in Eq. (6).

$$\tau_{ij} = \langle \tilde{u}_i \tilde{u}_j \rangle = \frac{2}{3} \delta_{ij} k_{SGS} - 2\nu_{SGS} \left( \frac{\partial \langle u_i \rangle}{\partial x_j} + \frac{\partial \langle u_j \rangle}{\partial x_i} \right) \quad (6)$$

## 2.4. WALE subgrid scale model [12]

The WALE (Wall-Adapting Local-Eddy Viscosity), Subgrid Scale model, is an eddy viscosity model, of which length scale is filtered width  $\Delta$ . In WALE model, the SGS eddy viscosity  $\nu_{SGS}$  is defined as following by using the filter width  $\Delta$ :

$$\nu_{SGS} = C_w \Delta^2 \frac{(S_{ij}^d S_{ij}^d)^{3/2}}{(S_{ij}^d S_{ij}^d)^{5/4} + (S_{ij} S_{ij})^{5/2}} \quad (7)$$

, where the strain rate tensor  $S_{ij}$ ,  $g_{ij}$  and the tensor  $S_{ij}^d$  are respectively defined as following;

$$S_{ij} = \frac{1}{2} \left( \frac{\partial \langle u_i \rangle}{\partial x_j} + \frac{\partial \langle u_j \rangle}{\partial x_i} \right) \quad (8)$$

$$g_{ij} = \frac{\partial \langle u_i \rangle}{\partial x_j} \quad (9)$$

$$S_{ij}^d = \frac{1}{2} (g_{ij}^2 + g_{ji}^2) - \frac{\delta_{ij}}{3} g_{kk}^2, \quad g_{ij}^2 = g_{ik} g_{kj} \quad (10)$$

In this study, the model coefficient  $C_w$  is set as  $C_w = 0.544$ .

## 2.5. Volume of Fluid (VOF)

The Volume of Fluid (VOF) method has been given by Noh and Woodward in 1976 [13], where fraction function  $\alpha$  (see Eq.(11)) appeared, although the first publication by Hirt and Nichols in 1981 [14]. The VOF model assumes that all immiscible fluid phases present in a control volume share velocity, pressure, and temperature fields. Therefore, the same set of basic governing equations describing momentum, mass, and energy transport in a single-phase flow is solved. The properties solved by this method are defined as following by using the (i)th phase volume fraction ( $\alpha_i$ )

$$\alpha_i = \frac{V_i}{V_c} \quad (11)$$

$$\phi = \sum_{l=1}^n \alpha_l \phi_l \quad (12)$$

where  $\phi$  is any equivalent property. The conservation equation that describes the transport of volume fractions is:

$$\frac{\partial}{\partial t} \int_V \alpha_i dV + \int_A \alpha_i (u - u_{rf}) dA = \int_V (S_{\alpha_i} - \frac{\alpha_i}{\rho_i} \frac{D\rho_i}{Dt}) dV \quad (13)$$

where  $S_{\alpha_i}$  is the source or sink of the  $i$  th phase. The equation considers the phase motion relative to the reference frame motion  $(u - u_{rf})$ .

The fluid interface is found by rapid change of the value of volume fraction  $\alpha$ . When a cell is empty with no traced fluid inside, the value of  $\alpha$  is zero. When the cell is full,  $\alpha = 1.0$ . When there is a fluid interface in the cell,  $0 < \alpha < 1.0$ .  $\alpha$  is a discontinuous function. In other words, its value jumps from 0 to 1 when the argument moves into the interior of traced phase. Hence, the fluid interface is found where the value of  $\alpha$  changes most rapidly.

## 2.6. Experiment setup

The hydro turbine loop is designed to run a horizontally oriented 0.0762m Kaplan turbine from a relatively low water height (3m maximum level) between the head and sink. The system is a closed system. Water flows from the head tank to the turbine, discharging to the sink tank, and then the system pumps the water again from the sink tank to the head one. The 3D CAD of the system is shown in Figure 4.

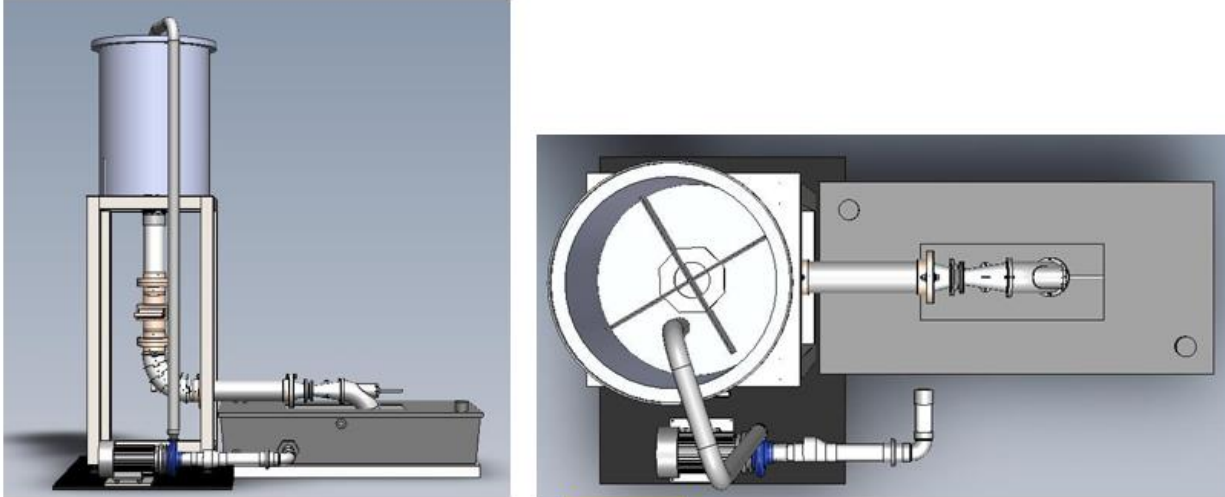


Figure 4 : 3D CAD of the experimental system

The experiment system is composed of a tank, a pump to circulate the water, two flow meters (one before the tank and one in the overflow pipe), and a turbine. Although Rim-drive generator usually does not have any shaft, the runner in this experiment system has a shaft for measuring the speed and torque. As seen in Figure 5, this shaft was connected to a Magtrol torque-meter and a DC generator. Electric power dissipates in a resistive load bank. The flow rate was measured by a Badger-Meter electromagnetic flow-meter, Model M-2000 M-Series Mag meter. The rotational speed of the runner was measured by Omega HHT13 Tachometer.

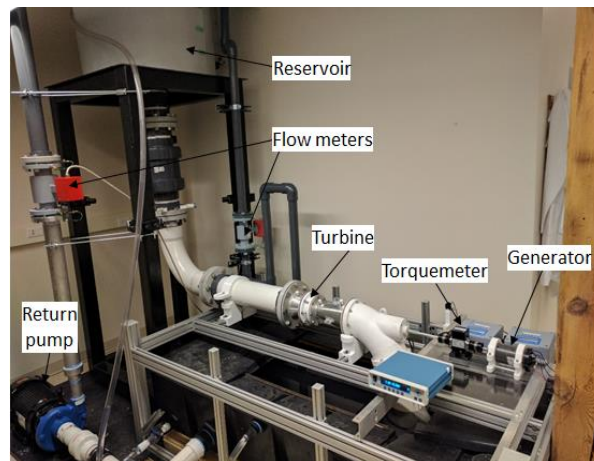


Figure 5 : The experiment system

## 2.7. Turbine design

The 3-inch diameter turbine design was developed by Turbine Builder design software [15] and then 3D CAD was built and exported to the CFD model. The rotor blade has an aspect ratio of 1.0, the thickness–chord ratio of 0.07, and count of 5 blades. The geometrical layout of the turbine is shown in Figure 6. The turbine and stator for the experiment were 3D printed. As shown in Figure 7, the runner has a slot to slide the electrical generator. The material selected for the runner and stator manufacturing was Eastman Amphora 3D Polymer AM3300 marketed by ColorFabb as nGen [16].

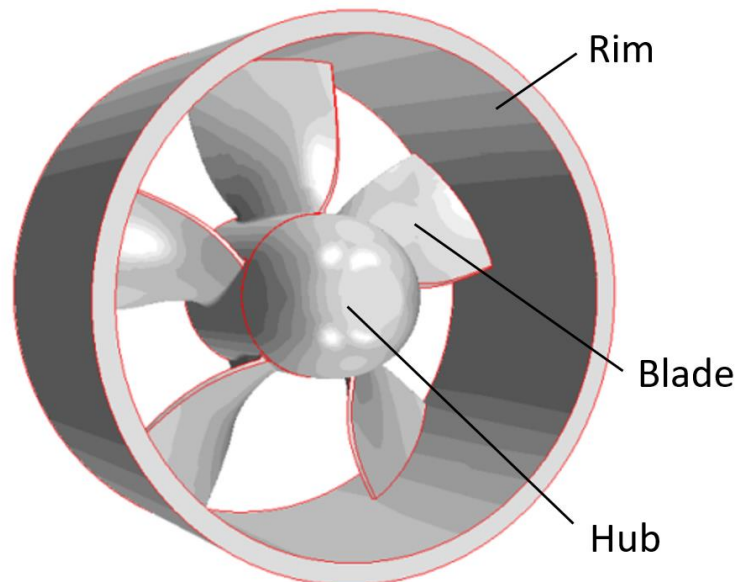


Figure 6 : Geometrical layout of the turbine

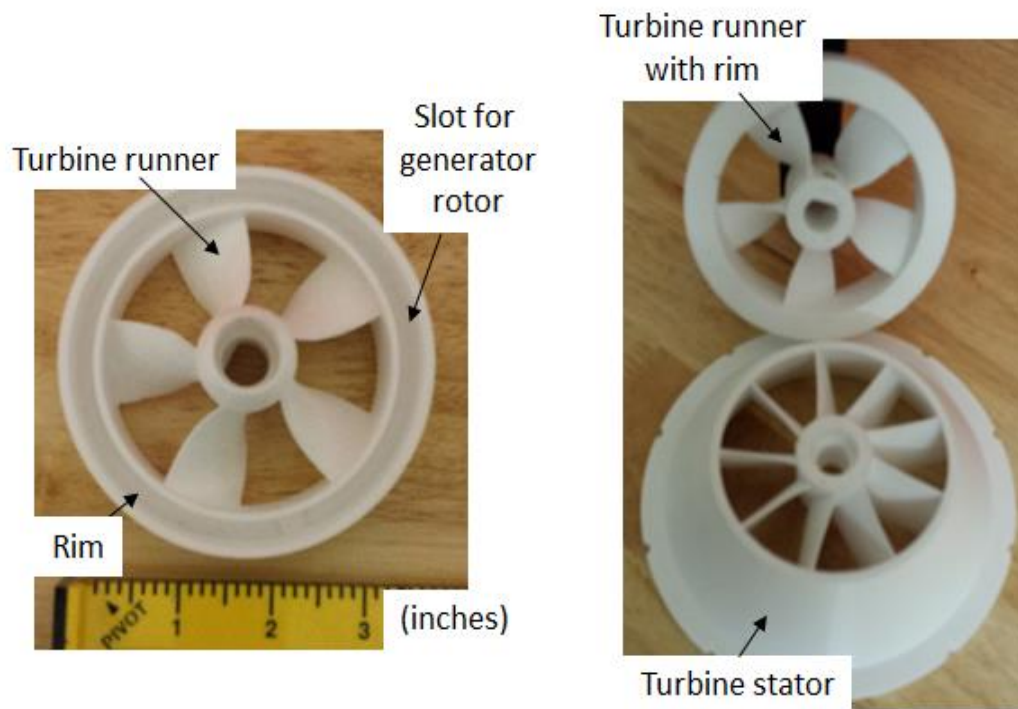


Figure 7 : Turbine and stator made by 3D printer

### 3. CFD development for Rim-Drive

#### 3.1. Mesh size

Three kinds of polyhedral meshes were initially tested around the turbine to examine the effect of the mesh size. The detail of these meshes is shown in Table 1. Figure 8 shows the mesh resolution around the runner in each case. The power output was chosen as the parameter to check the mesh independence. As shown in Figure 9, The difference of power output is 6.4% between 0.8 million and 1.5 million setups and 10.4% between 1.5 million and 4.4 million setups. Considering the time management and the accuracy of the CFD, a mesh with 1.5million cells was selected for this study.

It is important to have fine enough mesh near the wall to get precise simulation results because the amount of change of physical value such as velocity is significantly big there. To check if the mesh near the wall is fine enough, dimensionless distance  $Y^+$ , defined by Eq.(14), is checked. Figure 10 shows the mesh around the rotor and stator. Although the maximum of  $Y^+$  was 25,  $Y^+$  was kept less than 2.5 almost all over the stator and turbine.

$$Y^+ = \frac{u_\tau y}{\nu} \tag{14}$$

Table 1 : Mesh conditions for cases (a), (b) and (c)

Number of Cells	0.8 Million	1.5 Million	4.4 Million
Computational Time	1.0x	1.9x	5.5x
Simulation Detail	Coarse	Fine	Very Fine

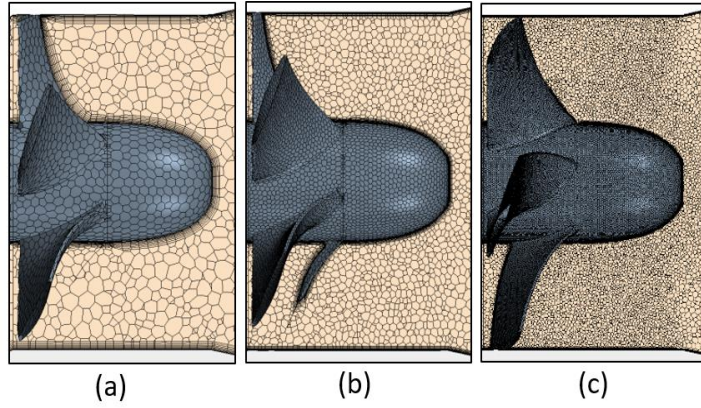


Figure 8 : Mesh resolution ; (a) coarse 0.8 M (b) fine 1.5M (c) very fine 4.4M

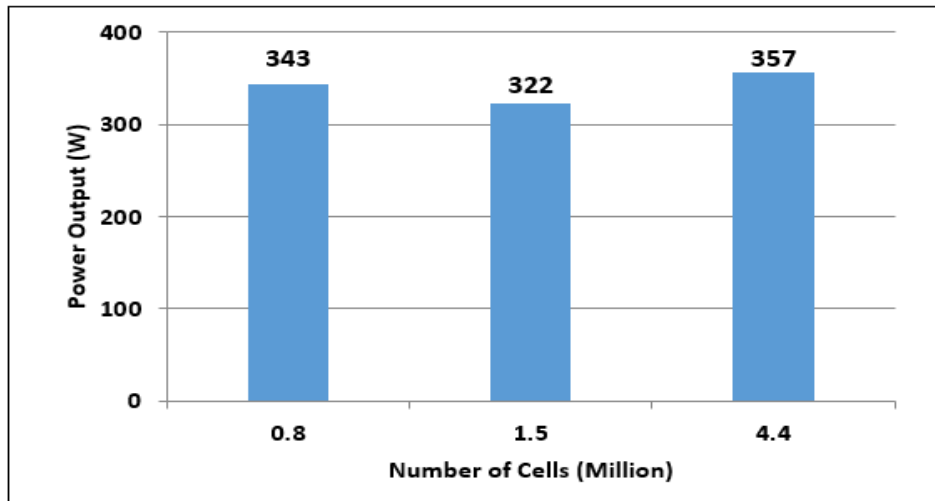


Figure 9: Power output versus mesh size

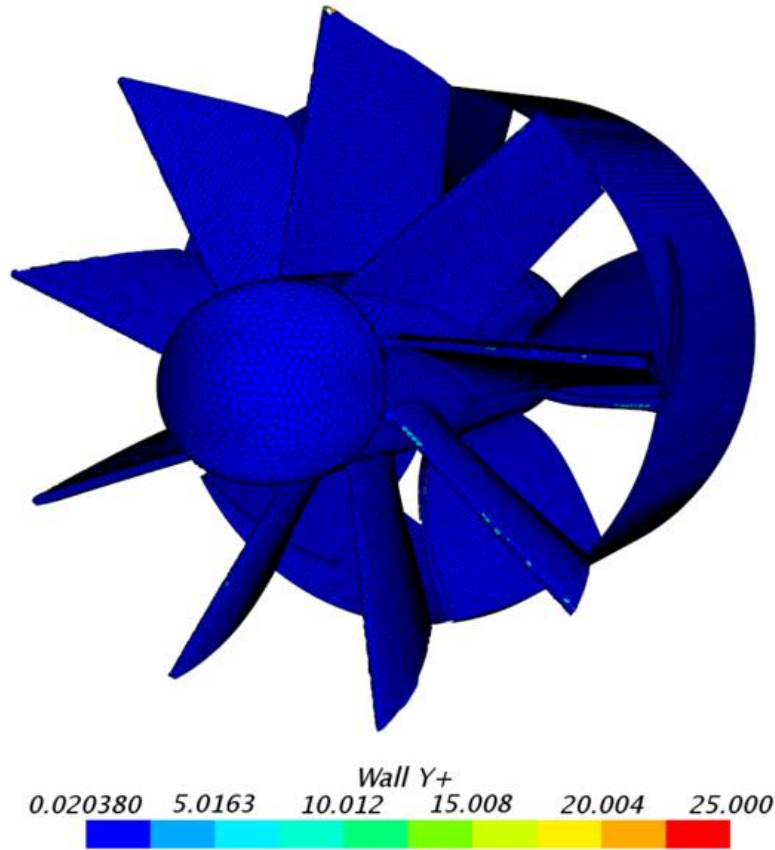


Figure 10 :  $Y^+$  around the stator and runner when the rotational speed is 3000 rpm

### 3.2. Time step

A time step  $\Delta t = 10^{-4}$ (s) was chosen for the simulation of the entire system. In order to verify the condition of the mesh, and the time step, the Convective Courant Number  $C$  around the runner and stator were checked. The Convective Courant Number  $C$  is the dimensionless transport per time step and defined as Eq.(15) in the one-dimensional case. This number is widely used to check if the size of the time step is proper or not. For example, if the courant number is 1, the flow of a certain point advances to the next element at the next moment as shown in the upper diagram of Figure 11. Therefore, the original analysis accuracy

of the mesh can be obtained. On the other hand, if the Courant number is 10, the flow goes forward by the 10 elements at the next moment as shown in the lower diagram of Figure 11, passing through the nine elements during that time. Therefore, the accuracy will be as same as simulations with 10 times coarse mesh. As Figure 12 shows, the Convective Courant Number is less than 2.0 over almost all area on the stator and runner.

$$C = \frac{u\Delta t}{\Delta L} \tag{15}$$

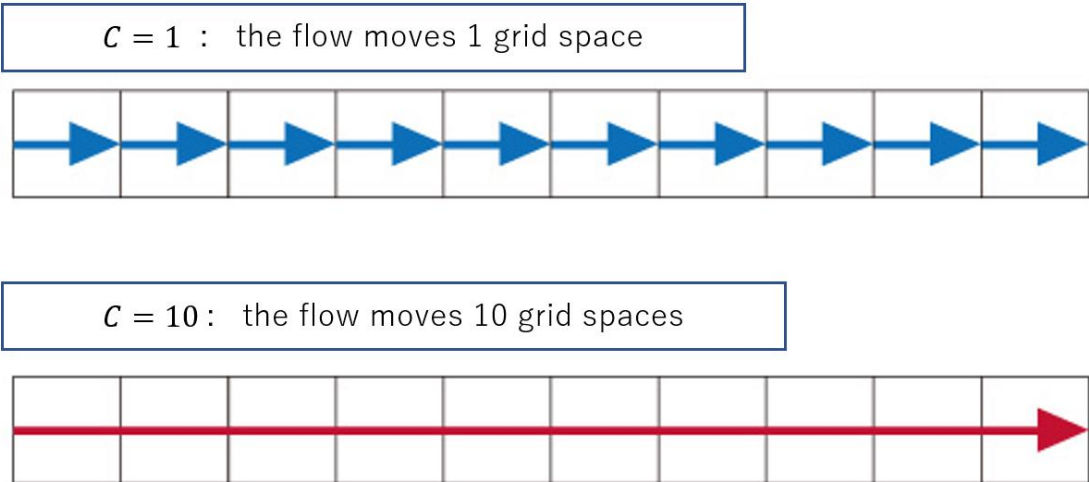


Figure 11 : The image of flow with different Courant number

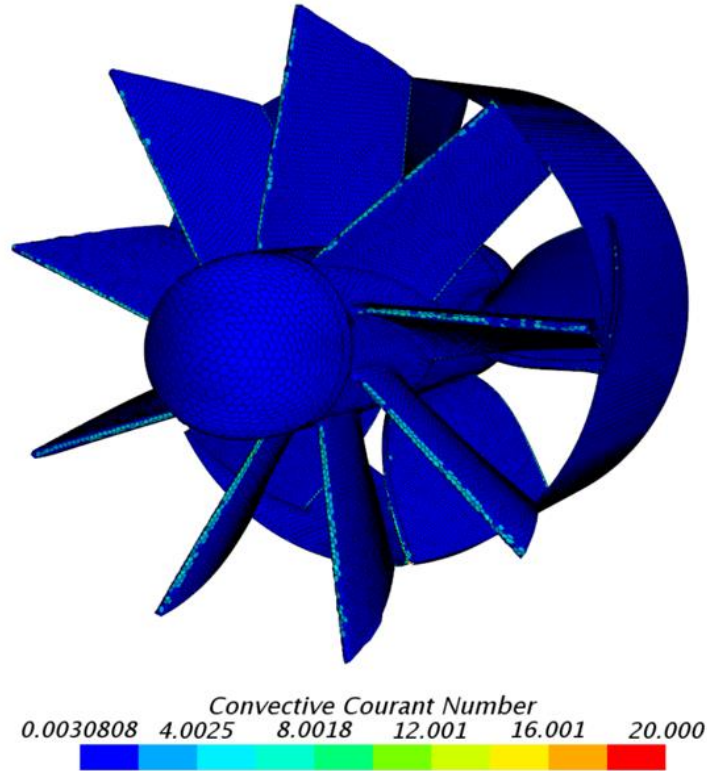


Figure 12 : Convective Courant Number when the rotational speed is 3000 rpm

### 3.3. Draft tube design

It is well known that the draft tube has a substantial impact on the performance of hydro turbines [17]. Hence, in this study, the shape of the draft tube was investigated to get the best power output. The equations for power output is shown in Eq. (16). The angle of the intake tube and the rotational speed of the turbine were set as constant, 30 degrees and 4000 rpm, respectively. The computational condition is shown in Figure 13.

$$W = \frac{L \cdot \pi \cdot N}{30} \quad (16)$$

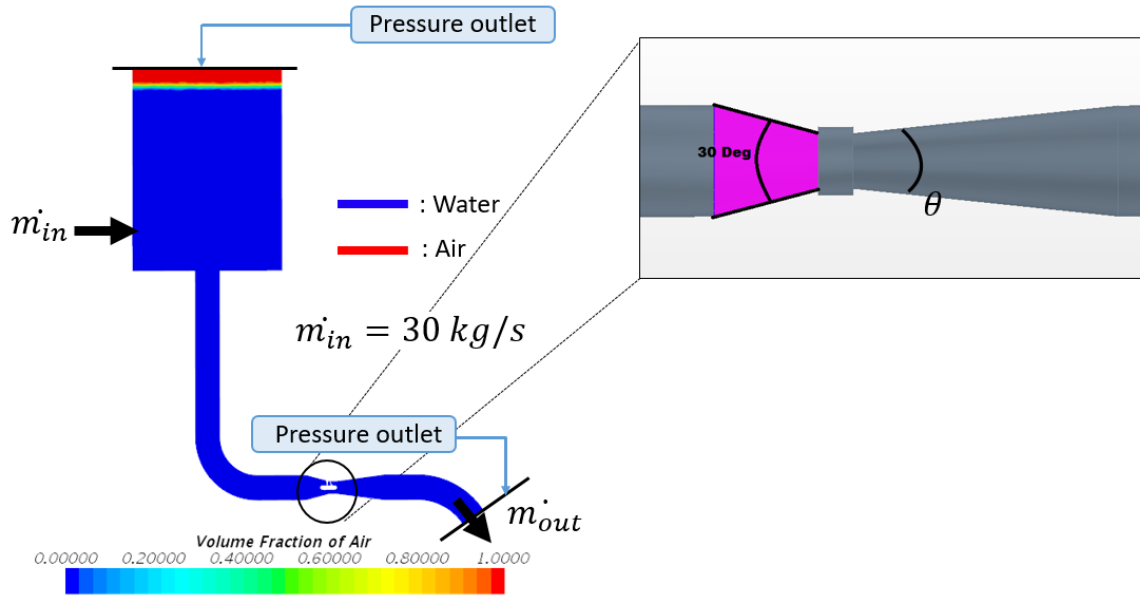


Figure 13 : Computational condition for the rim-drive

Five kinds of draft tube angles were tested in this study. Figure 14 shows the profile of the power output with different draft tube angle. For the greater value of the draft tube angle, it is seen that the flowing water leave the boundary and cause separations, which bring down the efficiency of draft tubes (see Figure 15). Hence, there is a tendency that less draft tube angle gives more power output (see Figure 14). Considering the limitation of the lab space of the room, a 15-degree draft tube angle was selected at the end.

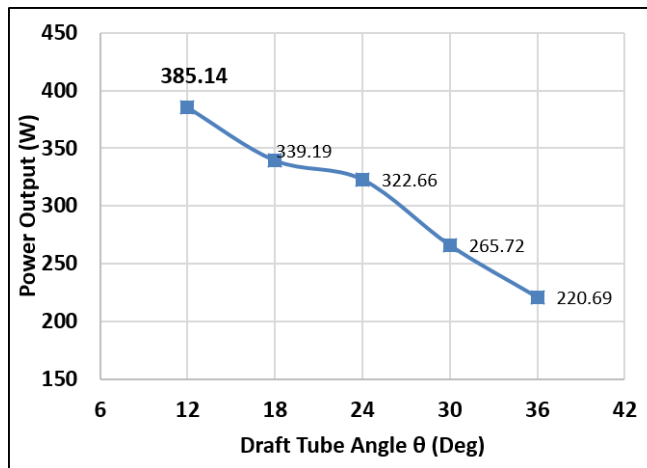


Figure 14 : Power output with for different draft tube angles

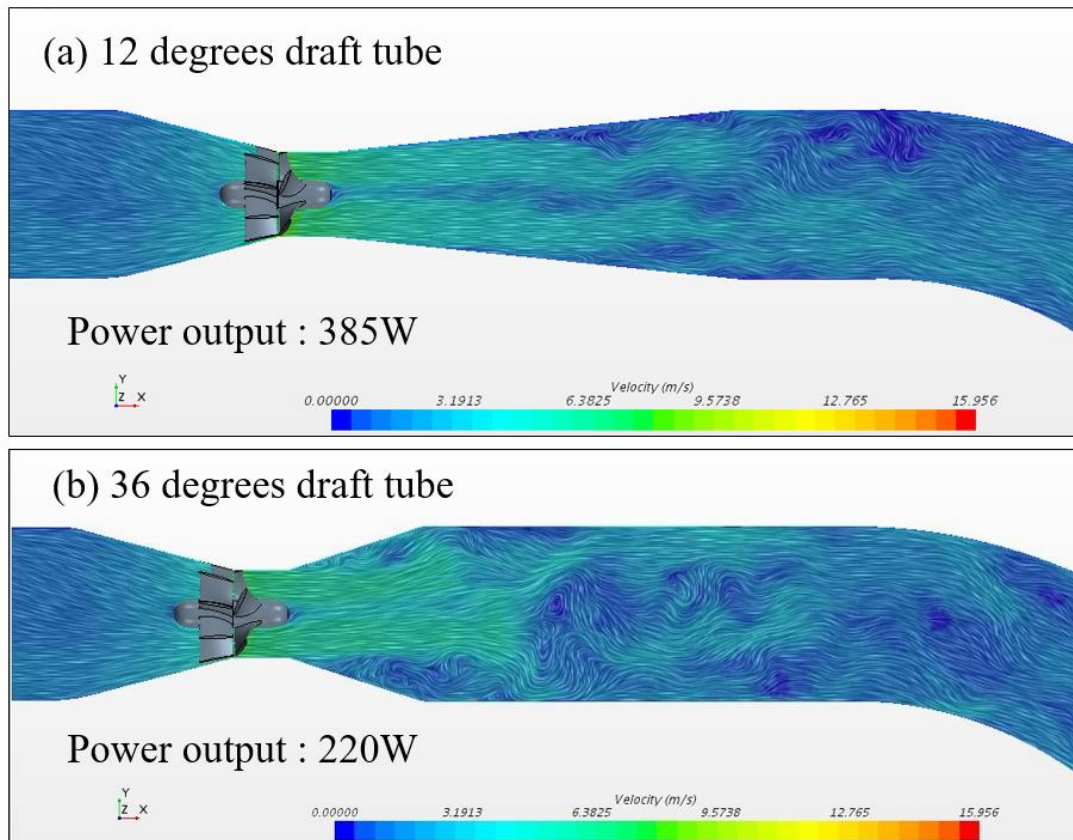


Figure 15 : Velocity profiles with 12 deg. tube (top) and 36 deg. tube (bottom)

### 3.4. Investigation of guide vanes at the 90-degree elbow

The experimental system includes a 90-degree elbow just upstream of the turbine (see Figure 4). Such an elbow causes flow skewness and eddies due to the sudden change in flow direction when the flow enters the elbow. Of course, the best policy is to avoid or minimize such discontinuities, but this is not always practical. One of the ways to minimize the problem caused by the sudden change of the flow direction is the use of guide vanes. Hence, in this study, four kinds of guide vanes in the elbow, shown in Figure 16, were examined.

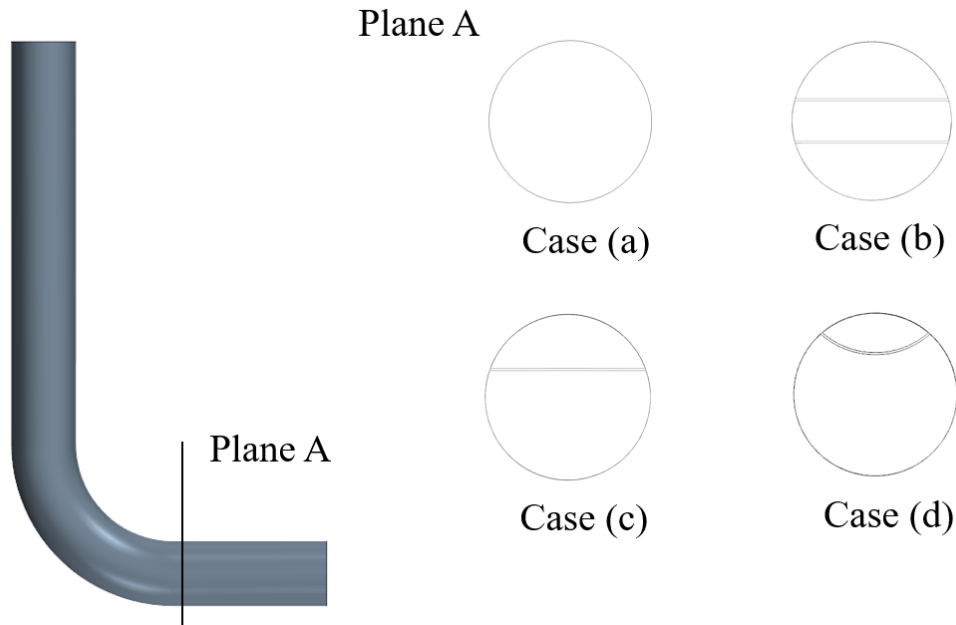


Figure 16 : Cross sectional view of the guide vanes in the elbow. Case (a): Without guide vane. Case (b): Two flat guide vanes. Case (c): One flat guide vane. Case (d): One curved guide vane.

Figure 17 illustrates the ability of the guide vanes to straighten the flow in the elbow.

As the disadvantage of the guide vane, it was found that the guide vanes caused an energy loss due to the friction between the flow and the guide vanes.

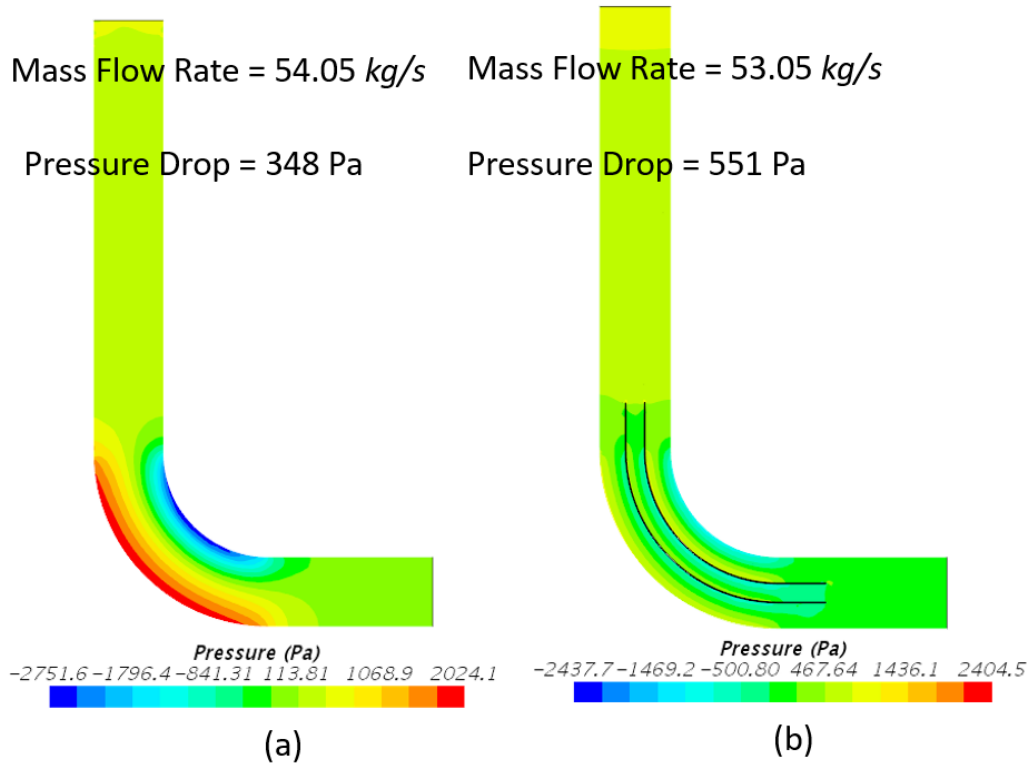


Figure 17 : Pressure distribution (a) without guide vanes (b) with two flat guide vanes

Firstly, Optimization study for the Case(c) was conducted. To consider the effect of the position of the guide vane, a new dimensionless parameter ( $L$ ) was defined for the flat guide vanes to express the guide vane position concerning the center of the elbow:

$$L = r/r_0 \quad (17)$$

where  $r$  is the distance between the guide vane and the center of the pipe, and  $r_0$  is the radius of the pipe, which is constant at 0.0762m in this case. Also, the angle  $\theta$  is defined as the ending point of the guide vane as shown in Figure 18.

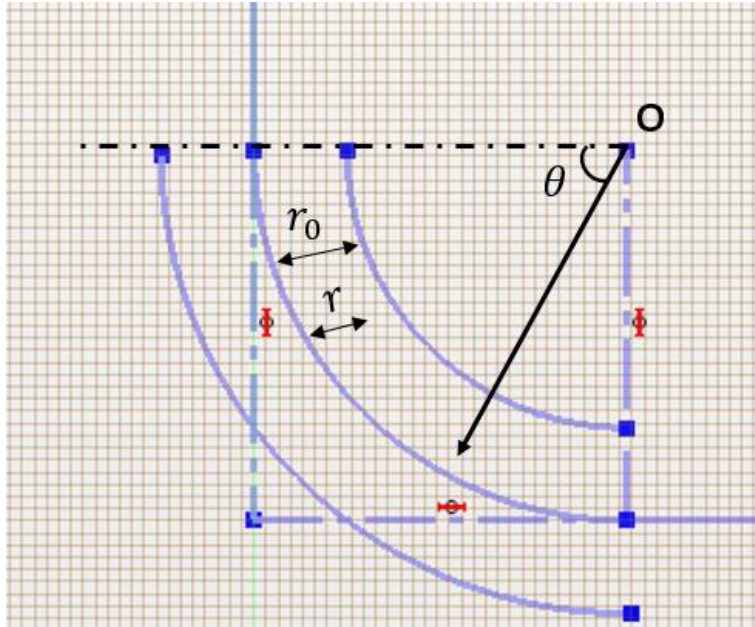


Figure 18 : 2D sketch for the elbow with one flat guide vane

Three values of  $\theta$  (30, 60 and 90 degrees) and three values of  $L$  (0.33, 0.50 and 0.67) were used for the flat guide vane, and the mass flow rate and the pressure drop were checked (Figure 19). From this result, the position of the guide vane ( $L$ ) does not affect the mass flow rate and pressure drop. Besides, there is a tendency of more mass flow rate and less pressure drop with larger  $\theta$ . Hence, 90-degree is the best among of 30, 60 and 90-degree guide vanes.

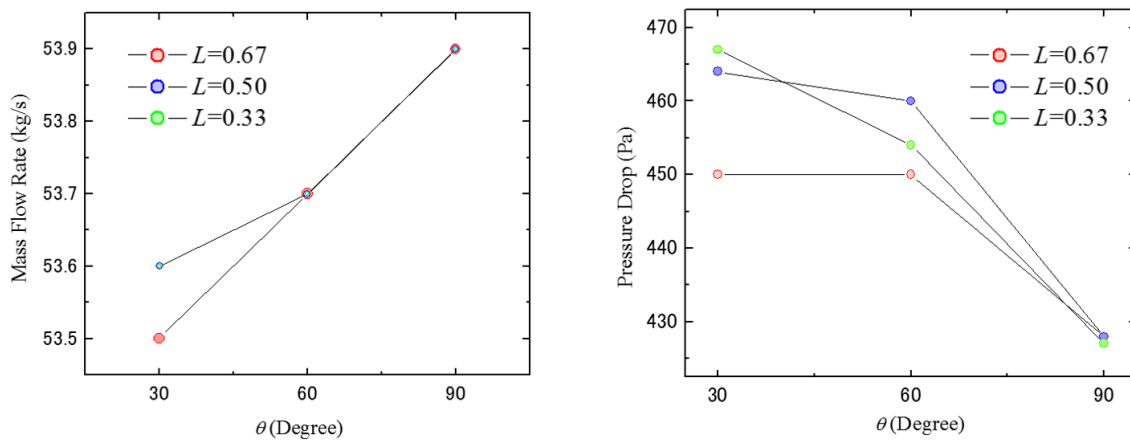


Figure 19: Mass flow rate (left) and pressure drop (right), flat guide vane

Secondary, an optimization study for the Case(d) was conducted. Two other dimensionless parameters ( $R$  and  $D$ ) were defined for the curved guide vane case. The details are shown in Figure 20 and Eq. (18) and Eq. (19). In the case of the one flat guide vane, it was discovered 90-degree guide vane was the best in terms of maximizing mass flow rate and minimizing pressure drop. Hence, in the study of Case(d),  $\theta$  was set as constant as 90 degrees. The profile of mass flow rate and pressure drop are shown in Figure 21. There is a tendency that larger  $D$  and smaller  $R$  gives more mass flow rate and less pressure drop because of less wet area of the guide vane which cause friction loss.

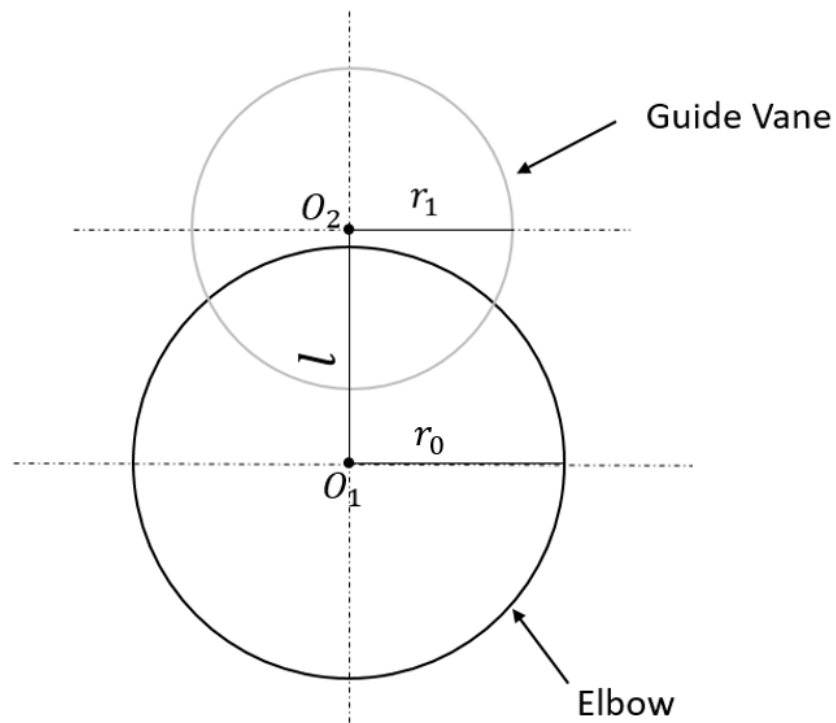


Figure 20: 2D sketch for the elbow with a curved guide vane

$$R = r_0/r_1 \quad (18)$$

$$D = l/r_0 \quad (19)$$

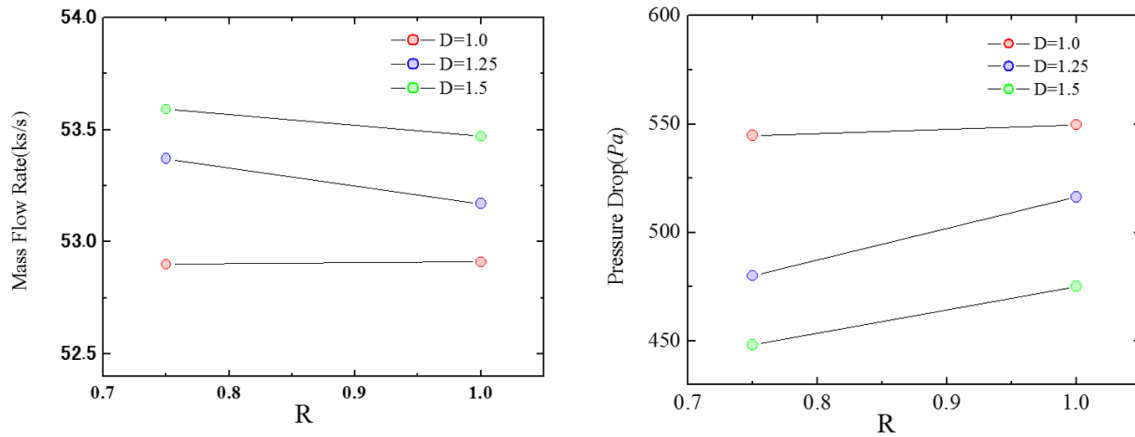


Figure 21: Mass flow rate (left) and pressure drop (right), curved guide vane

According to these different guide vane cases, regarding energy, the best choice is not to install any guide vane. However, another factor needs to be considered, particularly for a hydro turbine which is to operate on a continuous basis with minimum maintenance. The pressure fluctuations observed in the pipe could induce vibrations and cause turbine wear. While the standard derivation of pressure drop in the case of without any guide vane was 7.9 Pa, as Figure 22 shows, any guide vane at the elbow can reduce the pressure fluctuation in the pipe. If this is a concern, some guide vanes can be implemented in the system, benefiting maintenance needs at the cost of a small energy loss due to the friction on guide vane surfaces.

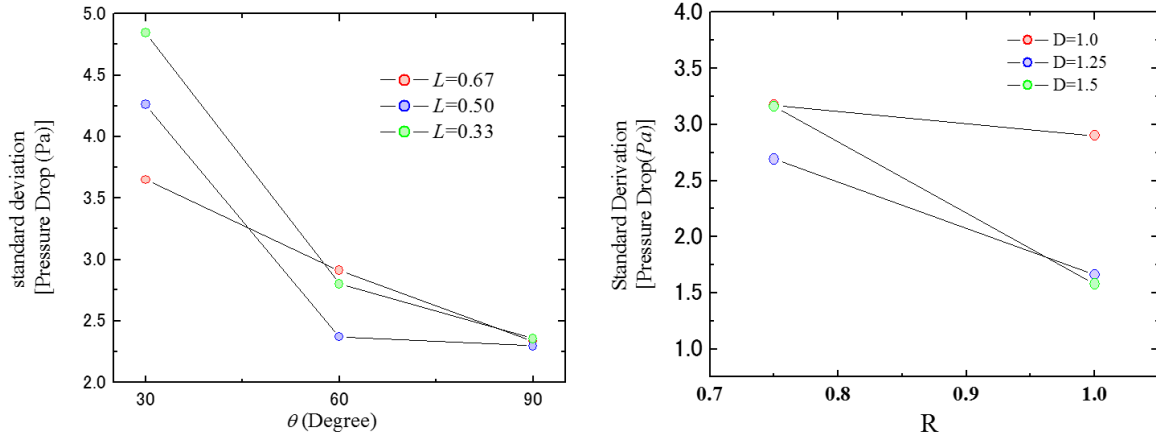


Figure 22 : Standard derivation of pressure drop; one flat guide vane(left), curved guide vane (right)

## 4. Result and discussion on Rim-Drive

### 4.1. Initial data

Considering the study of draft tubes and guide vanes, a 15-degree draft tube and elbow without any guide vane were selected for the experiment and CFD setup. The configuration of the system is shown in Figure 23. The CFD and experiment were conducted with 2.0m water head and the result is shown in Figure 24 and Figure 25. As Figure 24 and Figure 25 show, there is significant disagreement between CFD and experiment. In the next section, the causes of these disagreements are discussed.

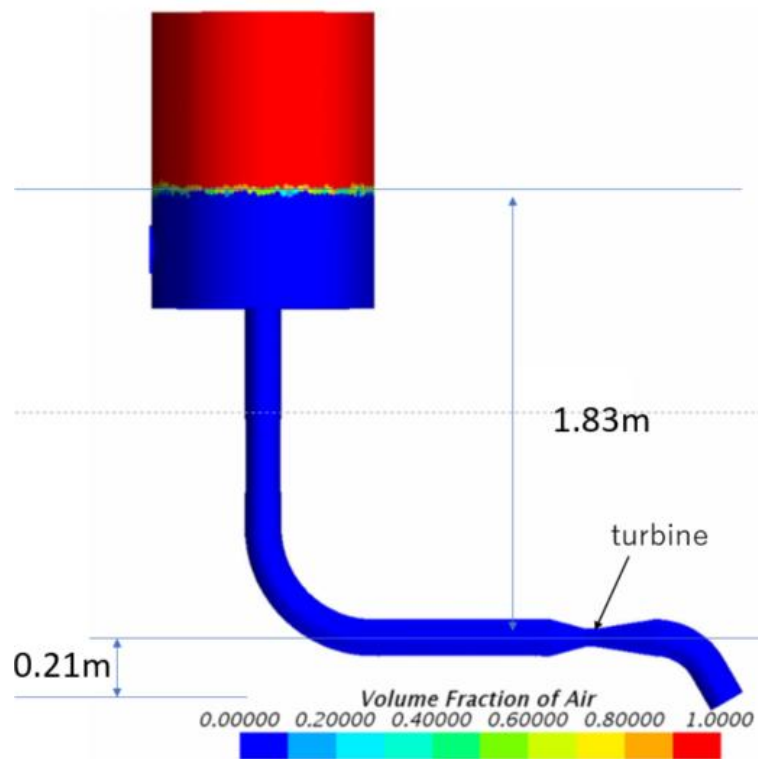


Figure 23 : Configuration of the system

Characteristic curve of 3-inch Kaplan turbine (Mass Flow Rate)

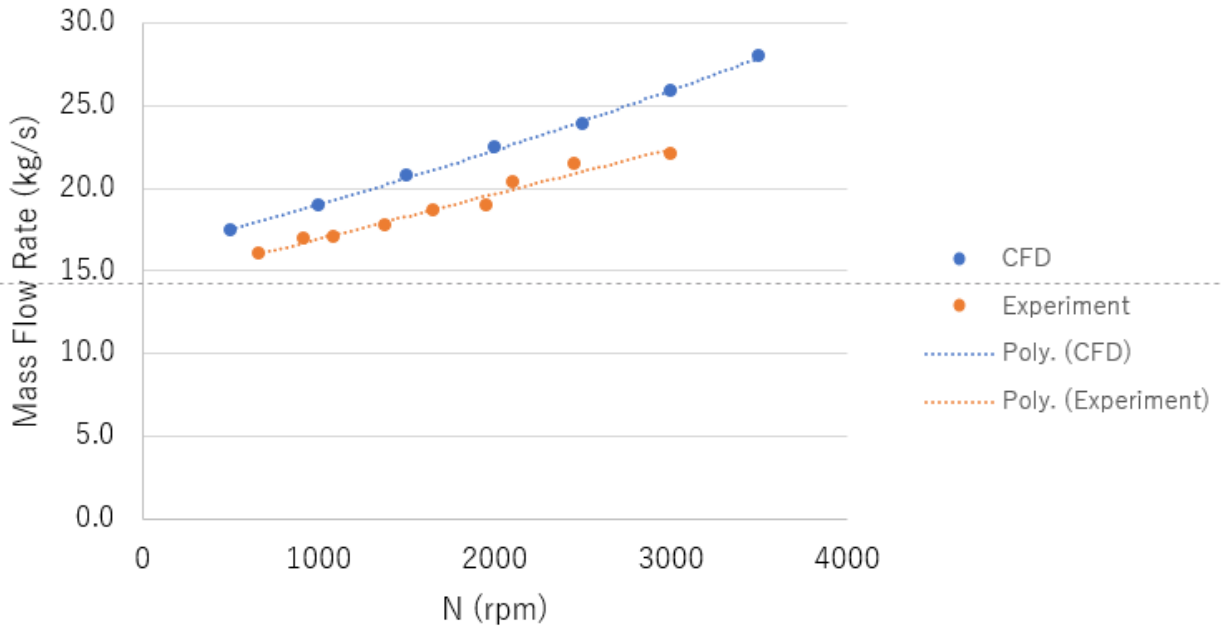


Figure 24: Mass flow rate of the CFD and experiment

Characteristic curve of 3-inch Kaplan turbine (Power)

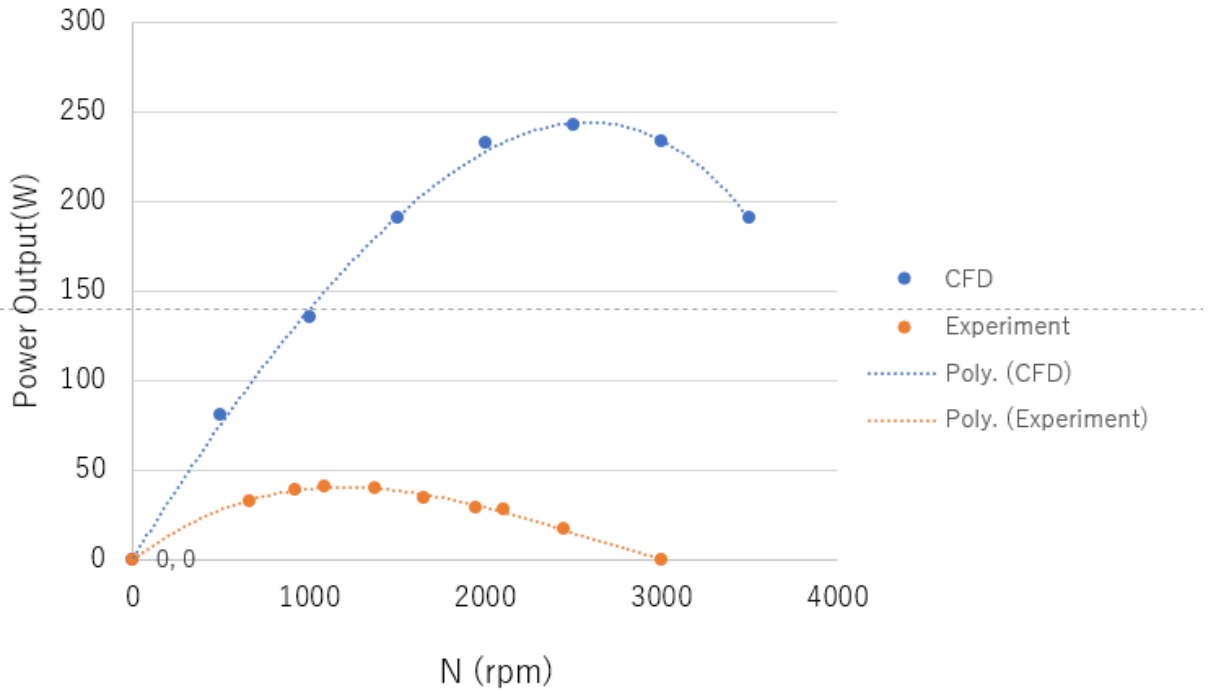


Figure 25 : Power output of the CFD and experiment

## 4.2. Presence of air

Figure 24 shows that the mass flow rate was less in the experiment than CFD. The flow observed during the experiment contained air, and it is the reason why the mass flow rate in the experimental test is less than CFD. Both the experimental and calculated flow rates are linear with rotational speed and can be approximated from the curves by linear approximation as following:

$$f_{\text{CFD}} = 0.0035N + 15.546 \quad (20)$$

$$f_{\text{EXP}} = 0.0027N + 14.20 \quad (21)$$

where  $N$  is the rotational speed, and  $f_{\text{CFD}}$  and  $f_{\text{EXP}}$  are the calculated and experimental flow rates, respectively. Defining the coefficient  $C_r$  as the ratio of mass flow rate with ideal condition (CFD) and mass flow rate from the experiment:

$$C_r = f_{\text{EXP}}/f_{\text{CFD}} \quad (22)$$

and assuming that the power output is proportional to the mass flow rate, we can obtain a corrected CFD power output,  $W_b$ , as taking into account the effect of air in the system. The correction is expressed in the equation below, and the results are plotted in Figure 26:

$$W_b = C_r \times W_{\text{CFD}} \quad (23)$$

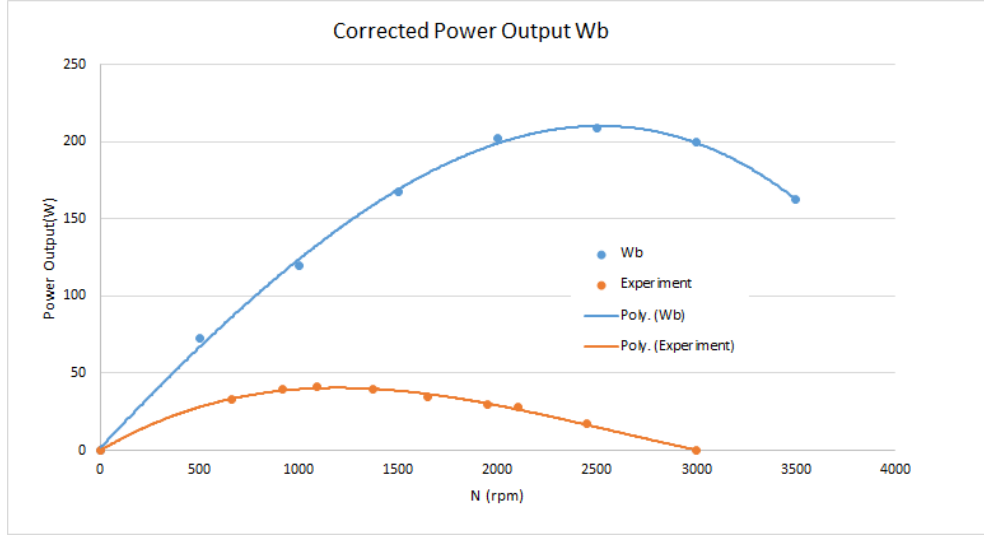


Figure 26: Comparison CFD corrected for presence of air with the experiment

### 4.3. Effect of friction

The part holding the shaft is so tight that the shaft could not rotate smoothly (see Figure 27) in the experiment. The friction here is considered as the cause of the energy loss.

Assuming the friction force  $F$  is constant, the energy loss  $E_{loss}(W)$  is defined as;

$$E_{loss} = F \times (\text{Rotational speed}) = F \times \left( \frac{N}{60} 2\pi R_{shaft} \right) \quad (24)$$

where  $R_{shaft}$  (m) is the radius of the shaft (0.0079m) and  $N$  is the rotational speed per minute (rpm). The constant force  $F$  can be determined from the experimental point where there is no output, 3,000 rpm, when all the energy is dissipated by friction. Hence, the friction force  $F$  can be estimated as following;

$$(W_b)_{3000rpm} = F \times \left( \frac{3000}{60} 2\pi \times 0.0079 \right) \quad (25)$$

$$\Leftrightarrow F = 80.6 \text{ (N)} \quad (26)$$

By substituting Eq. (26) into Eq. (24), the energy loss  $E_{loss}$  can be obtained. Then, the power output  $W_f$  corrected for friction can be obtained as;

$$W_f = W_b - E_{loss} \quad (27)$$

The profile of  $W_f$  is shown in Figure 28.

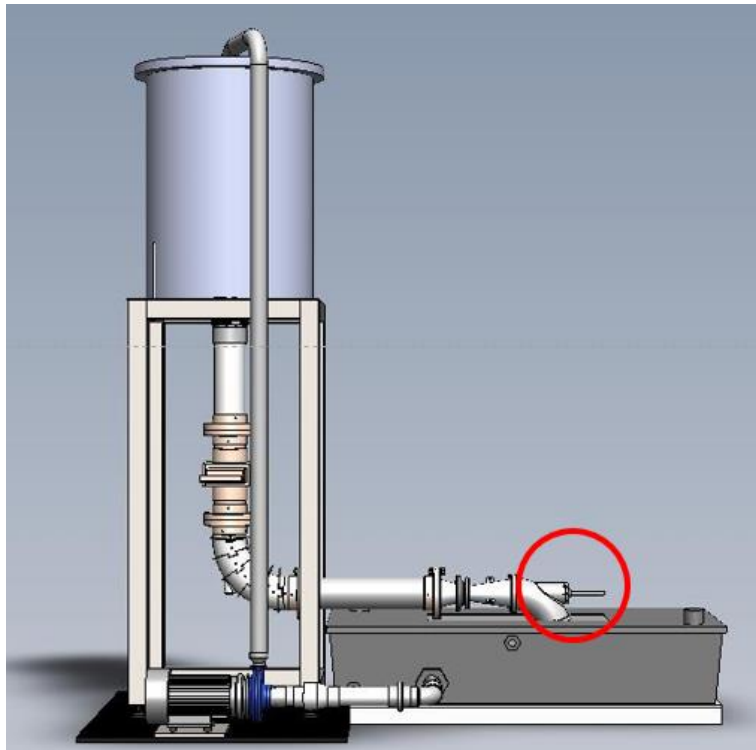


Figure 27 : The part causing friction

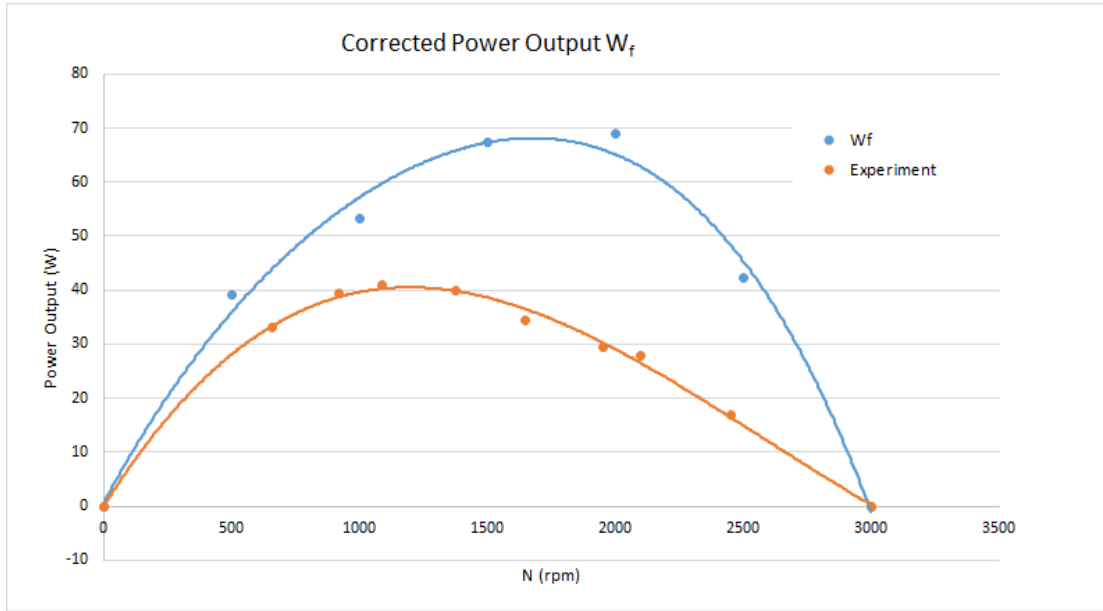


Figure 28 : Comparison CFD corrected for presence of air and friction with the experiment

#### 4.4. Error analysis

Table 2 sums up the measurement technique, measuring range and accuracy of various instruments used in the experiment for various parameters. Errors in experiments can rise from instrument conditions, calibration, environment, observation, and reading. The accuracy of the experiment has to be validated with the aid of error analysis using the method described by Moffat [18]

Table 2: Range and accuracy of tools used for the experiment

Quantity	Measuring range	Accuracy
Torque meter	0-10 (N · m)	±0.01(N · m) [19]
Tachometer	1-20,000 (rpm)	±0.05% [20]
Flow meter	4.7-1400 ( $\frac{kg}{s}$ )	±0.25% [21]

When the measurement value is described as  $\phi \pm U(\phi)$ , the fractional uncertainty is defined by Eq. (28). The fractional uncertainty gives a dimensionless number that shows the relative size of the uncertainty compared to the measurement. The torque from the experiment and its uncertainty and fractional uncertainty is shown in Table 3. The rotational speed N (rpm) from the experiment and its uncertainty and fractional uncertainty is shown in Table 4. The mass flow rate from the experiment and its uncertainty and fractional uncertainty is shown in Table 5.

$$(\text{Fractional uncertainty of } E) = \frac{U(\phi)}{\phi} \quad (28)$$

Table 3: Data from the experiment, uncertainty and fractional uncertainty of torque

Experiment Number	Torque (N · m)	Uncertainty (N · m)	Fractional uncertainty
1	0.000	±0.010	
2	0.066	±0.010	±15.09%
3	0.127	±0.010	±7.85%
4	0.144	±0.010	±6.92%
5	0.200	±0.010	±5.01%
6	0.278	±0.010	±3.60%
7	0.359	±0.010	±2.78%
8	0.410	±0.010	±2.44%
9	0.477	±0.010	±2.09%

Table 4: Data from the experiment, uncertainty and fractional uncertainty of rotational speed

Experiment Number	Rotational speed N (rpm)	Uncertainty (rpm)	Fractional uncertainty
1	3000	$\pm 1.500$	$\pm 0.05\%$
2	2450	$\pm 1.225$	$\pm 0.05\%$
3	2100	$\pm 1.050$	$\pm 0.05\%$
4	1950	$\pm 0.975$	$\pm 0.05\%$
5	1650	$\pm 0.825$	$\pm 0.05\%$
6	1375	$\pm 0.688$	$\pm 0.05\%$
7	1090	$\pm 0.545$	$\pm 0.05\%$
8	920	$\pm 0.460$	$\pm 0.05\%$
9	660	$\pm 0.330$	$\pm 0.05\%$

Table 5: Data from the experiment, uncertainty and fractional uncertainty of rotational mass flow rate

Experiment Number	Mass flow rate (kg/s)	Uncertainty (kg/s)	Fractional uncertainty
1	22.087	$\pm 0.055$	$\pm 0.25\%$
2	21.436	$\pm 0.054$	$\pm 0.25\%$
3	20.388	$\pm 0.051$	$\pm 0.25\%$
4	18.944	$\pm 0.047$	$\pm 0.25\%$
5	18.604	$\pm 0.047$	$\pm 0.25\%$
6	17.755	$\pm 0.044$	$\pm 0.25\%$
7	17.018	$\pm 0.043$	$\pm 0.25\%$
8	16.905	$\pm 0.042$	$\pm 0.25\%$
9	16.084	$\pm 0.040$	$\pm 0.25\%$

If the measured quantities  $\phi_1 \pm U(\phi_1)$ ,  $\phi_2 \pm U(\phi_2)$ , ...,  $\phi_n \pm U(\phi_n)$  are used to compute the result E which has the form expressed by Eq. (29), then the fractional uncertainty in E is given by Eq. (30). Since the power output (W) is calculated by Eq. (31), the fractional uncertainty of the power output can be calculated by Eq. (32). The fractional uncertainty of the power output was calculated by substituting the fractional uncertainty of torque and rotational speed from Table 3–Table 4 into Eq. (32), and Table 6 sums up the fractional uncertainty and uncertainty of power output. The power output considering the uncertainty is

showed in Figure 29.

$$E = C\phi_1^a \cdot \phi_2^b \dots \phi_n^d \quad (29)$$

$$\frac{U(E)}{E} = \pm \sqrt{\left[ a \frac{U(\phi_1)}{\phi_1} \right]^2 + \left[ b \frac{U(\phi_2)}{\phi_2} \right]^2 + \dots + \left[ d \frac{U(\phi_n)}{\phi_n} \right]^2} \quad (30)$$

$$W = \frac{L \cdot \pi \cdot N}{30} \quad (31)$$

$$\frac{W}{U(W)} = \pm \sqrt{\left[ \frac{U(L)}{L} \right]^2 + \left[ \frac{U(N)}{N} \right]^2} \quad (32)$$

Table 6: Data from the experiment, fractional uncertainty, and uncertainty of power output

Experiment Number	Power output (W)	Fractional uncertainty	Uncertainty (W)
1	0		
2	17	±0.151	±2.57
3	28	±0.079	±2.20
4	29.5	±0.069	±2.04
5	34.5	±0.050	±1.73
6	40	±0.036	±1.44
7	41	±0.028	±1.14
8	39.5	±0.024	±0.96
9	33	±0.021	±0.69

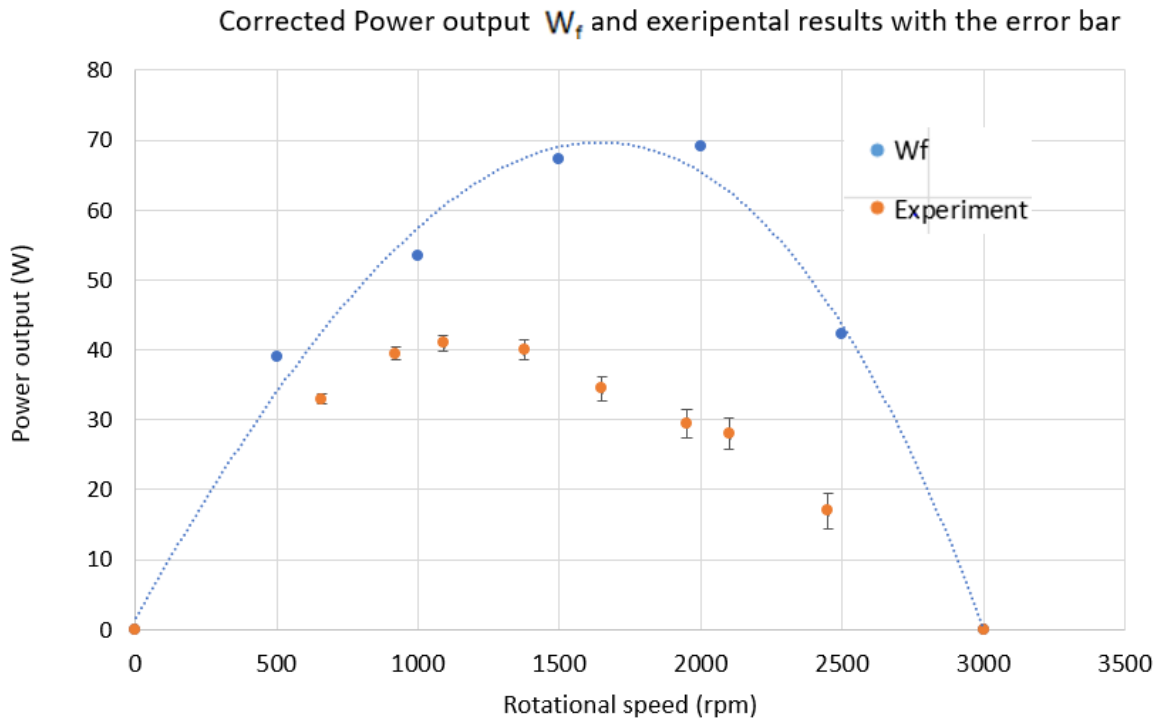


Figure 29 : Corrected power output  $W_f$  and experimental results with the error bar

## 4.5. Summary of experimental study

Test results from the experiment were initially far below CFD calculations. However, the difference can be explained by the presence of air in the system and friction. The presence of air could be reduced or eliminated with a redesign and would be expected to be less in a larger system. Friction is due mostly to the shaft, which is not necessary for the rim-drive system. Ultimately, with proper flow input and under the conditions set in the lab, a rim-drive turbine should, therefore, be able to produce 250 W with very low water head: 2.04.

## 5. Cavitation treatment by air injection

### 5.1. Phenomenon Description

Cavitation is caused by local vaporization of the fluid when the local static pressure of liquid falls below the vapor pressure of the liquid. Small bubbles or cavities filled with vapor are formed, which suddenly collapse on moving forward with the flow into regions of high pressure. These bubbles collapse with tremendous force, giving rise to as high a pressure as 1GPa [22]. In turbines, cavitation is most likely to occur at the suction side of blades. When cavitation occurs, it causes the undesirable effects such as local pitting of the metal surface, severe erosion [23–25], the vibration of the machine [26–28] and a drop of efficiency due to vapor formation, which reduces the effective flow areas [29–30]. The avoidance of cavitation in conventional designs is regarded as one of the essential tasks of turbine designers. Cavitation imposes a limitation on the design and working condition such as speed of rotations of the turbines [31]. In this study, the aeration treatment was investigated regarding the reduction of cavitation and improvement of the range of rotational speed that the system can run safely.

#### 5.1.1. Cavitation number

The cavitation number  $\sigma$  is used to characterize the potential of the flow to cavitate. It is a dimensionless number defined by Eq. (33). It expresses how close the pressure in the liquid flow is to the vapor pressure (and therefore the potential for cavitation).

$$\sigma = \frac{P_{\infty} - P_v}{\frac{1}{2} \rho_L U_{\infty}^2} \quad (33)$$

$U_{\infty}$ ,  $P_{\infty}$  and  $P_v$  are respectively a reference velocity, reference pressure and vapor pressure in the flow, respectively. (usually upstream quantities), and  $\rho_L$  is the liquid density. In this study, the velocity and pressure entering the rotor were chosen as  $U_{\infty}$  and  $P_{\infty}$  respectively.

## 5.1.2. Type of cavitation

### Vortex cavitation

Many high Reynolds number flows seen in industry contain a region of concentrated vorticity where the pressure in the vortex core is often considerably smaller than in the rest of the flow. Tip vortex cavitation is the form of cavitation inception occurs when a bubble is trapped into the low-pressure region located in the center of the tip vortex [32]. The tip vortices of ship's screws or pump impellers are a typical example of this (see Figure 30).

### Cloud cavitation

With a further reduction in the cavitation number, it follows that the entire core of the vortex is filled with vapor and becomes continuous due to the accumulation of individual bubbles, as illustrated by the picture in Figure 31, namely cloud cavitation.

### Sheet cavitation

Another class of large-scale cavitation structures is that which occurs when a wake or region of separated flow fills with vapor. Cavitation took place while a single vapor-filled separation zone as illustrated in Figure 32 is called sheet cavitation.

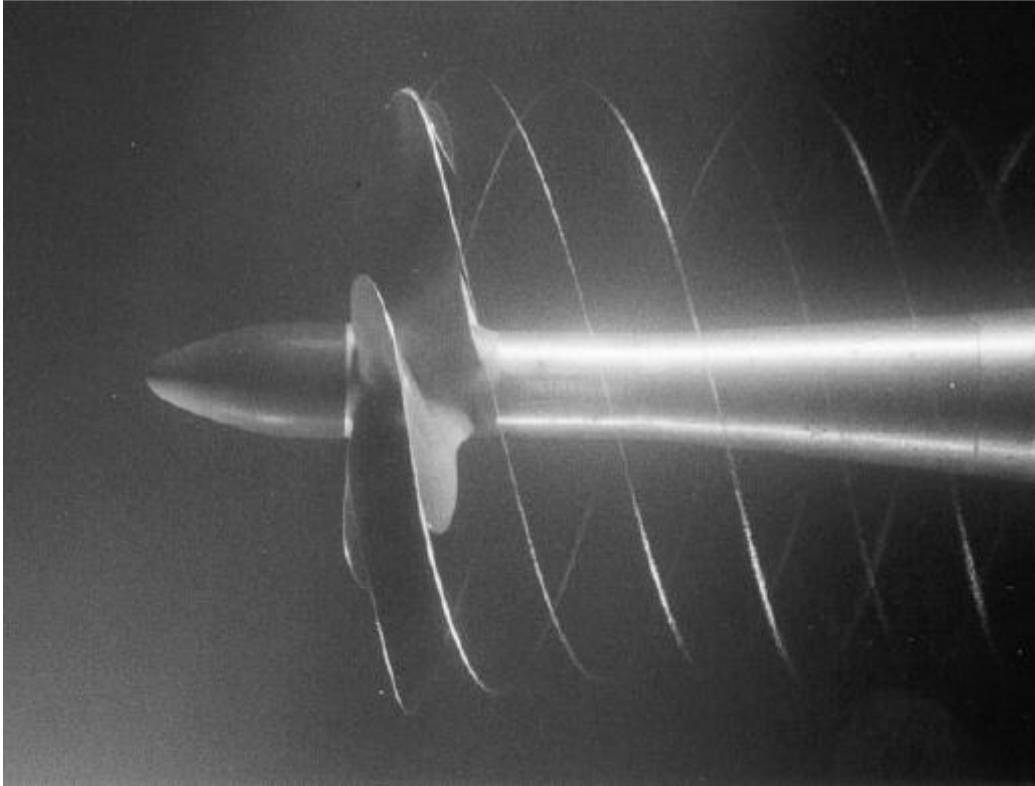


Figure 30: Tip vortex cavitation on a propeller [b]

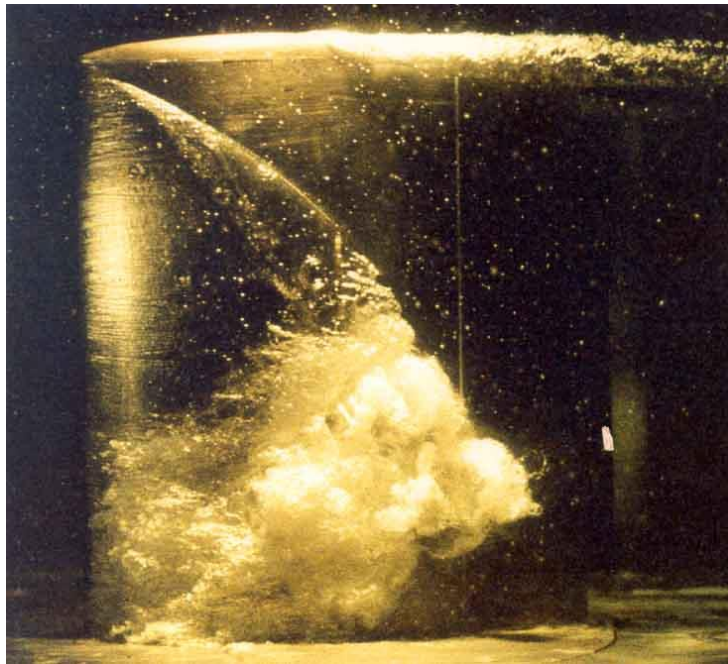


Figure 31: Cavitation cloud on the suction surface of a hydrofoil [3]

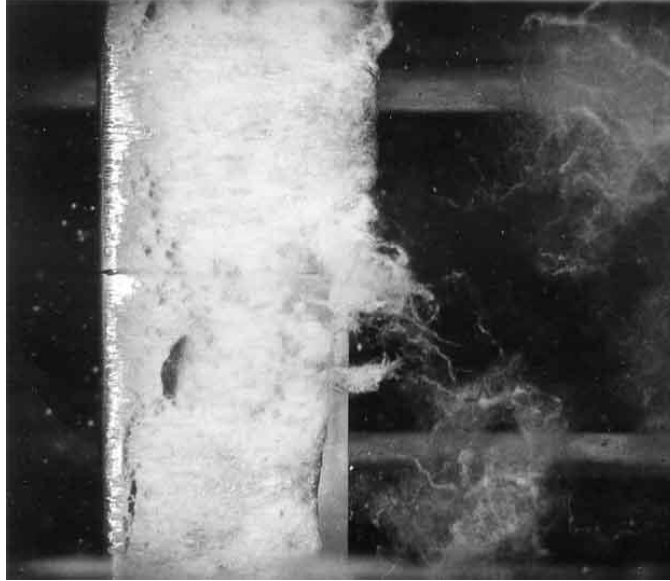


Figure 32: Sheet cavitation on the suction surface of a hydrofoil [34]

## 5.2. Computational Fluid Dynamics (CFD) model setting up

### 5.2.1. Modeling

Same as the study for the hydro turbine system with a low head, CFD approach was performed by using the commercial codes of the multidisciplinary STAR CCM+, choosing Volume of Fluid (VOF) and Large Eddy Simulation (LES) to solve the unsteady multi phase turbulent flow in this study, too. The vapor pressure of water was set as 3.2 kPa, assuming the temperature of the water is 298(K). The time step was set as  $4 \times 10^{-5}$  (s). As Figure 33 shows, the Convective Courant Number is less than 1.0 almost all over the area of the runner, so the time step is small enough. The rotational speed N was set in the range of 1000–4000rpm. The stator, runner, intake and outlet tube are the same as those used in the study on rim-drive.

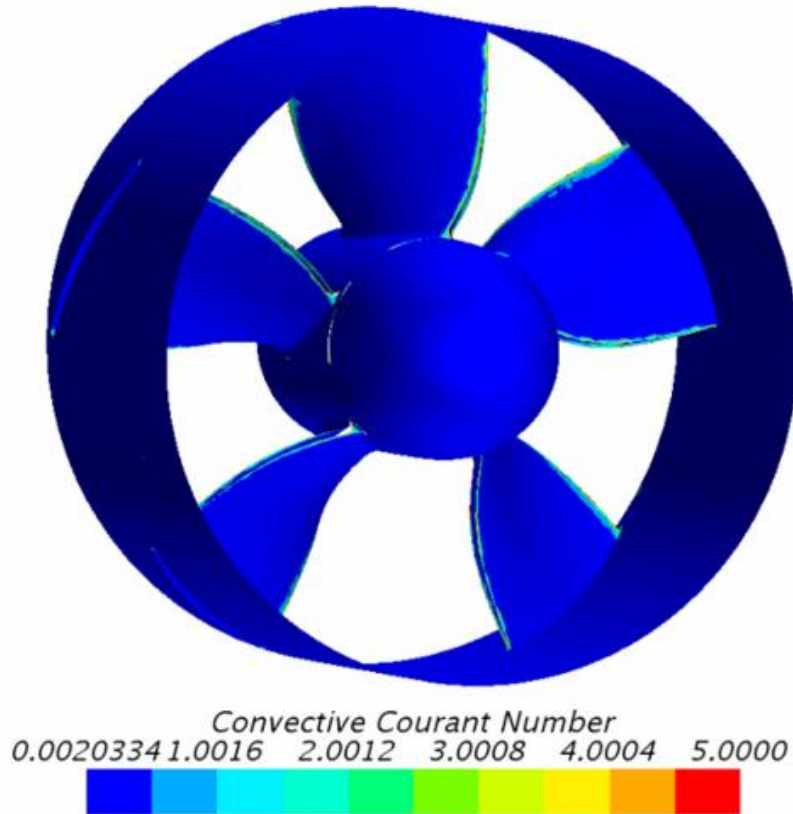


Figure 33 : Convective Courant Number on the stator when it runs at 3000rpm without any air injection

### 5.2.2. Configuration and mesh

Since cavitation is a complex phenomenon which includes the formation, separation and collapse of the cavitation bubble, it is necessary to use very fine mesh to capture the characteristics of the flow phenomenon. Hence, to make the number of cells for the simulation smaller, just the intake tube, stator, turbine and draft tube were selected as calculation domain (see Figure 34). Figure 35 shows the VVF over the suction side of the turbine blade when the rotational speed is 1000rpm, and these value of VVF were used for the mesh independent study. The 3.6Million cells case was selected as the mesh for the latter work because of the

minimum deviation from the average (1.3 %), the better  $Y^+$  representation than the 1.9 million case, and the 67% less time consuming compared to the 5.2Million case. The  $Y^+$  was kept less than 2.0 with using 3.6 million cells (see Figure 36)

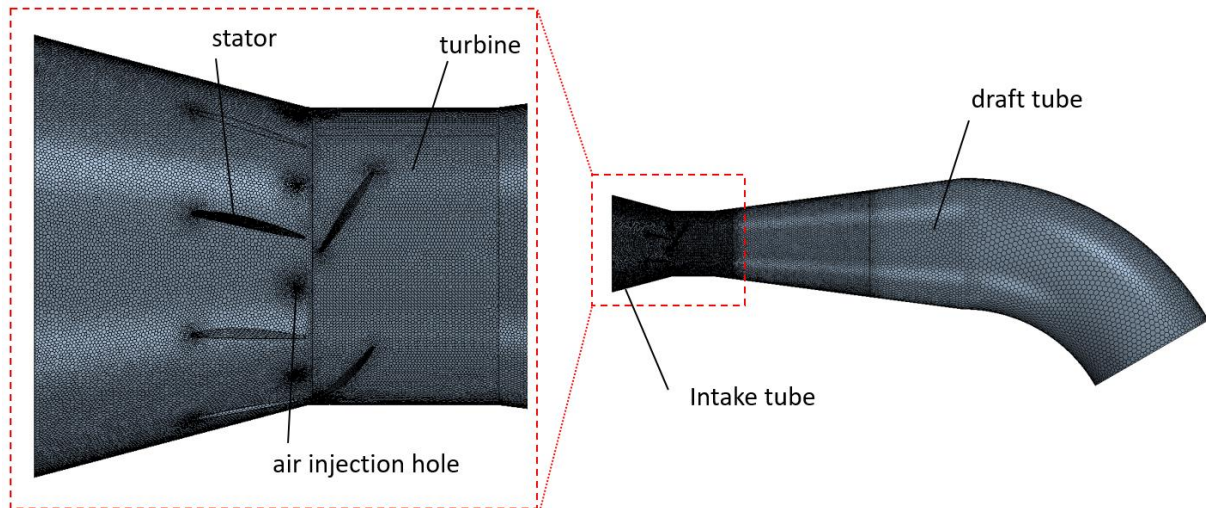


Figure 34 : Computational domain and the mesh around the system

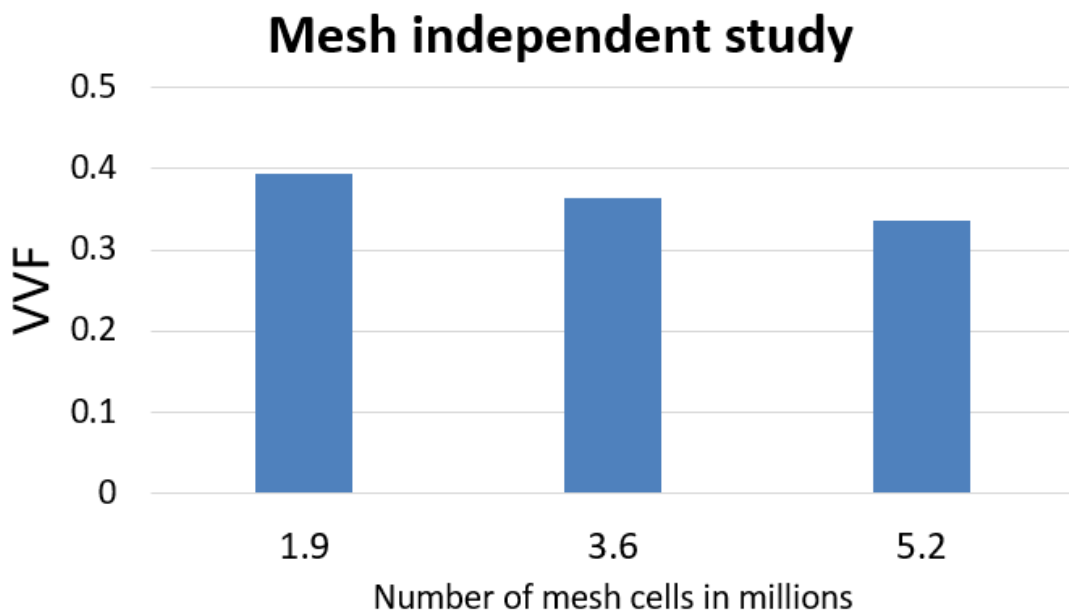


Figure 35 : VVF in different mesh conditions; 1.9M, 3.6M, 5.2M

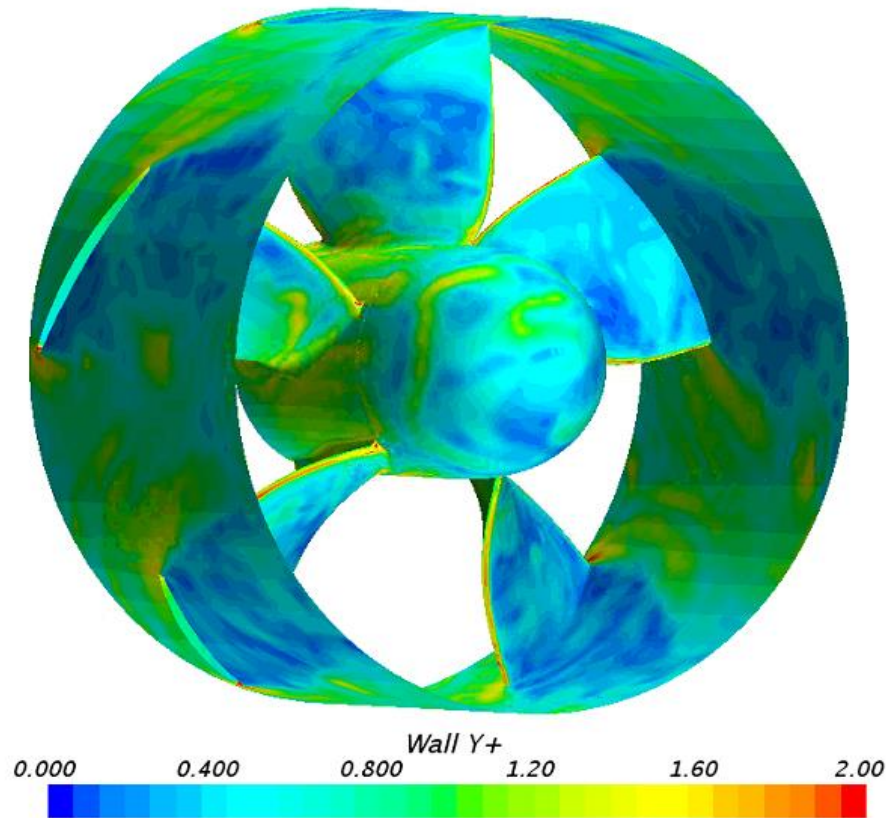


Figure 36 : Wall Y+ on the turbine when it runs at 1000rpm

### 5.2.3. Design of air injection holes

Since the turbine used in this study has a rim, it is difficult and not practical to make air injection holes right above the turbine blade. Hence air injection holes were made at upstream of the turbine. In this thesis, two kinds of design of air injection holes were investigated. Firstly, air injection holes were set between blades of the stator (Design A). The diameter of each hole is 1mm. Since the stator has nine blades, nine air injection holes were set (see Figure 37). Secondly, air injection holes were made on the blades of the stator (Design B). In this design, each blade has three injection holes at the 0.015m, 0.025m and 0.035m from the center

of the stator respectively. The position of these holes can be described by the dimensionless parameter  $L_a$ , which is defined by Eq. (34) (see Figure 38). The diameter of these holes is 1mm.

$$L_a = \frac{D_a}{R_t} \tag{34}$$

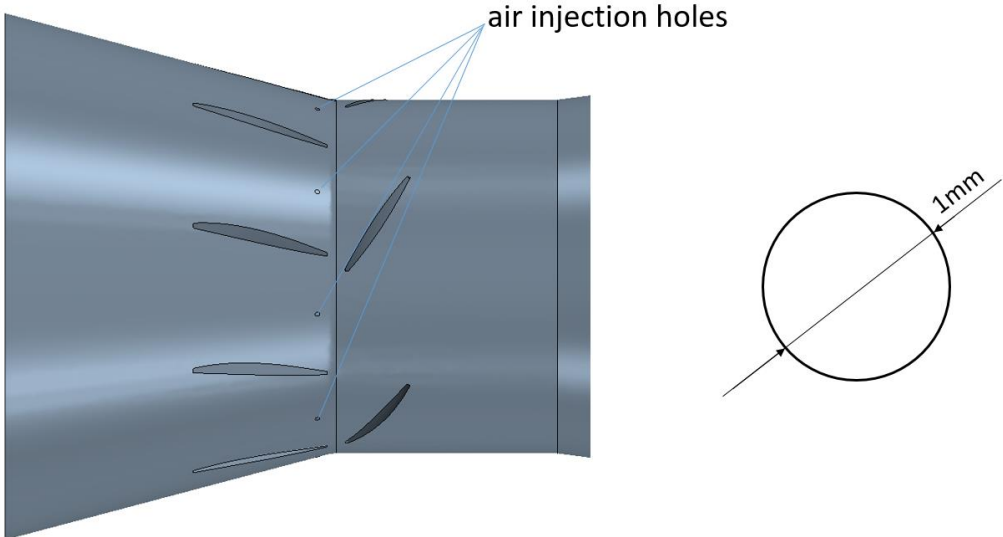


Figure 37: Configuration of the air injection hole of Design A

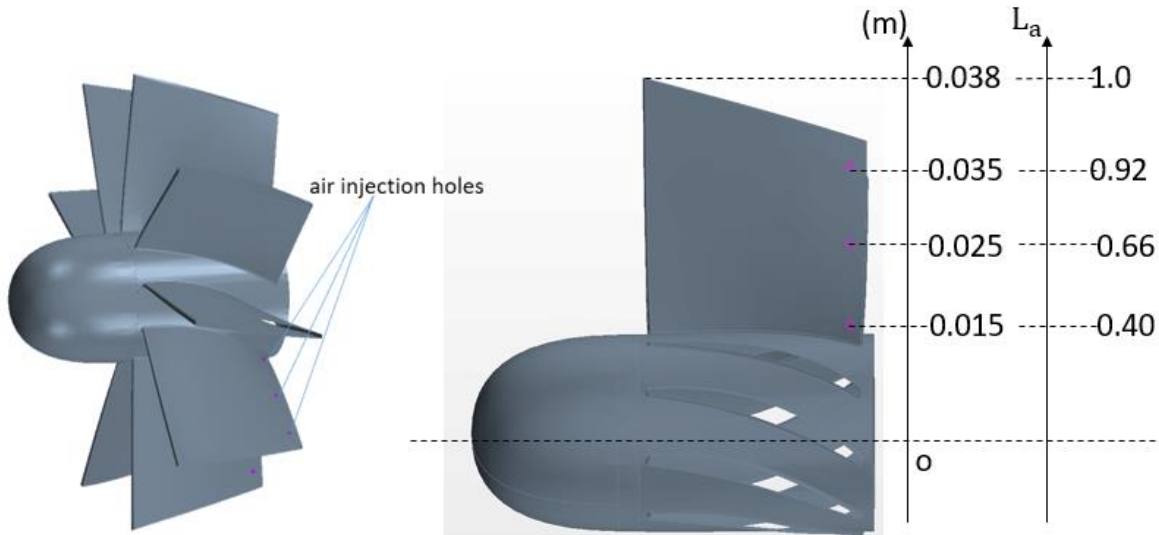


Figure 38: Configuration of the air injection hole of Design B

#### 5.2.4. Boundary conditions

82.7 (kPa) was applied at the inlet as the boundary condition. As the outlet condition, atmospheric pressure outlet was used. Non-slip boundary condition was applied on the wall.

### 5.3. Result and Discussion

#### 5.3.1. No air injected case

No air injected case was first investigated to get the baseline data. The rotational speed of the turbine was changed in the range of 1000rpm to 4000rpm. The quasi-steady state is reached at 0.18(s), and data later than this time was used to get time averaged properties. The cavitation number in each rotational speed case, calculated from the mean velocity and pressure entering the turbine, are shown in Table 7. The patterns of cavitation are shown in Figure 39 and Figure 40. As Figure 39 shows, stronger type of cavitation (sheet cavitation) was

found for the higher rotational speed of the turbine, corresponding to the decrease of cavitation number. The difference of cloud cavitation and sheet cavitation can be seen in Figure 40. When the rotational speed is 1000rpm, the behavior of cavitation is randomly fluctuating due to the vapor cloud cycle (formation, separation, and collapse). However, when the turbine is rotating at higher speed (3000rpm or 4000rpm), the vapor volume fraction (VVF) on the suction side of the blade is more stable, and more than 75% of the area of the suction side is covered with vapor. As the baseline data, the VVF over the blade and hub, power output and mass flow rate of water were obtained (see Table 8)

Table 7 : Cavitation number in different rotational speed

	1000rpm	2000rpm	3000rpm	4000rpm
Cavitation number	2.71	2.05	1.55	1.17

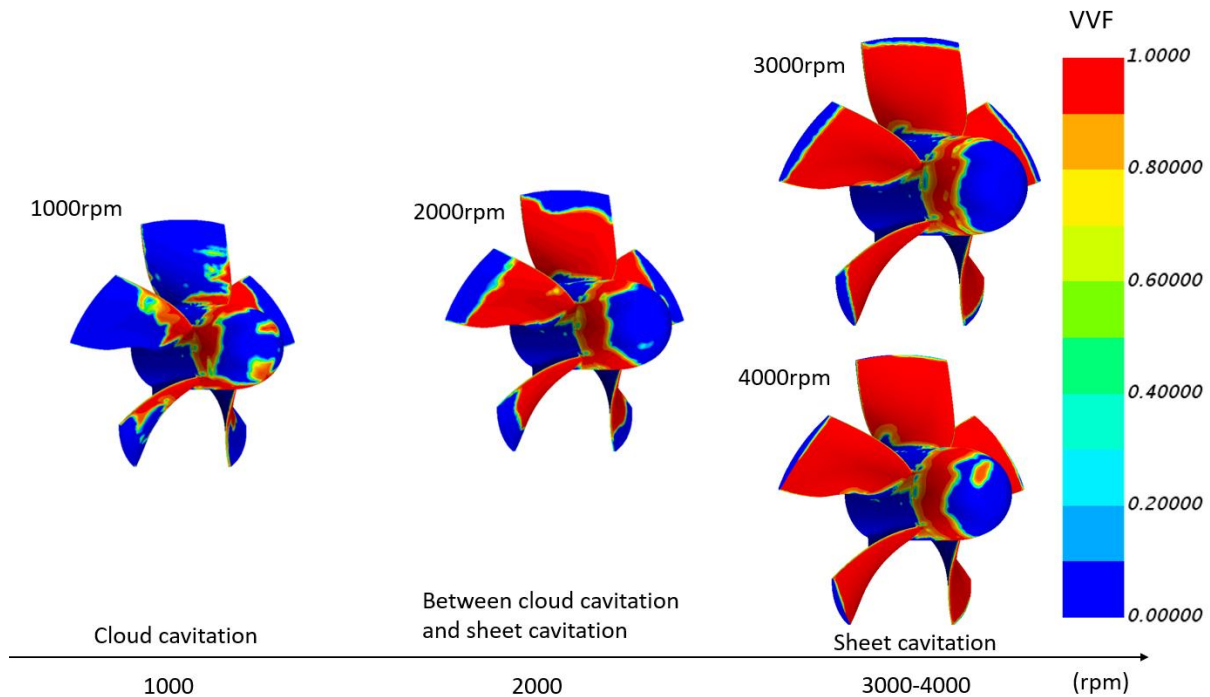


Figure 39: Contour plots of VVF without air injection when the rotational speed is 1000rpm – 4000rpm, real time is 0.3 (s)

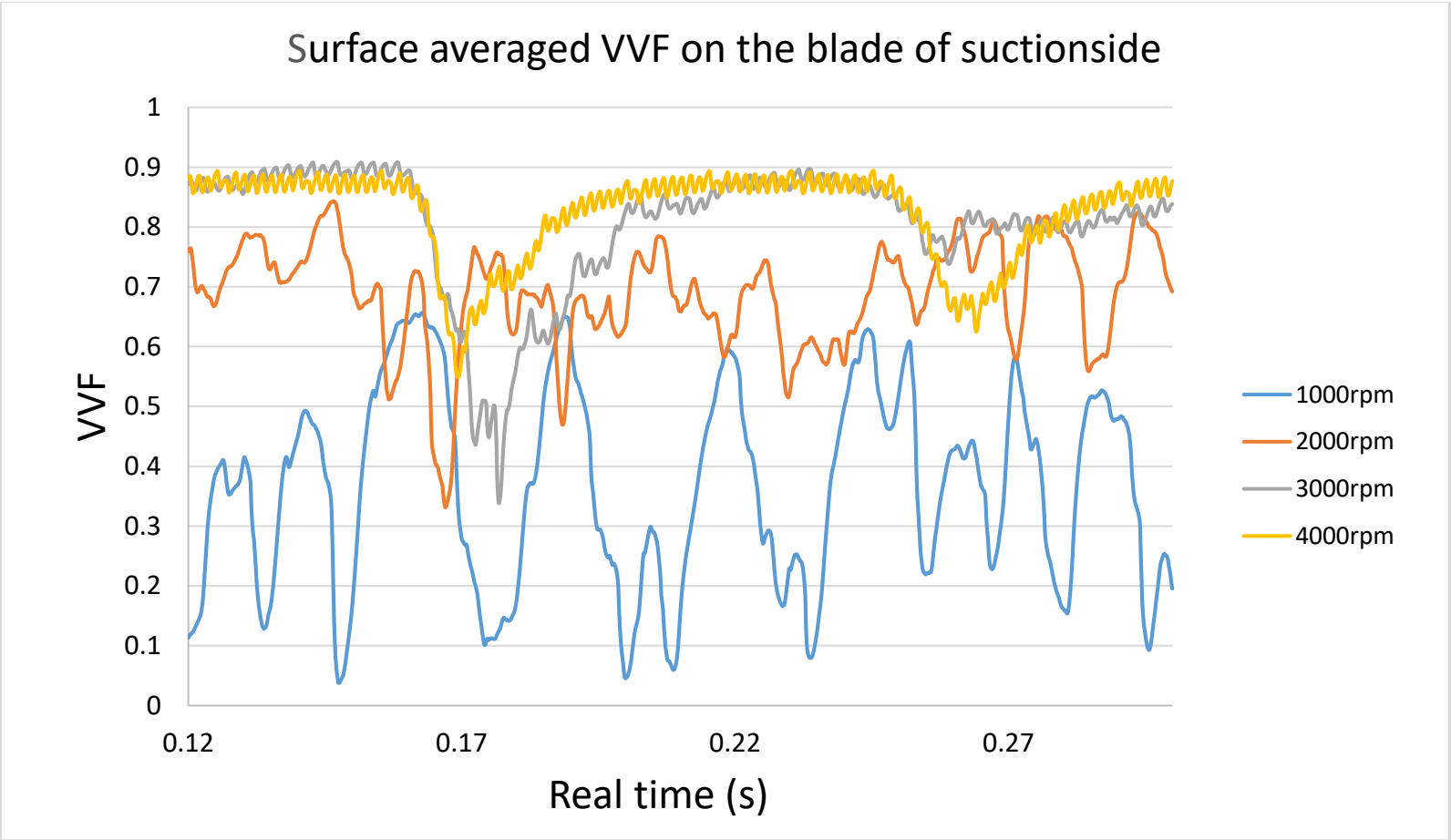


Figure 40 : Time history for the surface averaged VVF over the suction side of the blade

Table 8: VVF, power, and mass flow rate for No air injected case

No Air	1000rpm	2000rpm	3000rpm	4000rpm
VVF (blade)	0.363	0.692	0.810	0.817
VVF (hub)	0.343	0.321	0.295	0.225
P(W)	612.9	1103.4	1414.2	1511.7
Mass Flow Rate (kg/s)	35.23	39.14	42.99	46.55

### 5.3.2. Fluctuation of pressure on the air injection hole

Firstly, 51.7(kPa) gauge pressure was applied on the air injection holes with turbine rotating at 2000rpm in the Design A, and VVF over the blade and hub, Power output and mass flow rate of water were obtained (Table 9). In this case, the surface and time averaged cavitation over the suction side of the blade is 0.652, while that of baseline data is 0.692 (percentage of reduction is 5.8%). The aeration treatment could not eliminate cavitation over the suction side of the blade well because of the fluctuation of pressure on the air injection holes. As Figure 41 shows, the pressure on the air injection hole fluctuates when the blades of turbine pass the hole because of the difference in pressure between the suction side and pressure side of the blade (see Figure 42). The pressure reaches the peak right after the passage of the blade and going down as the suction-side of the next blade get closer to the hole. The amount of air injected into the system is determined by the difference in pressure between the air injection hole and liquid water around the air injection hole. Since constant pressure is applied to the air injection holes, the mass flow rate of air from the hole also fluctuates corresponding to the fluctuation of pressure on that (see Figure 43). In order to clear the correlation between the pressure and the mass flow rate of air, both pressure and mass flow rate of air were normalized by their mean values, which are 122.6kPa and 0.178g/s,

respectively. Profile of them is shown in Figure 44, denoting the correlation of them. When the pressure of liquid water near the hole is high (time 0.271s), the mass flow rate of air from the hole is small. On the other hand, when the pressure is low (time 0.275), the mass flow rate of air is significant. Figure 45 visualize how the injected air travels in the system. The air injected during time 0.273s to 0.276s, which makes an enormous cloud of air, goes through the system without contacting the blades of the turbine. Hence, the aeration treatment, in this case, could not eliminate cavitation over the blades well. If it is possible to control the position of the air injection holes to make the cloud of air injected during the pressure of water near the holes are small contact the blades of the runner, it would be a way to utilize aeration efficiently. However, since this study focuses on the effect of air on cavitation around the turbine, enough amount of air (68.9kPa and 137.9kPa for the Design A and 103.4kPa and 137.9kPa for the Design B) were injected in the following chapter.

Table 9: VVF, power, and mass flow rate; Design A, 51.7(kPa) on air injection holes

VVF (blade)	VVF (hub)	Power (W)	Mass flow rate (kg/s)
0.652	0.317	1102.1	38.72

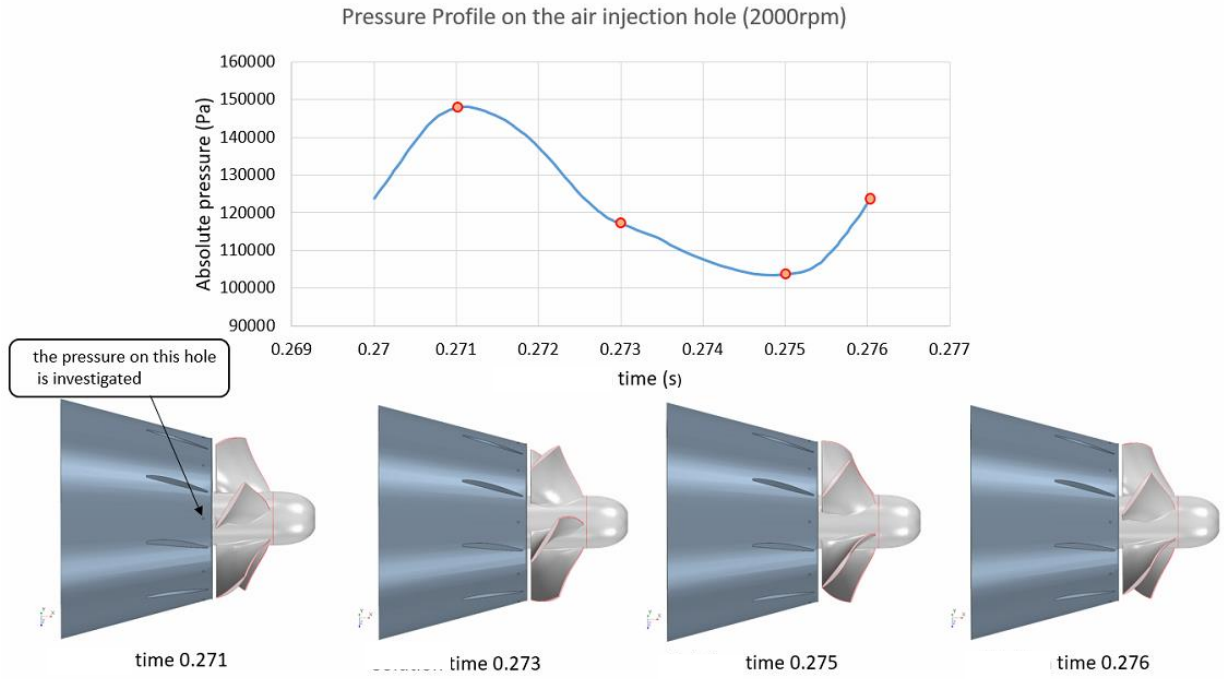


Figure 41: Profile of pressure on the air injection hole

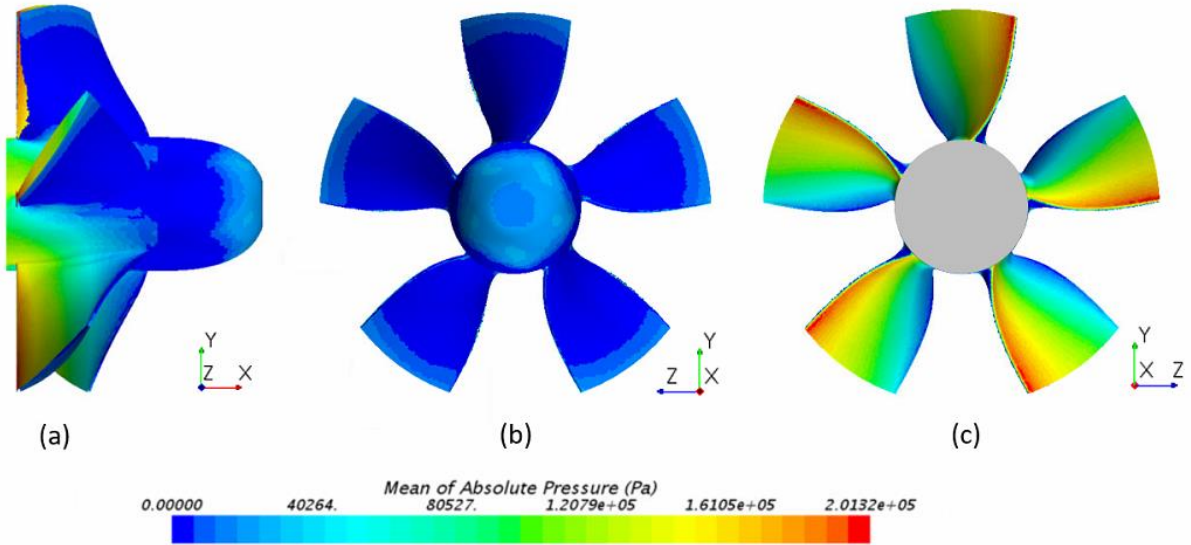


Figure 42 : Contour plots of time averaged absolute pressure over the turbine

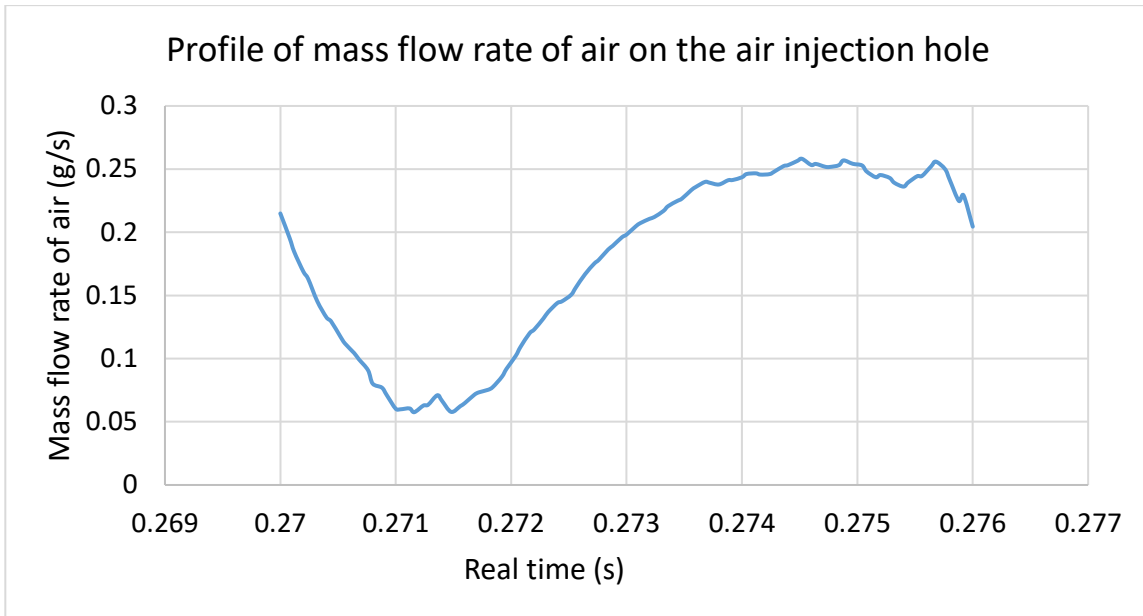


Figure 43 : Profile of mass flow rate of air from the air injection hole when the applied pressure on the holes is 51.7kPa and the turbine runs at 2000rpm

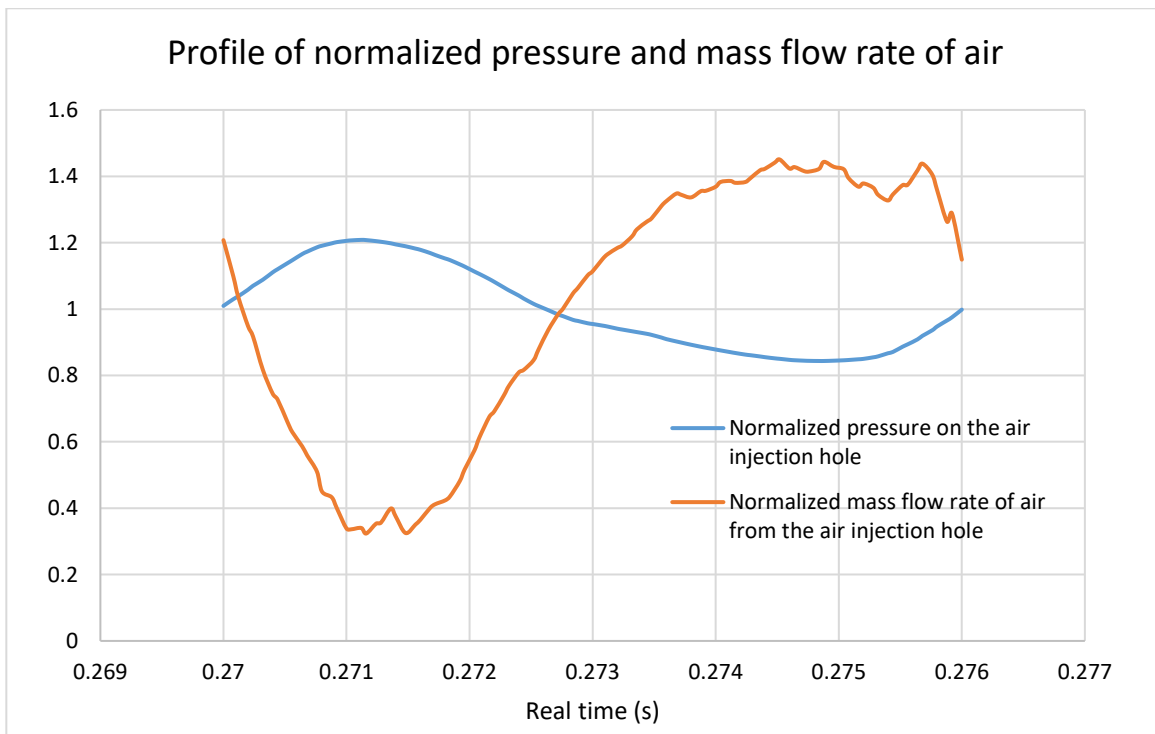


Figure 44 : Profile of mass flow rate of air from the air injection hole when the applied pressure on the holes is 51.7kPa and the turbine runs at 2000rpm

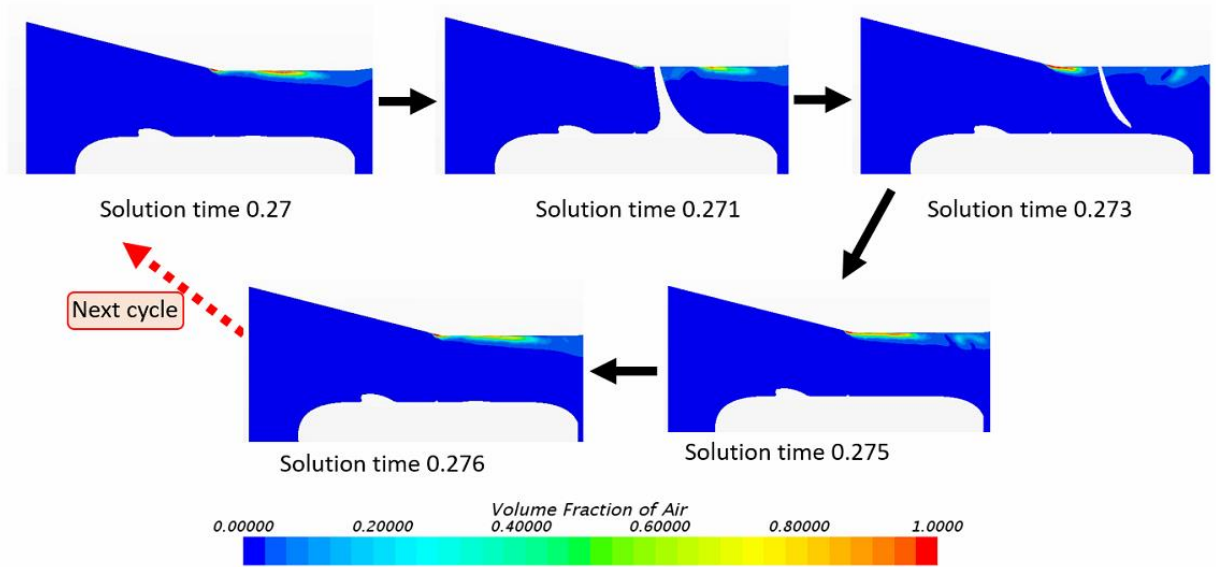


Figure 45: Traveling air injected into the system

### 5.3.3. Design A

In this design, two kinds of inlet pressure, 68.9kPa, and 137.9kPa gauge pressure, on the air injection holes were tested. Air volume fraction (AVF) at the outlet, vapor volume fraction (VVF) over the suction side of the blade and hub, mass flow rate of water, and power output were investigated with comparison with the baseline data (No-air case).

#### 5.3.3.1. Movement of air injected from the upstream of the turbine

In the study of aeration treatment for tip vortex cavitation, the air injection holes were made above the turbine blade, and the air was injected directly to the area cavitation happens [7]. However, the turbine used in this study has a rim around the turbine blades. Hence, it is difficult and not practical to make air injection holes above the turbine blade. That is why the air injection holes were made upstream of the turbine. Hence, it is necessary to investigate

the movement of air injected from the upstream of the turbine to check if air can eliminate cavitation.

The surface and time averaged VVF, AVF and pressure on seventeen cross sections, shown in Figure 46, were investigated to examine the movement of air injected from upstream of the turbine. The seventeen cross sections were set from 0.01m ( $x/R_t=0.263$ ) to 0.09m ( $x/R_t=2.37$ ) in x direction. Figure 47 shows the VVF over these cross sections. Cavitation starts to happen at  $x=0.01$ m ( $x/R_t=0.263$ ), which is the starting position of turbine blade, and the volume of vapor increases due to cavitation happening on the turbine blades and the VVF reaches the maximum value at  $x=0.025$ m ( $x/R_t=0.658$ ), which is the ending position of the turbine blades. Then, the VVF decreases after  $x=0.025$ m ( $x/R_t=0.658$ ) due to the collapse of cavitation bubbles (see Figure 47). The pressure profile over the cross sections is shown in Figure 48. Due to the cavitation bubble, which has less pressure than liquid water, the value of pressure reaches the minimum at  $x=0.025$ m ( $x/R_t=0.658$ ). Because of the pressure gradient shown in Figure 48, the air injected into the system from upstream of the turbine stayed or sucked at around  $x=0.025$ m ( $x/R_t=0.658$ ) and eliminate cavitation (see Figure 47 and Figure 49).

The movement of air at the cross section at  $x=0.01$ m ( $x/R_t=0.263$ ) was also investigated to verify that air from the upstream can eliminate cavitation. Figure 50 shows volume fraction scenes of the three fluids (air: blue, liquid water: green, vapor: red) by

introducing  $f_c$ , which is defined by Eq. (30). This figure shows the movement of air getting sucked into the suction side of the blade and reducing cavitation.

$$f_c = f_w + 2f_v \tag{35}$$

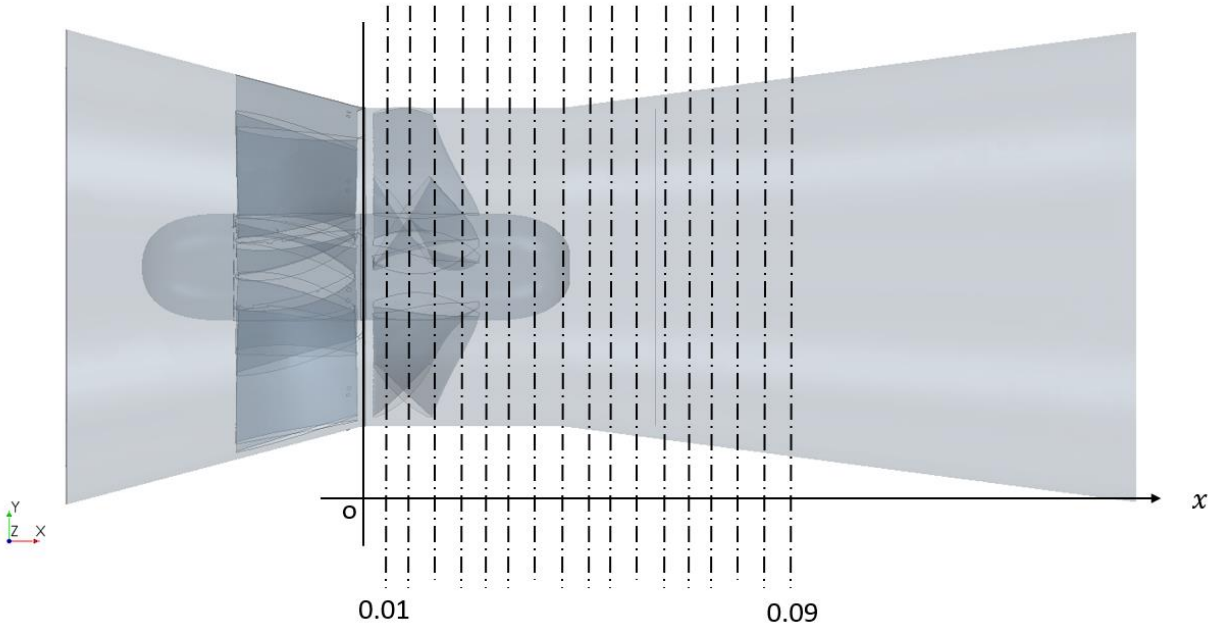


Figure 46: 17 cross sections over the runner and draft tube

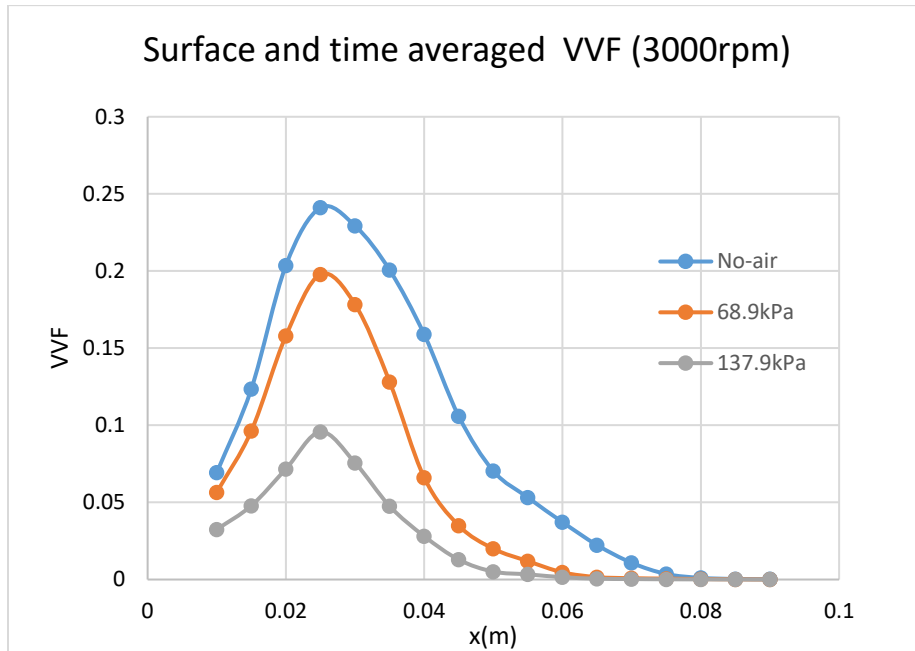


Figure 47 : profile of surface and time averaged VVF when the rotational speed is 3000rpm

### Surface and time averaged absolute pressure (3000rpm)

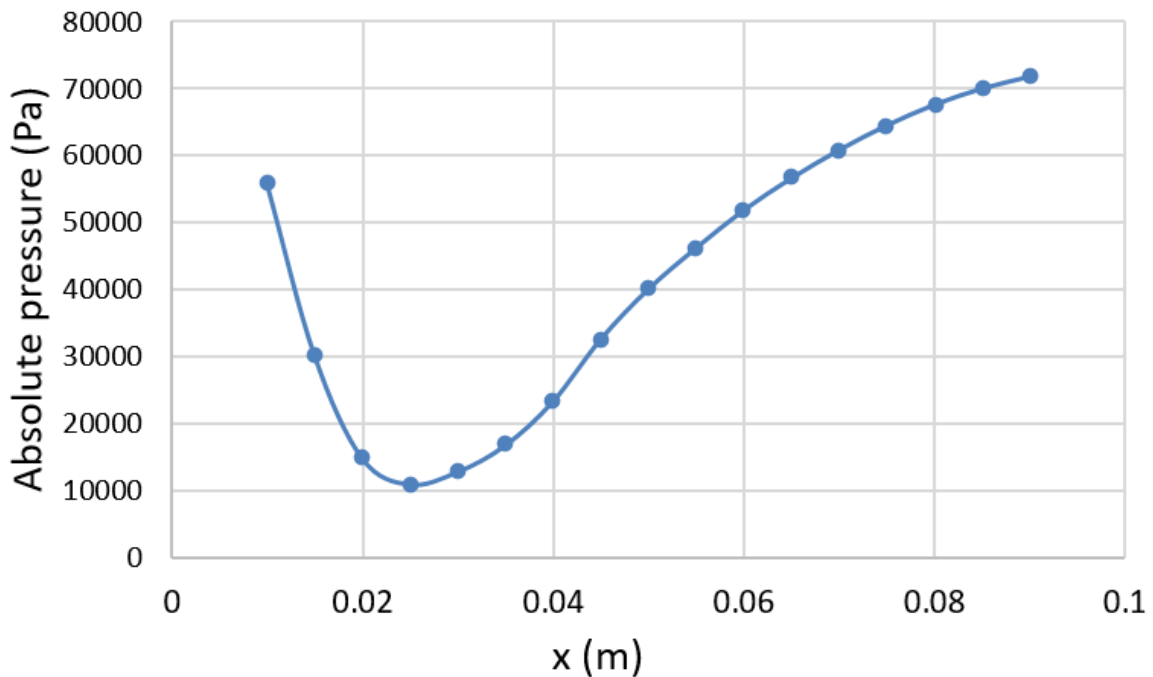


Figure 48 : Profile of surface and time averaged absolute pressure at each cross section when the rotational speed is 3000rpm, No-air case

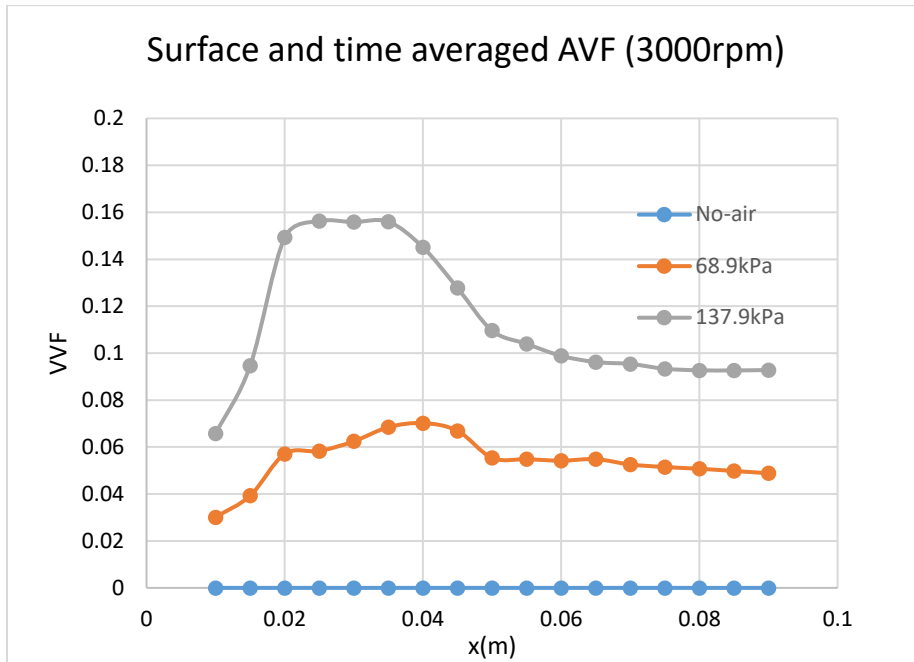


Figure 49 : Profile of surface and time averaged AVF when the rotational speed is 3000rpm

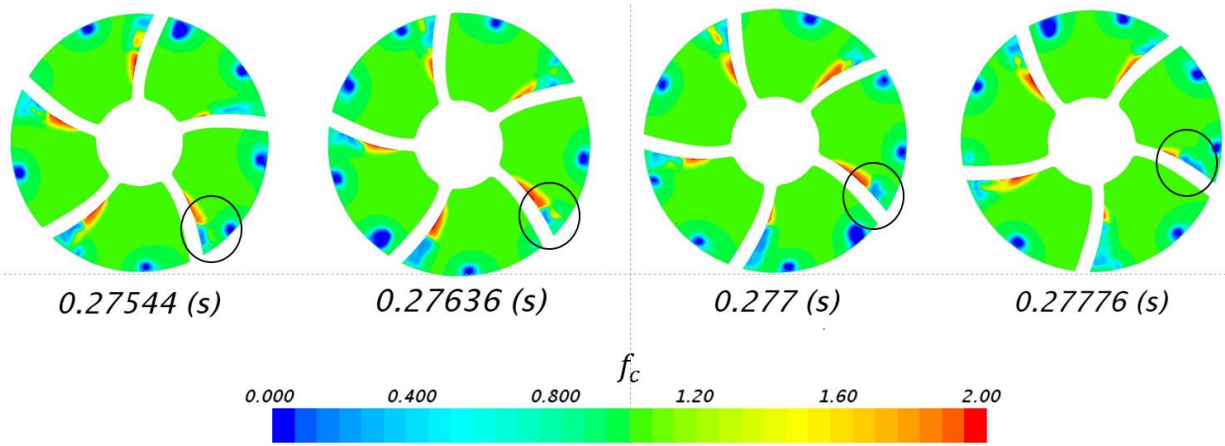


Figure 50: Contour plots of  $f_c$  at cross section of the turbine (the rotational speed is 3000rpm and pressure on the air injection holes is 137.9kPa)

### 5.3.3.2. Cavitation over the blade and hub

The results of each rotational speed are shown in Table 10– Table 13, respectively. The percentage change (VVF increase, Mass flow rate increase and Power increase) is based on the No–air result as a reference. As Table 10–Table 13 show, while 137.9kPa case can eliminate cavitation at most 50.4% over the blade, 68.9kPa case is just able to reduce cavitation at most 11.9%. Especially when the rotational speed is 1000rpm, the percentage of reduction of VVF over the blade is small; 1.1% by 68.9kPa air injection. The reason why 68.9kPa case cannot reduce cavitation over the blade can be explained by the depth of air penetration and cavitation pattern. When the rotational speed is 1000rpm, cavitation happens around the joint of the turbine blades and the hub, not around the tip of the turbine blades. However, as Figure 51 visualizes, air injected into the system by 68.9kPa can not penetrate deep enough to reach around the joint. Hence, pressurized air by 68.9kPa is not able to eliminate cavitation over the blade well. On the other hand, air injected by 137.9kPa can penetrate deep enough to cover the whole suction side of the blade; therefore Missing subject can eliminate cavitation more than 68.9kPa case (see Figure 51). When the rotational speed is higher than 1000rpm, cavitation can be seen near the tip of the turbine blades too. Hence, 68.9kPa case can also reduce cavitation more than it can when the rotational speed is 1000rpm. However, as mentioned before, the depth of penetration of air by 68.9kPa injection is just around the tip of the blade. That's why the area aeration treatment by 68.9kPa can eliminate cavitation is limited around the tip of the blades, while 137.9kPa pressure inlet can inject air deeper and eliminate cavitation more (see Figure 52).

While aeration eliminated cavitation over the blade, cavitation over the hub was increased in some cases (see Figure 53 and Figure 54). Figure 55 is the contour plots of the time averaged AVF over the runner and the cross sections of it when the rotational speed is 1000rpm, and the air is injected by 137.9kPa. These four cross sections a, b, c and d were set at 0.01m, 0.015m, 0.02m, 0.025m in x direction respectively. This figure shows that air could reach to the blade only. Hence, cavitation over the blade was directly reduced by pressurized air, but cavitation over the hub was changed not by pressurized air but by the change of fluid flow pattern caused by the aeration.

Table 10: Air injection Design A compared to No-air case when the rotational speed is 1000rpm

1000rpm	No-air	68.9kPa	137.9kPa
AVF at outlet	0	0.031	0.082
VVF (blade, hub)	0.363, 0.343	0.359, 0.376	0.215, 0.344
% VVF increase	0, 0	-1.1, 9.6	-40.8, 0.3
Mass flow rate (kg/s)	35.23	34.65	33.93
% Mass flow rate increase	0	-1.7	-2.1
Power (W)	612.9	611.2	602.6
% Power increase	0	-0.3	-1.7

Table 11: Air injection Design A compared to No-air case when the rotational speed is 2000rpm

2000rpm	No-air	68.9kPa	137.9kPa
AVF at outlet	0	0.035	0.081
VVF (blade, hub)	0.692, 0.321	0.609, 0.317	0.457, 0.297
% VVF increase	0, 0	-11.9, -1.3	-54.3, -7.5
Mass flow rate (kg/s)	39.14	38.36	37.60
% Mass flow rate increase	0	-2.0	-3.9
Power (W)	1103.4	1099.2	1085.3
% Power increase	0	-0.4	-1.6

Table 12: Air injection Design A compared to No-air case when the rotational speed is 3000rpm

3000rpm	No-air	68.9kPa	137.9kPa
AVF at outlet	0	0.040	0.081
VVF (blade, hub)	0.810, 0.229	0.730, 0.187	0.498, 0.100
% VVF increase	0, 0	-9.9, -36.6	-38.5, -56.3
Mass flow rate (kg/s)	42.99	41.92	40.92
% Mass flow rate increase	0	-2.5	-4.8
Power (W)	1414.2	1412.9	1408.2
% Power increase	0	-0.1	-0.4

Table 13: Air injection Design A compared to No-air case when the rotational speed is 4000rpm

4000rpm	No-air	68.9kPa	137.9kPa
AVF at outlet	0	0.048	0.073
VVF (blade, hub)	0.817, 0.225	0.741, 0.106	0.569, 0.115
% VVF increase	0, 0	-9.3, -52.9	-30.4, -48.9
Mass flow rate (kg/s)	46.55	45.49	44.69
% Mass flow rate increase	0	-2.3	-4.0
Power (W)	1511.7	1510.5	1488.0
% Power increase	0	-0.1	-1.6

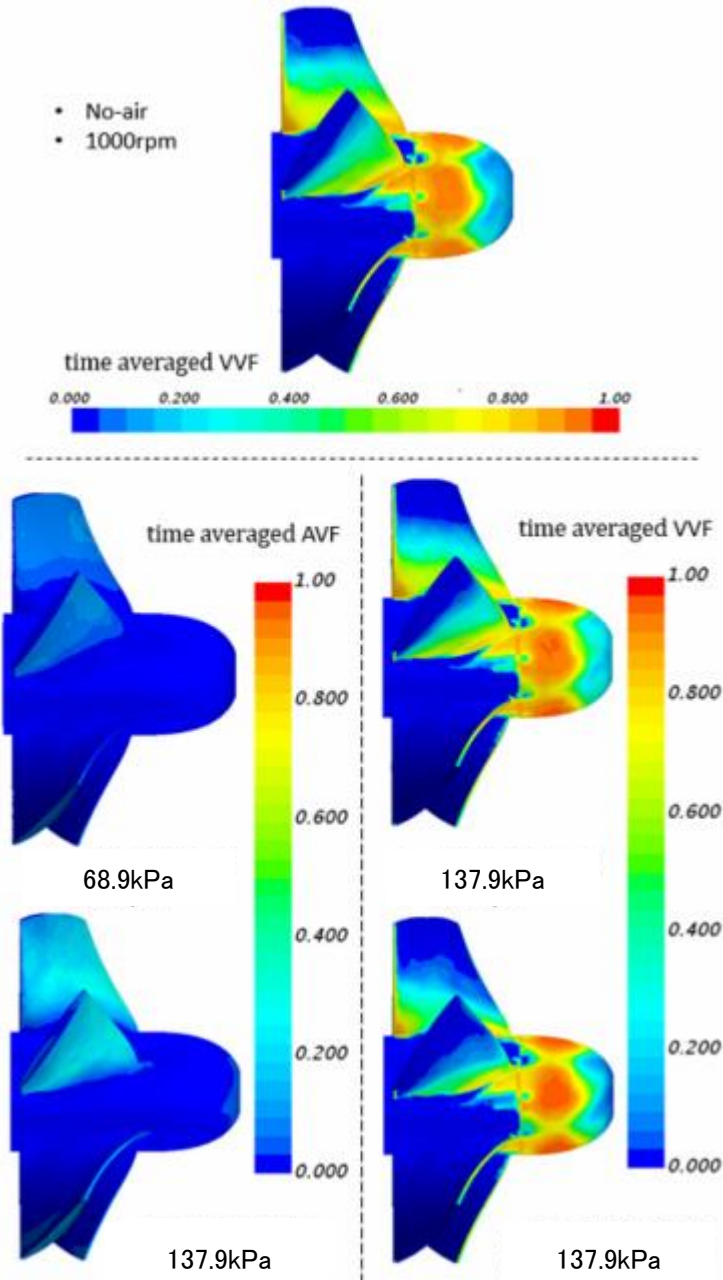


Figure 51 : Comparison of 68.9kPa and 137.9kPa air injection in terms of depth of air penetration and reduction of cavitation when the rotational speed is 1000rpm

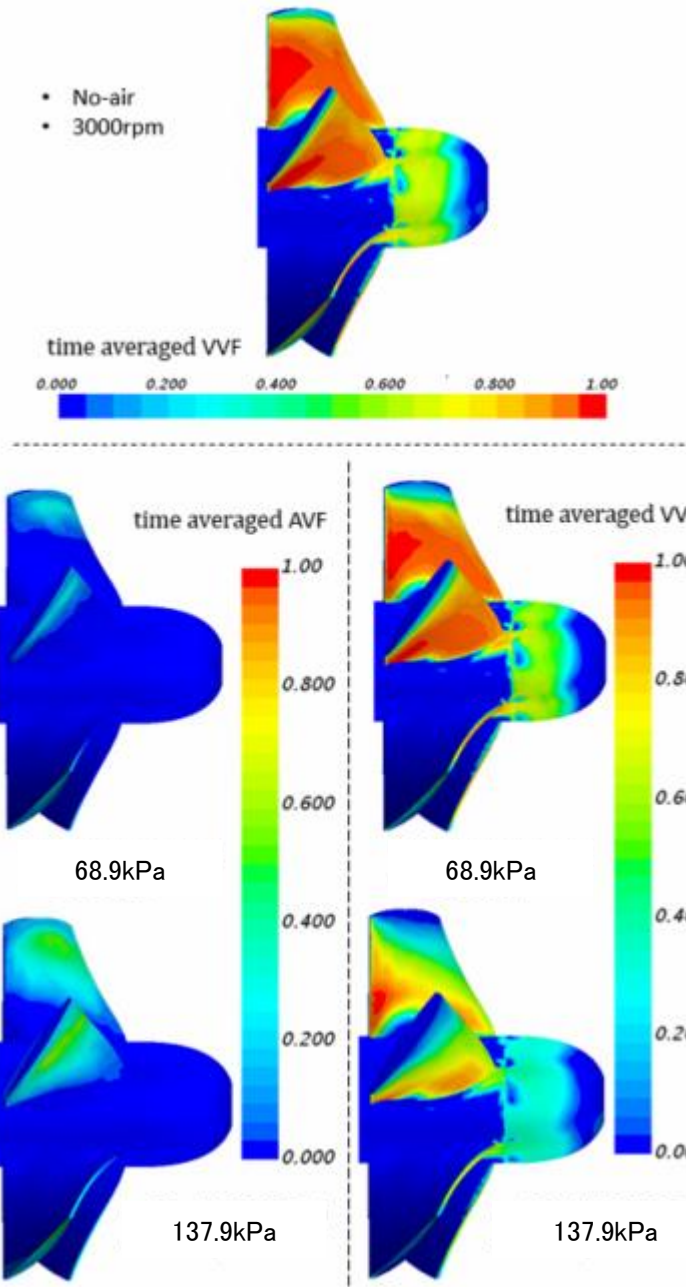


Figure 52 : Comparison of 68.9kPa and 137.9kPa air injection in terms of depth of air penetration and reduction of cavitation when the rotational speed is 3000rpm

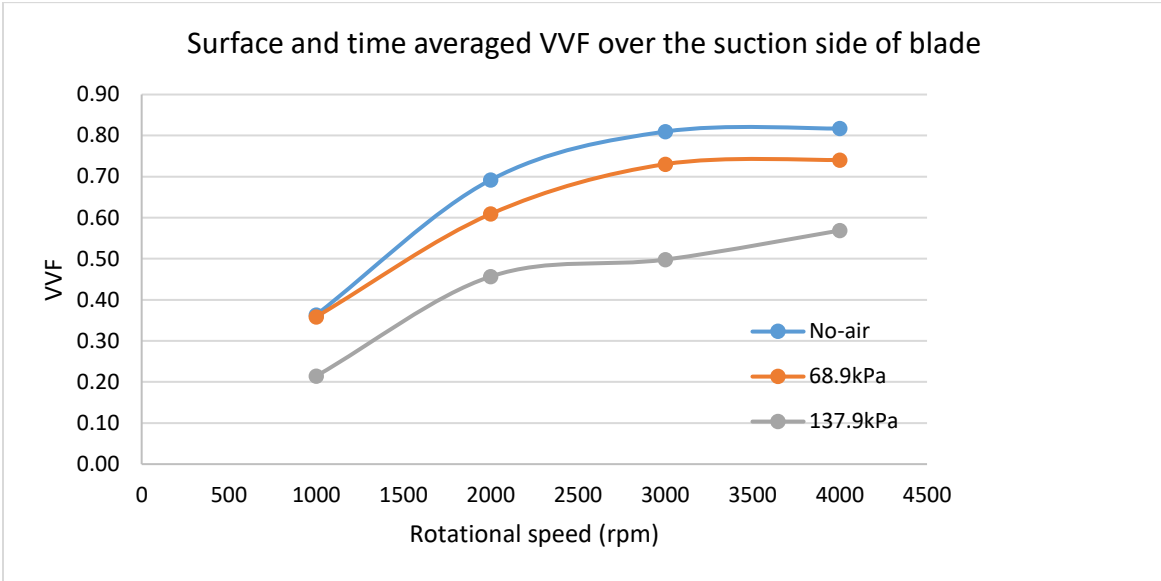


Figure 53: Profile of surface and time averaged VVF over the suction side of blade

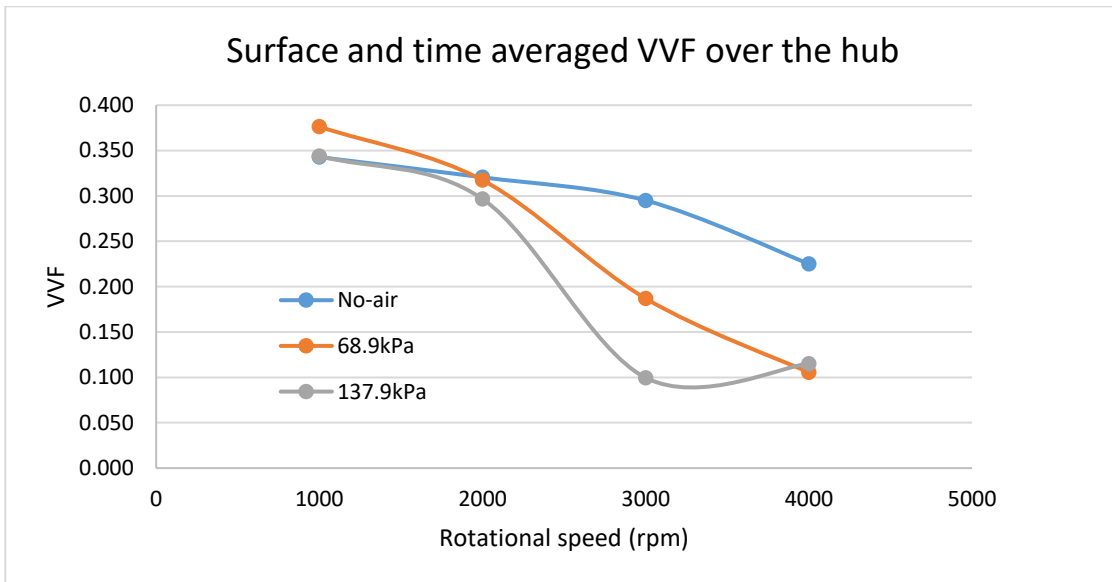


Figure 54: Profile of surface and time averaged VVF over the hub

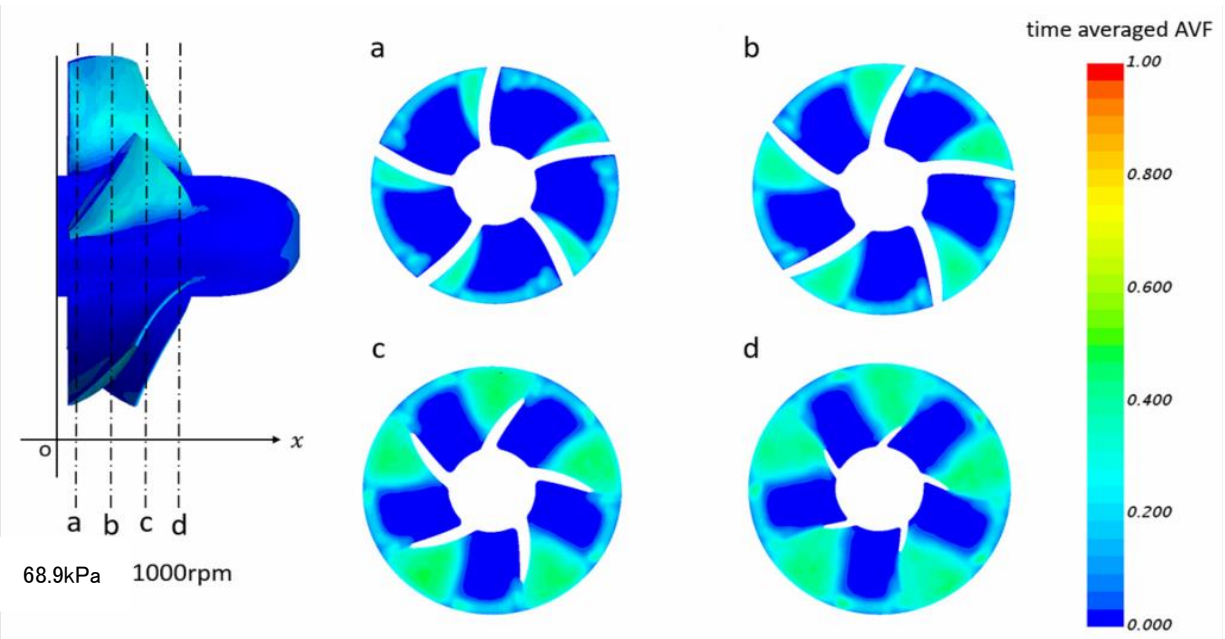


Figure 55: Contour plots of time averaged AVF over the turbine and cross sections a, b, c and d when the rotational speed is 1000rpm and pressure on the air holes is 137.9kPa.

### 5.3.4. Design B

Since Design A could not eliminate cavitation around the hub and the joint of the blades and the hub, because air could not penetrate deep enough into the flow regions to reduce cavitation around these areas (see Figure 55), three air injection holes were made on each blade in different depth. As the boundary condition on the injection holes, 103.4kPa and 137.9kPa gauge pressure were applied. The results of each rotational speed case are shown in Table 14–Table 17, respectively. Since the air injection holes are set at different depths, air injected into the system covers all over the turbine. Figure 56 is the contour plots of the time averaged VVF and AVF over the turbine of the Design A and the Design B when the turbine

rotates at 1000rpm. It shows that the air injected from the Design B can cover around the hub and the joint of the hub and blades. Hence, the pressurized air from Design B could eliminate more area than the air injected from the Design A (the area circled by red circles in Figure 56). Likewise, in every rotational speed case, the aeration from the Design B reduced cavitation more than the aeration from the Design A, as shown in Table 14–Table 17. The ability of aeration treatment by the Design B to eliminate cavitation can be seen in Figure 57 and Figure 58 as well. The reduction of cavitation is remarkably large especially when the rotational speed is 1000rpm or 2000rpm, and the maximum reduction percentage is 96.1% over the blade, and 98.7% over the hub.

Due to the presence of air in the system, the mass flow rate and power output were dropped at most by 6.7% and 16.1%, respectively. The pressure at the inlet (82.7kPa) is equivalent to 8.43m water head. Hence the efficiency drop can be calculated by Eq. (36) and Eq. (37), using the data from Table 14–Table 17. The efficiency drop of each rotational speed case with air injected from the Design B is summarized in Figure 59. Considering the significant reduction of cavitation (at most 96.1% over the blade and 98.7% over the hub), the aeration treatment by Design B is useful regarding preventing erosion and vibration caused by cavitation even though the air injection treatment reduces the power output and the efficiency of the turbine.

$$\eta = \frac{(\text{Power output})}{QgH} \quad (36)$$

$$(\text{Efficiency drop}) = \frac{\eta_{Air} - \eta_{No-air}}{\eta_{No-air}} \times 100 [\%] \quad (37)$$

Table 14: Air injection Design B compared to No-air case when the rotational speed is 1000rpm

1000rpm	No-air	103.4kPa	137.9kPa
AVF at outlet	0	0.20	0.23
VVF (blade, hub)	0.363, 0.343	0.079, 0.043	0.021, 0.0056
% VVF increase	0, 0	-78.2, -98.7	-94.2, -98.4
Mass flow rate (kg/s)	35.23	33.70	33.20
% Mass flow rate increase	0	-4.3	-5.8
Power (W)	612.9	548.7	514.5
% Power increase	0	-10.5	-16.1

Table 15 : Air injection Design B compared to No-air case when the rotational speed is 2000rpm

2000rpm	No-air	103.4kPa	137.9kPa
AVF at outlet	0	0.20	0.23
VVF (blade, hub)	0.692, 0.321	0.090, 0.088	0.027, 0.0094
% VVF increase	0, 0	-87.0, -72.6	-96.1, -97.1
Mass flow rate (kg/s)	39.14	37.12	36.50
% Mass flow rate increase	0	-5.2	-6.7
Power (W)	1103.4	1021.8	926.2
% Power increase	0	-7.4	-16.1

Table 16 : Air injection Design B compared to No-air case when the rotational speed is 3000rpm

3000rpm	No-air	103.4kPa	137.9kPa
AVF at outlet	0	0.18	0.22
VVF (blade, hub)	0.810, 0.295	0.385, 0.200	0.139, 0.108
% VVF increase	0, 0	-52.5, -32.2	-82.9, -63.2
Mass flow rate (kg/s)	42.99	40.49	40.45
% Mass flow rate increase	0	-5.8	-5.9
Power (W)	1414.2	1316.1	1285.0
% Power increase	0	-6.9	-9.1

Table 17: Air injection Design B compared to No-air case when the rotational speed is 4000rpm

4000rpm	No-air	103.4kPa	137.9kPa
AVF at outlet	0	0.18	0.21
VVF (blade, hub)	0.817, 0.225	0.544, 0.154	0.22, 0.031
% VVF increase	0, 0	-33.4, -31.6	-73.1, -86.5
Mass flow rate (kg/s)	46.55	44.35	44.41
% Mass flow rate increase	0	-4.7	-4.6
Power (W)	1511.7	1352.8	1345.0
% Power increase	0	-10.5	-11.0

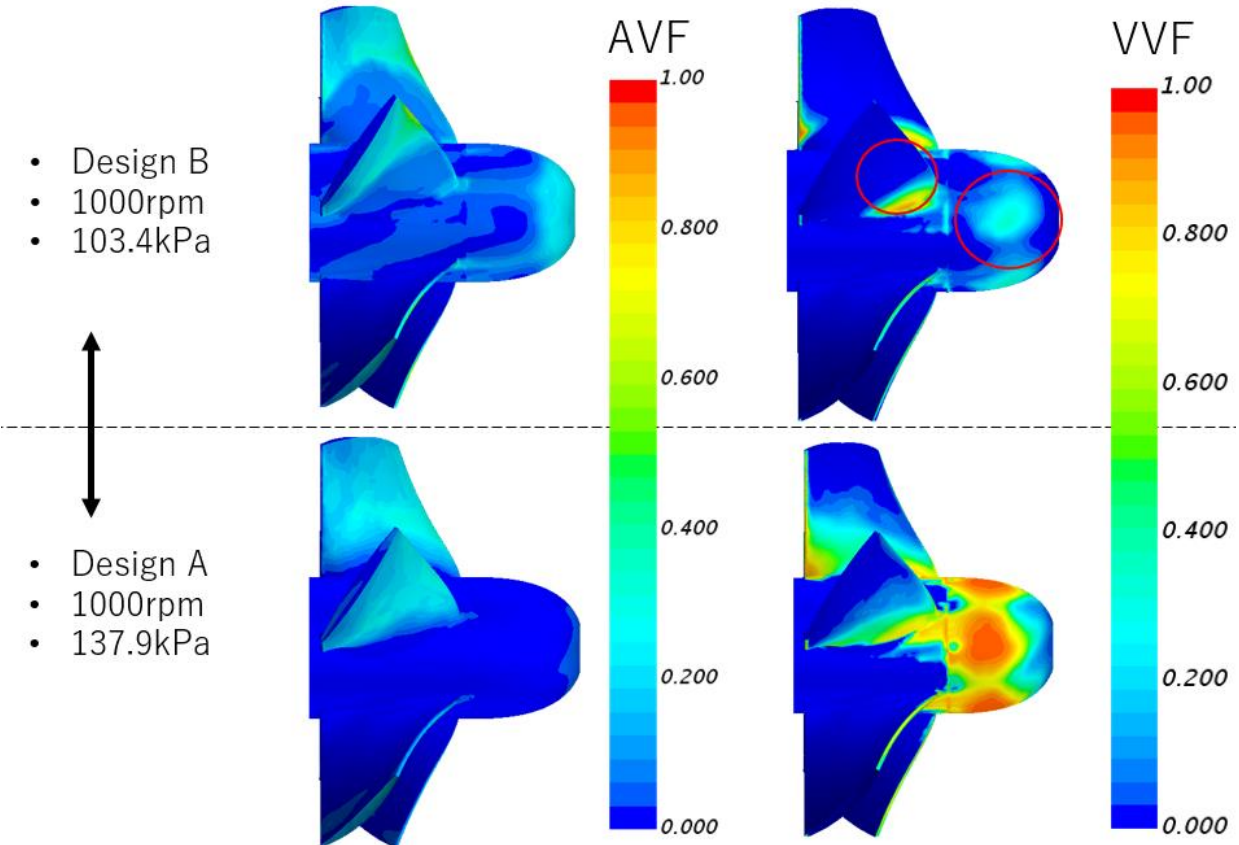


Figure 56: Contour plots of time averaged AVF and VVF over the turbine when the rotational speed is 1000rpm; air injected by 103.4kPa from the Design B(top), air injected 137.9kPa from the Design A (bottom)

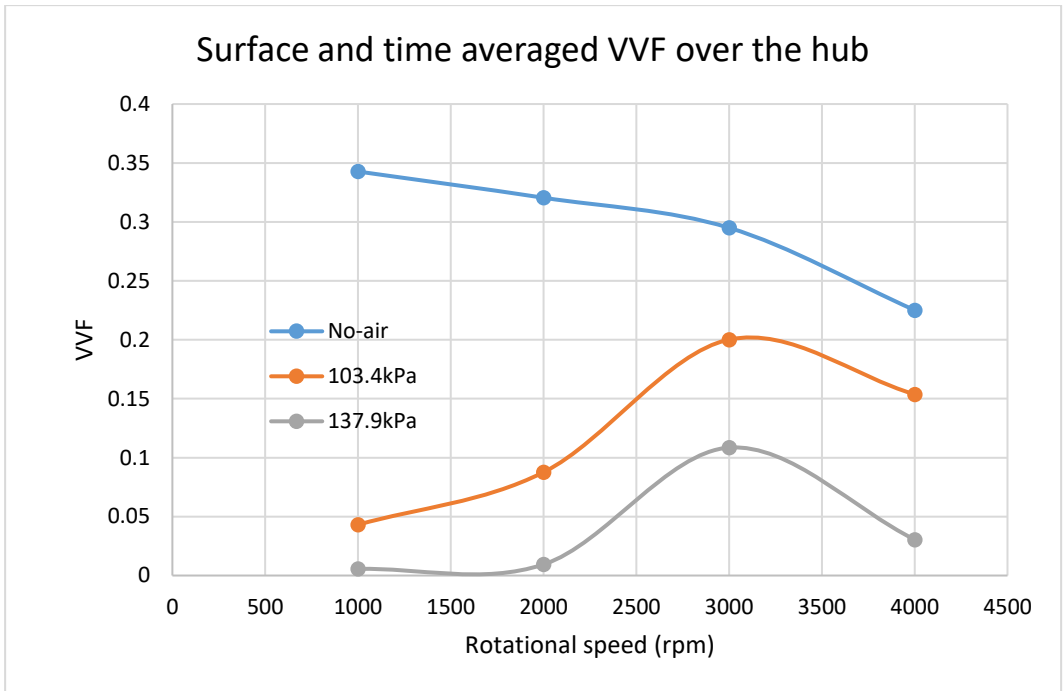


Figure 57 : Profile of surface and time averaged VVF over the hub, Design B

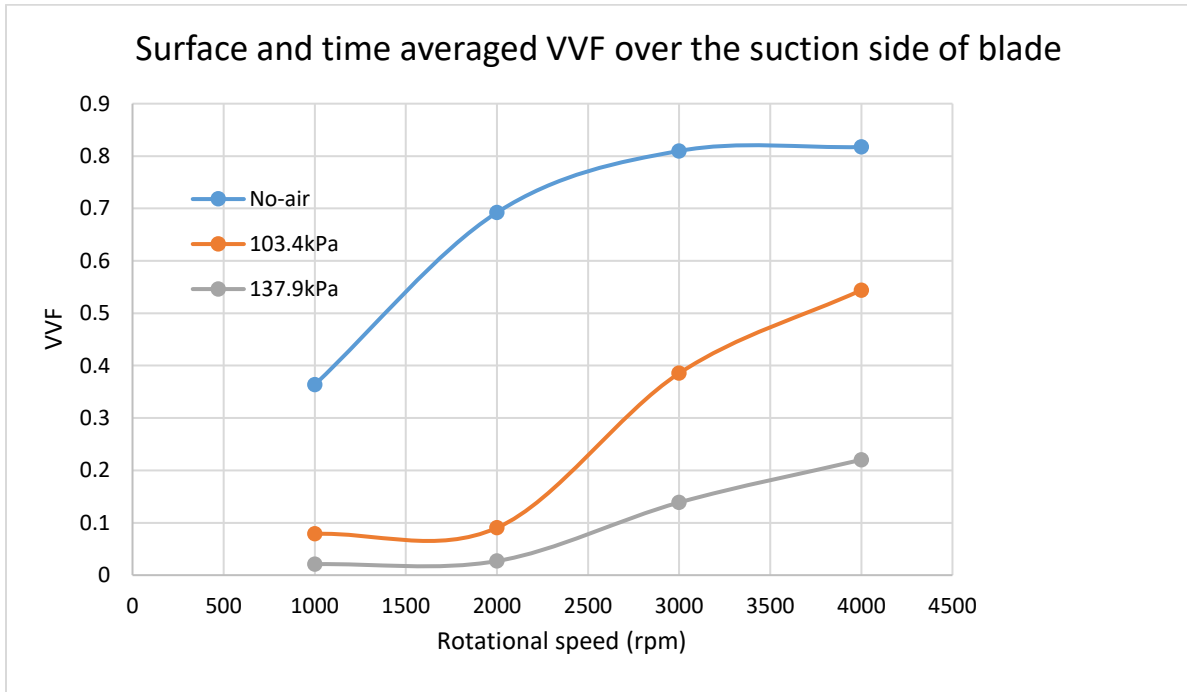


Figure 58 : Profile of surface and time averaged VVF over the suction side of blade, Design B

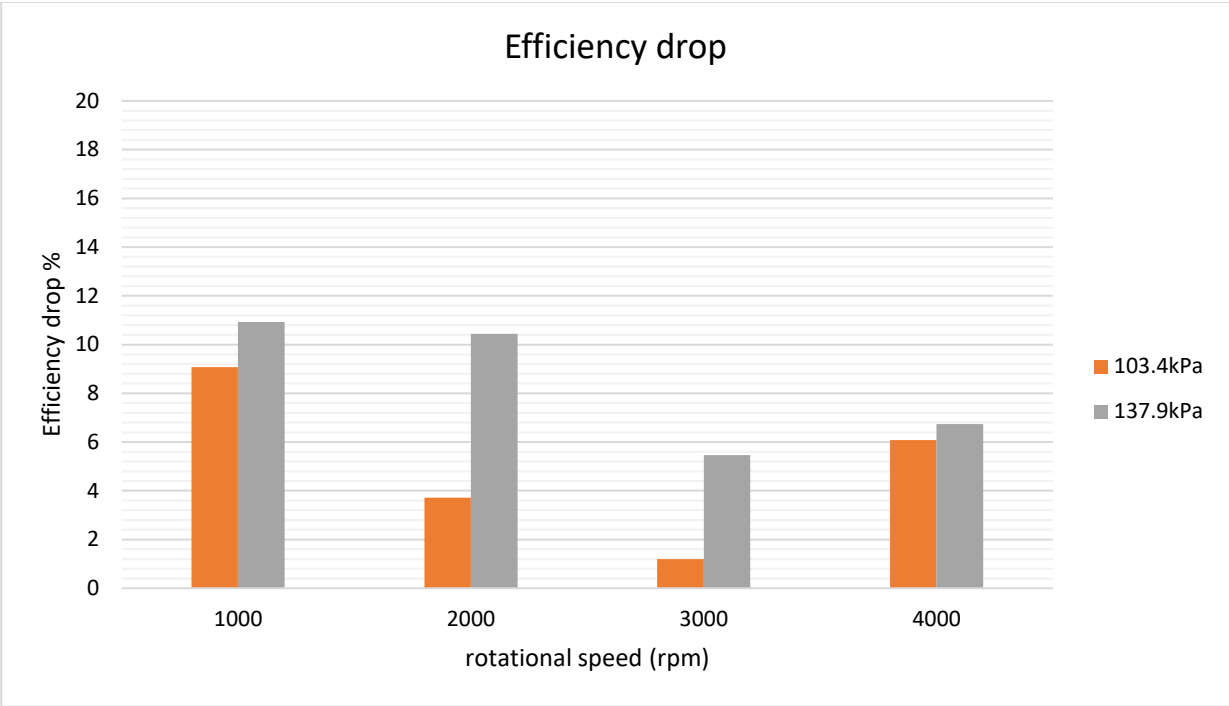


Figure 59: Efficiency drop of the turbine when air is injected from the Design B

Moreover, the improvement of the working condition of hydro turbine has to be regarded as the benefit of air injection treatment. As Avellan reported, hydro turbines have a limitation of the range of rotational speed because high rotational speed may cause intense cavitation, which results in erosion of turbines [31]. If the system has to be run with the turbine covered by cavitation less than 10% of area of the suction side of the blade, for instance, the system used in this study cannot run with a higher rotational speed than 300rpm, which just gives 195W (see Table 18; the result of 300rpm with No-air case was added). However, aeration from Design B enables the system to run even when the rotational speed is 1000rpm or 2000rpm because it eliminates cavitation over the blade till less than 10% of the area of the

suction side of the blade (see Figure 60). In another word, aeration treatment can expand the range of rotational speed which the system can run safely.

Table 18: VVF over the blade and hub, Mass flow rate and Power when the turbine rotates at 300rpm

VVF (blade)	VVF (hub)	Mass flow rate (kg/s)	Power (W)
0.098	0.273	32.5	195.3

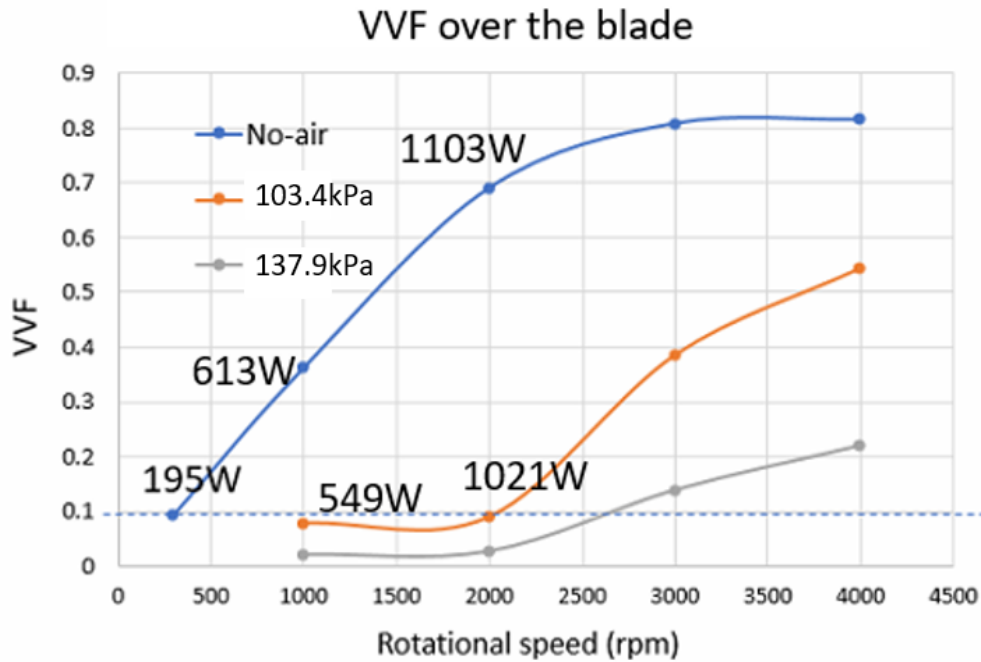


Figure 60: Profile of VVF over the blade

### 5.3.5. Constant Head Case

In the previous study, the inlet boundary conation was set at a constant pressure (82.7kPa), assuming the water head was constant. In this section, the constant mass flow rate of water as inlet boundary condition at the inlet is applied in each rotational speed for Design

B (see Figure 61). The inlet mass flow rate of each rotational speed is set as the same as the baseline data (No-air case). The results of each rotational speed are shown in Table 19–Table 22. The difference between these results from previous results with the constant head condition can be found in power output (see Figure 62). The power output of constant mass flow rate cases increased in every rotational speed case, while the power output of constant pressure inlet cases decreased due to the drop in mass flow rate because of the existence of air in the system. The increase in power output can be explained by examining the pressure at the inlet. Since constant mass flow rate boundary condition is applied, the pressure at the inlet increased to maintain the same mass flow rate as the baseline data. The surface and time averaged gauge pressure at the inlet are shown in Figure 63. As this figure shows, the pressure at the inlet increase from 82.7kPa at most by 25kPa which is equivalent to 2.54m rise of water head. Although the power output was increased in the constant mass flow case, the efficiency of the turbine was dropped if the increase of water head is considered (see Table 23).

Figure 64 and Figure 65 are generated from the data of VVF in Table 19–Table 22, and showing the profile of the surface and time averaged VVF over the suction side of the blade and hub, respectively. Although the aeration treatment reduced cavitation in every case both over the blade and hub, it can be found that the percentage of reduction of cavitation is less than constant head cases in both blade surface and the hub surface by comparing Figure 58 and Figure 64, and Figure 57 and Figure 65 for each section. The reason why the aeration treatment with constant mass flow rate condition could not eliminate cavitation well compared

with the aeration treatment with constant pressure inlet condition can be explained by the velocity around the turbine. When air is injected, the water volume fraction is smaller than No-air case due to the presence of air, which means the effective flow area is smaller (see Figure 66). In order to maintain the same mass flow rate as the base line data with less effective flow area, the velocity around the turbine has to be bigger than baseline data in the constant mass flow case. For example, the mean velocity at the cross section  $x=0.01\text{m}$  was  $11.23\text{ (m/s)}$  when the rotational speed was  $1000\text{rpm}$  and the air was injected by  $137.9\text{kPa}$ , while the mean velocity at the cross section  $x=0.01\text{m}$  was  $9.73\text{ (m/s)}$  when the rotational speed was  $1000\text{rpm}$  and No-air was injected. Due to the increase of the velocity, the cavitation number was decreased from  $2.71$  to  $2.1$ . Hence, the cavitation which the aeration is treating in the constant mass flow case is stronger than the cavitation with No-air case. That is why the reduction percentage of cavitation in the constant mass flow case is smaller than the constant pressure case.

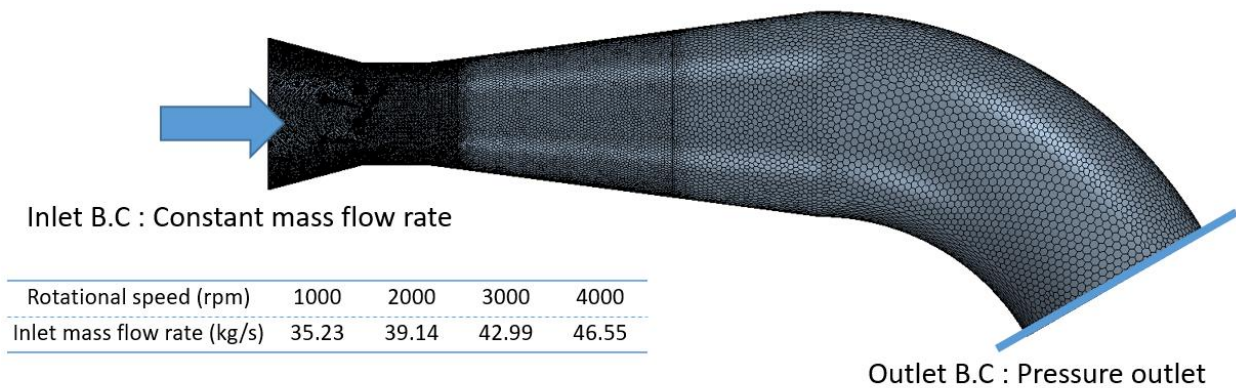


Figure 61 : Configuration of the computational domain and the inlet Boundary Condition

**Table 19 : Air injection Design B compared to No-air case when the rotational speed is 1000rpm and the inlet mass flow rate is 35.23kg/s**

1000rpm	No-air	103.4kPa	137.9kPa
AVF at outlet	0	0.21	0.24
VVF (blade, hub)	0.363, 0.343	0.284, 0.311	0.179, 0.279
% VVF increase	0, 0	-21.8, -9.3	-50.7, -18.6
Power (W)	612.9	635.3	648.7
% Power increase	0	3.7	5.8

**Table 20 : Air injection Design B compared to No-air case when the rotational speed is 2000rpm and the inlet mass flow rate is 39.14kg/s**

2000rpm	No-air	103.4kPa	137.9kPa
AVF at outlet	0	0.22	0.24
VVF (blade, hub)	0.692, 0.321	0.612, 0.302	0.523, 0.291
% VVF increase	0, 0	-11.6, -5.9	-24.4, -9.35
Power (W)	1103.4	1160.5	1197.2
% Power increase	0	5.2	8.5

**Table 21 : Air injection Design B compared to No-air case when the rotational speed is 3000rpm and the inlet mass flow rate is 42.99kg/s**

3000rpm	No-air	103.4kPa	137.9kPa
AVF at outlet	0	0.20	0.23
VVF (blade, hub)	0.810, 0.295	0.752, 0.280	0.719, 0.276
% VVF increase	0, 0	-7.2, -5.1	-11.2, -6.4
Power (W)	1414.2	1514.4	1570.0
% Power increase	0	7.1	11.0

Table 22 : Air injection Design B compared to No-air case when the rotational speed is 4000rpm and the inlet mass flow rate is 46.55kg/s

4000rpm	No-air	103.4kPa	137.9kPa
AVF at outlet	0	0.20	0.23
VVF (blade, hub)	0.817, 0.225	0.773, 0.225	0.742, 0.2185
% VVF increase	0, 0	-5.4, -0	-9.2, -2.9
Power (W)	1511.7	1694.6	1727.9
% Power increase	0	12.1	14.3

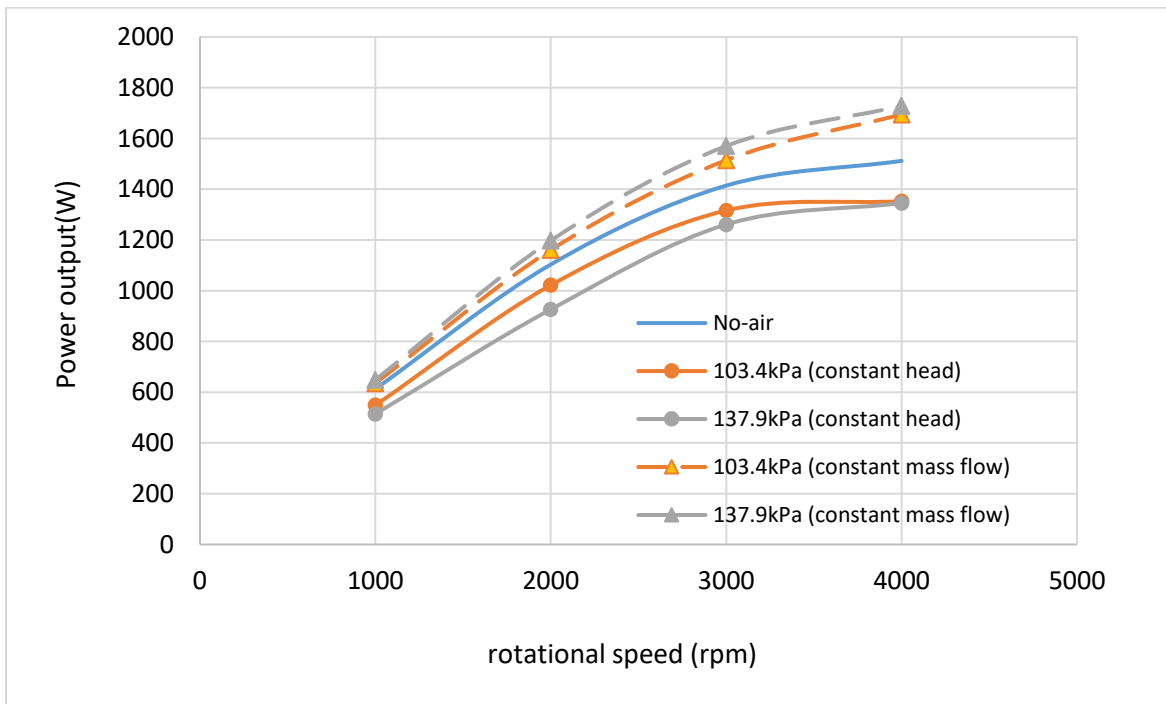


Figure 62 : Power output with different inlet condition

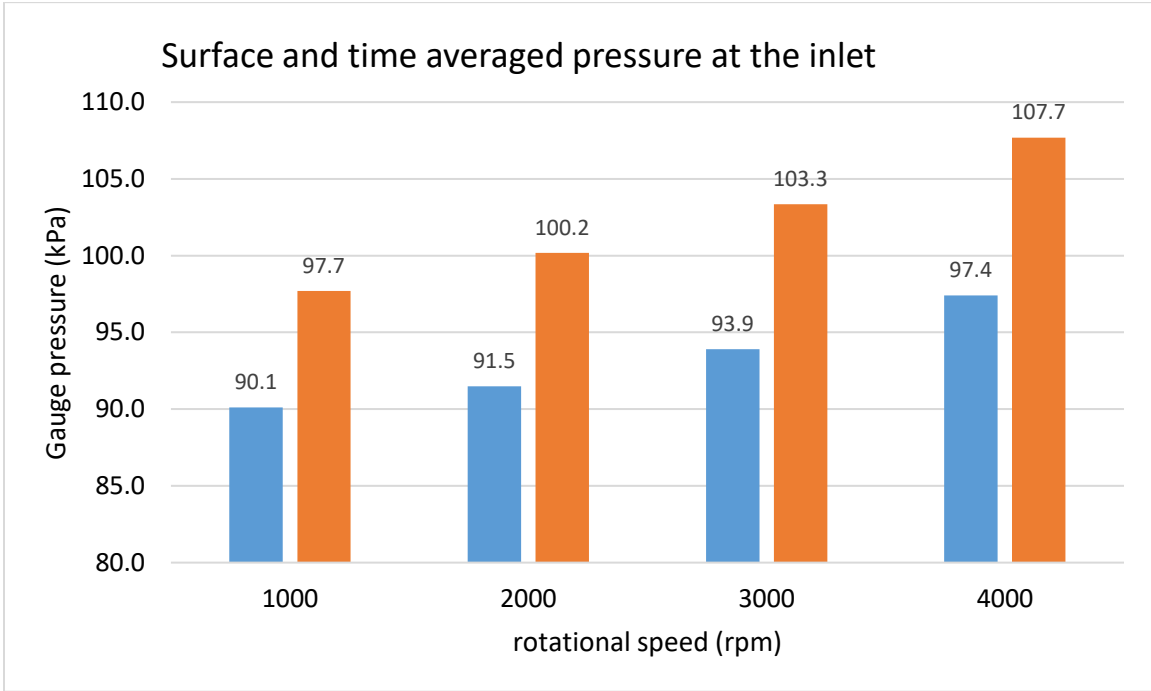


Figure 63 : Surface and time averaged pressure at the inlet

Table 23: Efficiency drop (%) of the turbine in different rotational speed cases

	1000rp	2000rpm	3000rpm	4000rpm
103.4kPa	4.8	4.9	5.7	4.8
137.9kPa	10.4	10.4	11.1	12.2

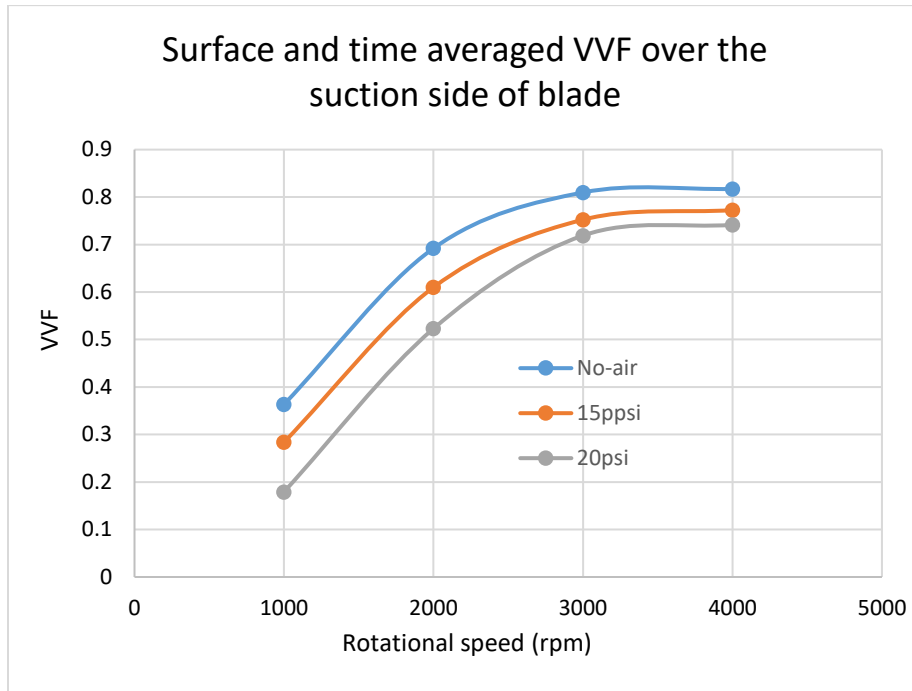


Figure 64 : Surface and time averaged VVF over the suction side of the blade with constant mass flow rate inlet condition

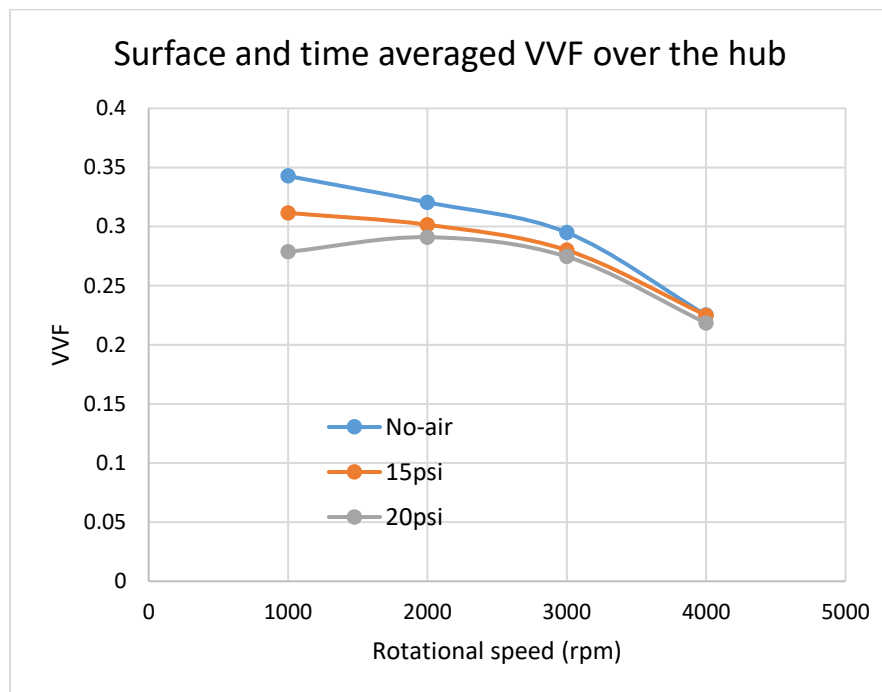


Figure 65 : Surface and time averaged VVF over the blade with constant mass flow rate inlet condition

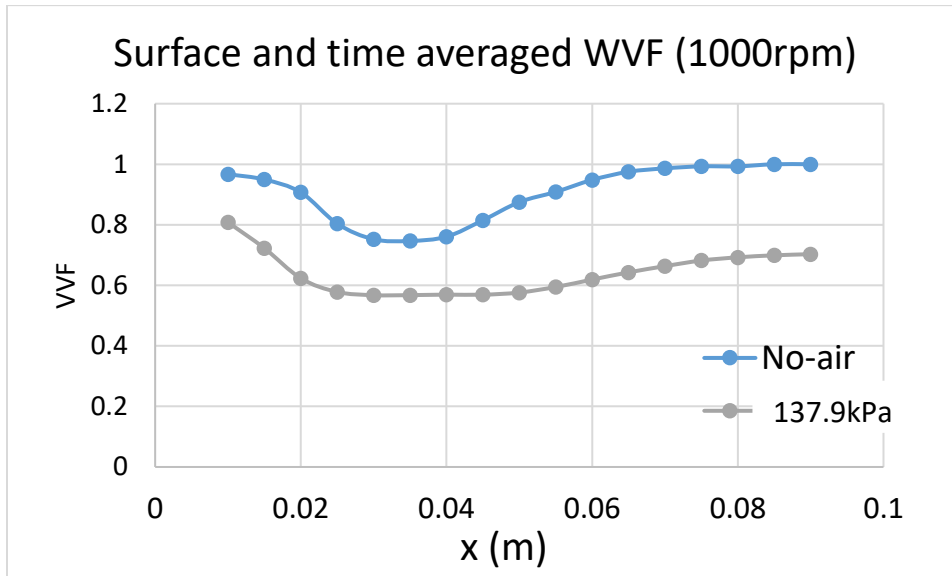


Figure 66 : Surface and time averaged WVF over the blade with constant mass flow rate inlet condition at the each cross section; 1000rpm and 137.9kPa air injection

## 6. Conclusions

In this study, the development of Kaplan hydro turbine with a rim suited for the low head was conducted, firstly, in the process of optimization of the design of the system, it was found that separations after the turbine can be eliminated by adjusting the angle of the draft tube. It was also found that the guide vanes are beneficial in reducing pressure fluctuation that may be caused by the sudden change of flow direction at the elbow, in exchange for energy loss due to the friction on the vanes. Although the experimental result did not much with the result of CFD, the experimental results showed a good agreement with the corrected CFD results after adopting the correction of  $W_f$ , which takes the energy loss due to the friction of the shaft and air in the system into account. Since the presence of air could be reduced or eliminated with a redesign and would be expected to be less in a larger system and the shaft is not necessary for the rim-drive system, it was computationally proven that the rim-drive turbine could produce 250 W with the 2.04m head.

As a method to eliminate cavitation around the turbine, aeration treatment was investigated regarding the reduction of cavitation and for improvement of the range or rotational speed in which the system can run without having much cavitation. Design A, which injects air from the housing around the stator, was first investigated. Although the pressurized air from Design A was able to reduce cavitation, it was found that cavitation around the joint of the blades and hub were not quite well reduced because the air from Design A could not

penetrate deep enough to reach around the joint. Hence, a different design, Design B, was modeled through CFD and investigated its performance. Unlike Design A, Design B could inject air to cover whole the turbine including the joint and the hub. Therefore, aeration treatment from Design B reduced cavitation significantly (at most 96.1% of the blade and 98.7% over the hub) in exchange of decrease of efficiency of the turbine. In addition to the reduction of cavitation to prevent erosion of the turbine and vibration due to cavitation, it was concluded that the aeration from Design B could reduce cavitation enough to expand the range of rotational speed in which the system can run without having strong cavitation.

The aeration treatment employing Design B with the constant mass flow rate was also examined. It was found that the power output was increased, and the increase can be explained by the rise of water head. The reduction percentage of cavitation is smaller than the constant pressure inlet case, and it can be explained by the decrease of cavitation number. Although the reduction percentage of cavitation is lower than the constant pressure inlet case, the aeration treatment could reduce cavitation in exchange of efficiency drop of the turbine.

The results emerged from the study are summarized as follows:

1. The rim-drive turbine system suited for low head, which can be installed easily due to its shaft-less design was proved to be able to generate 250W with the 2.0m head.

2. A new air injection design, Design B, can inject air all over the blade and reduce cavitation more than the Design A which inject air from the housing.
3. The percentage of reduction of cavitation by the aeration from Design B is at most 96.1% over the blade and 98.7% over the hub respectively, and this reduction of cavitation is good enough to expand the range of rotational speed in which the system can run safely.
4. In the constant mass flow rate case, the power output was increased, but the reason of the increase can be explained by the rise of water head. The efficiency is reduced when the increase of water is considered.
5. The difference of reduction percentage of cavitation between the constant pressure case and constant mass flow rate case can be explained by the decrease of cavitation number in the constant mass flow rate case.

## References

- [1] Sipahutar, R., Bernas, S.M. and Imanuddin, M.S., 2013, *Renewable energy and hydropower utilization tendency worldwide*, Renewable and Sustainable Energy Reviews, 17, pp.213-215
- [2] Hamududu, B. and Killingtveit, A., 2012, *Assessing climate change impacts on global hydropower*, Energies, 5(2), pp.305-322.
- [3] Amano, R.S., Lequesne, B., and Millevolte, J., "Very Low-Head Hydro Turbine Research," US Department of Energy, June, 2016-March, 2017, EERE Grant, Grant Number: DE-FOA-0001417.
- [4] Brennen, C.E., 1995, *Cavitation and bubble dynamics*, Oxford University Press
- [5] Arnt R, C Ellis, S Paul, 1995, *Preliminary Investigation of the Use of Air Injection to Mitigate Cavitation Erosion*, Journal of Fluids Engineering, Vol. 117, pp. 498-504.
- [6] Dong, Z.Y. and Su, P.L., 2006. *CAVITATION CONTROL BY AERATION AND ITS COMPRESSIBLE CHARACTERISTICS*, Project supported by the National Natural Science Foundation of China (Grant No: 50279048). Journal of Hydrodynamics, Ser. B, 18(4), pp.499-504
- [7] Rivetti A., Angulo M., Lucino C., and Liscia S., 2015, *Pressurized Air Injection in an Axial Hydro-Turbine Model for The Mitigation of Tip Leakage Cavitation*, 9th International Symposium on Cavitation (CAV2015), Journal of Physics: Conference Series 656.
- [8] Tinguely, M., 2013. *The effect of pressure gradient on the collapse of cavitation bubbles in normal and reduced gravity* (Doctoral dissertation, ÉCOLE POLYTECHNIQUE FÉDÉRALE DE LAUSANNE).
- [9] Brennen, C.E., 2013. *Cavitation and bubble dynamics*, Cambridge University Press.
- [10] Wu, J., Shimmei, K., Tani, K., Niikura, K. and Sato, J., 2007, *CFD-based design optimization for hydro turbines*. Journal of Fluids Engineering, 129(2), pp.159-168.
- [11] T.Kajishima, 1999, Computational simulations of turbulent flow, Youkendou, Tokyo  
梶島岳夫, 1999, 乱流の数値シミュレーション, 養賢堂, 東京
- [12] Nicoud, F. and Ducros, F., 1999, *Subgrid-Scale Stress Modelling Based on the Square of the Velocity Gradient Tensor*, Flow, Turbulence and Combustion, 62, pp. 183-200.

- [13] Noh, W.F. and Woodward, P., 1976, *SLIC (Simple Line Interface Calculation)*, Proceedings of the Fifth International Conference on Numerical Methods in Fluid Dynamics, Twente University, Enschede, NL, pp. 330-340. Springer Berlin Heidelberg.
- [14] Hirt, C.W. and Nichols, B.D., 1981, *Volume of Fluid (VOF) Method for the Dynamics of Free Boundaries*, Journal of computational physics, 39(1), pp.201-225.
- [15] Lequesne, B., Amano, R.S., and Millevolte, J., 2017, *3D-printed, integrated plug-and-play turbine-generator set for very-low-head hydro*, Technical Report: DOE-EMotors-15757-1, Under DOE DE-FOA-0001417 - SBIR/STTR FY 2016 Phase I Release 2: Topic 15.a WATER - Innovative Very Low-head and Instream Current Water Power Turbine-Generator Technologies.
- [16] [www.colorfabb.com](http://www.colorfabb.com); in particular, Eastman Amphora 3D Polymer AM3300; <http://colorfabb.com/files/AmphoraAM3300-TDS.pdf>
- [17] R. Khare, V. Prasad, M. Verma, *Design optimization of conical draft tube of hydraulic turbine*, International Journal of Advances In Engineering, Science And Technology (IJAESt), ISSN: 2249-913x, Vol. 2 No. 1, Mar-May 2012.
- [18] Moffat, R.J., 1988. Describing the uncertainties in experimental results. Experimental thermal and fluid science, 1(1), pp.3-17
- [19] Magtrol torque-meter. Available online at: <http://www.magtrol.com/manuals/tm300manual.pdf>
- [20] Omega HHT13 Tachometer. Available online at: <http://www.omega.com/temperature/pdf/hht13.pdf>
- [21] Badger-Meter electromagnetic flow-meter, Model M-2000 M-Series Mag meter. Available online at: [https://www.instrumart.com/assets/Badger-M2000\\_manual.pdf](https://www.instrumart.com/assets/Badger-M2000_manual.pdf)
- [22] Hickling, R. and Plesset, M.S., 1964, *Collapse and rebound of a spherical bubble in water*, The Physics of Fluids, 7(1), pp.7-14.
- [23] Patella, R.F., Choffat, T., Reboud, J.L. and Archer, A., 2013. *Mass loss simulation in cavitation erosion: Fatigue criterion approach*. Wear, 300(1), pp.205-215.
- [24] Petkovšek, M. and Dular, M., 2013. *Simultaneous observation of cavitation structures and cavitation erosion*. Wear, 300(1), pp.55-64.
- [25] Tsujimoto, Y., Kamijo, K. and Brennen, C.E., 2001. *Unified Treatment of Flow Instabilities of Turbomachines*. Journal of Propulsion and Power, 17(3).

- [26] Yong, W., Houlin, L., Shouqi, Y., Minggao, T. and Kai, W., 2012. *Experimental testing on cavitation vibration and noise of centrifugal pumps under off-design conditions*. Transactions of the Chinese Society of Agricultural Engineering, 2012(2).
- [27] Lahdelma, S. and Juuso, E.K., 2008. *Vibration analysis of cavitation in Kaplan water turbines*. IFAC Proceedings Volumes, 41(2), pp.13420-13425.
- [28] Medvitz, R.B., Kunz, R.F., Boger, D.A., Lindau, J.W., Yocum, A.M. and Pauley, L.L., 2002. *Performance analysis of cavitating flow in centrifugal pumps using multiphase CFD*. TRANSACTIONS-AMERICAN SOCIETY OF MECHANICAL ENGINEERS JOURNAL OF FLUIDS ENGINEERING, 124(2), pp.377-383.
- [29] Arn, C., Dupont, P. and Avellan, F., 1996. *Efficiency alteration of Francis turbines by traveling bubble cavitation*. In Hydraulic Machinery and Cavitation (pp. 524-533). Springer Netherlands.
- [30] Avellan, F., 2004, October. *Introduction to cavitation in hydraulic machinery*. In The 6th International Conference on Hydraulic Machinery and Hydrodynamics, Timisoara, Romania.
- [31] Yakushiji, R., 2009. *Mechanism of tip vortex cavitation suppression by polymer and water injection* (Doctoral dissertation, University of Michigan).
- [32] Korkut, E. and Atlar, M., 2002, January. *On the importance of the effect of turbulence in cavitation inception tests of marine propellers*. In Proceedings of the Royal Society of London A: Mathematical, Physical and Engineering Sciences (Vol. 458, No. 2017, pp. 29-48). The Royal Society.
- [33] Kermeen, R.W., 1956, *Water tunnel tests of NACA 4412 and Walchner Profile 7 hydrofoils in non-cavitating and cavitating flows*, Calif. Inst. of Tech. Hydro. Lab. Rep. 47-5.